

Electronic Thesis and Dissertation Repository

---

11-18-2011 12:00 AM

## High power systems for dynamic field control and shielding in the MR environment

Dustin W. Haw, *The University of Western Ontario*

Supervisor: Dr. Blaine A. Chronik, *The University of Western Ontario*

A thesis submitted in partial fulfillment of the requirements for the Doctor of Philosophy degree in Physics

© Dustin W. Haw 2011

Follow this and additional works at: <https://ir.lib.uwo.ca/etd>



Part of the [Other Physics Commons](#)

---

### Recommended Citation

Haw, Dustin W., "High power systems for dynamic field control and shielding in the MR environment" (2011). *Electronic Thesis and Dissertation Repository*. 313.  
<https://ir.lib.uwo.ca/etd/313>

This Dissertation/Thesis is brought to you for free and open access by Scholarship@Western. It has been accepted for inclusion in Electronic Thesis and Dissertation Repository by an authorized administrator of Scholarship@Western. For more information, please contact [wlsadmin@uwo.ca](mailto:wlsadmin@uwo.ca).

HIGH POWER SYSTEMS FOR DYNAMIC FIELD CONTROL AND SHIELDING IN  
THE MR ENVIRONMENT

(Systems for dynamic field control and shielding in MR)

(Thesis format: Integrated Article)

by

Dustin Wesley Haw

Graduate Program in Physics

A thesis submitted in partial fulfillment  
of the requirements for the degree of  
Doctor of Philosophy

The School of Graduate and Postdoctoral Studies  
The University of Western Ontario  
London, Ontario, Canada

© Dustin W. Haw, 2011

THE UNIVERSITY OF WESTERN ONTARIO  
School of Graduate and Postdoctoral Studies

**CERTIFICATE OF EXAMINATION**

Supervisor

Examiners

\_\_\_\_\_  
Dr. Blaine Chronik

\_\_\_\_\_  
Dr. Dennis Parker

Supervisory Committee

\_\_\_\_\_  
Dr. Giles Santyr

\_\_\_\_\_  
Dr. Eugene Wong

\_\_\_\_\_  
Dr. Neil Gelman

\_\_\_\_\_  
Dr. Martin Zinke-Allman

\_\_\_\_\_  
Dr. Eugene Wong

The thesis by

**Dustin Wesley Haw**

entitled:

**High power systems for dynamic field control and shielding in the  
MR environment**

is accepted in partial fulfillment of the  
requirements for the degree of  
Doctor of Philosophy

\_\_\_\_\_  
Date

\_\_\_\_\_  
Chair of the Thesis Examination Board

# Abstract

This thesis addresses several aspects of gradient and shim coil design and fabrication. New design techniques are coupled with experimental construction methods to expand small animal insert gradient and shim technology. The design techniques are also applied to other areas of magnetic resonance hardware.

A custom 2-axis gradient insert coil is designed and fabricated for the purpose of eddy current characterization. The construction tolerances were examined via bench top inductance measurements and eddy currents measurement inside a 7.0 T head-only MR system. A great deal of freedom is available when positioning shielding coils with respect to their corresponding primary coils in small animal inserts before eddy currents become prohibitive for imaging.

A new method for actively shielding electromagnets is presented. The minimum energy method for designing shielding coils of any geometry is developed and validated against historical methods. Several shielded gradient insert coils are designed, including a cylindrical gradient set with rectangular shields, which demonstrates the versatility of this new method. The performance of the shielded insert coils is reported.

A high power custom shim insert coil is designed and optimized for dynamic shimming applications. This 10-axis shim insert coil is designed to operate at currents higher than any previously existing shim sets. Several experimental fabrication methods are tested during the construction of the insert coil. Inductance, resistance and cooling measurements are conducted and compared to design specifications. Field measurements are taken using a 3-axis field transducer and the shim efficiencies are calculated. Finally mutual inductance measurements are taken between strongly coupled axes to verify active shielding performance.

Lastly, the minimum energy method for active shielding is applied to several MR fringe field type problems. Shields are designed to conform to rooms within an imaging facility for the purpose of controlling the magnetic footprint of an MR system. The MR room itself it designed to house an active shield, along with rooms adjacent to the MR room

and a small equipment cabinet located inside the MR room is also fitted with a shield. The performance of the shields is calculated, and the feasibility of such shields is discussed.

## Keywords

magnetic resonance imaging, electromagnetism, electromagnets, magnetic field, gradient coils, stream function, eddy currents, shim coils, dynamic shimming, inductance, shim efficiency, active shielding, magnetic susceptibility, homogeneity, minimum energy method, boundary element method, room shielding

# Co-authorship statement

This thesis contains materials from the following manuscripts:

- Haw D W, Harris C T, Handler W B and Chronik B A 2011. A direct minimum energy method for designing active shields of arbitrary geometry (*Submitted to IEEE Transactions on Magnetics*)

This manuscript is reproduced in its entirety and portions thereof in chapter 3. This manuscript was written by Dustin Haw. All theoretical work, computer modeling, experiments, data collection, and data analysis was performed by Dustin Haw with the following exceptions:

Brian Dalrymple and Frank Van Sas provided assistance in machining components for the insert gradient in chapters 2 and the insert shim set in chapter 4. Martin Klassen wrote the eddy current measurement pulse sequence, and Joe Gati and Jamu Alford assisted in setting up the insert gradient on the Varian system in chapter 2. Chad Harris wrote computer code, performed simulations and coauthored the work in chapter 3. Will handler wrote computer code for thermal, inductance, and efficiency calculations, as well as a Levenberg-Marquardt fitting routine. Blaine Chronik, Kyle Gilbert, Timothy Scholl, Will Handler, and Chad Harris contributed their ideas throughout this work.

*To my Mom and Dad,  
for their endless support.*

# Acknowledgments

This thesis represents a major commitment from many individuals who contributed their time, expertise and guidance, both academically and personally.

The completion of this work is largely due to Dr. Blaine Chronik, who supervised me throughout my graduate career. He provided me with the opportunity and guidance necessary to make this work a reality, as well as the freedom to explore my own ideas. I am blessed to have had such a phenomenal role model.

Drs. Will Handler and Tim Scholl have contributed to this project in every way imaginable from computer programming to final construction. They acted not only as colleagues, but friends, who made my day to day experience as a grad student more enjoyable.

Dr. Kyle Gilbert, once a fellow graduate student and now a close friend deserves a special recognition. His assistance with this work is greatly appreciated, but it's his role as a friend that will never be forgotten.

Brian Dalrymple and Frank Van Sas put a great deal of effort into both the construction of my insert coils and the development of my shop skills. Without their expertise this project would be nothing more than a collection of simulations.

I am very grateful for the many people who have worked closely with me during my degree. They include: James Odegaard, Josh de Bever, Parisa Hudson, Joe Gati, Jamu Alford, Geron Bindseil and Chad Harris.

Finally, I would like to acknowledge the three people that have had the greatest influence on me: Ann, Mom and Dad. Everything I have and everything I am is because of them.



# Table of contents

<b>CERTIFICATE OF EXAMINATION</b> .....	ii
Abstract .....	iii
Co-Authorship Statement.....	v
Dedication .....	vi
Acknowledgements.....	vii
Table of Contents .....	viii
List of Tables .....	xi
List of Figures .....	xii
Chapter 1 .....	1
1 Introduction .....	1
1.1 Introduction to magnetic resonance imaging .....	1
1.2 Nuclear magnetic resonance (NMR) and signal .....	1
1.3 MRI hardware .....	5
1.3.1 Main magnets .....	6
1.3.2 RF coils .....	8
1.3.3 Gradient coils and shim coils .....	10
1.3.3.1 Gradient coils.....	10
1.3.3.2 Shim coils .....	15
1.4 Magnetic field imperfections .....	17
1.5 Thesis overview .....	22
1.6 References.....	26
Chapter 2.....	27
2 Construction tolerances of small animal insert gradient coils .....	27
2.1 Introduction.....	27
2.2 Methods .....	28
2.2.1 Gradient coil design .....	28
2.2.2 Gradient coil construction .....	29
2.2.3 Bench testing.....	34
2.2.4 Eddy current measurements .....	35
2.2.5 Data analysis .....	36
2.3 Results.....	37
2.3.1 Bench testing.....	37
2.3.2 Eddy current measurements .....	39
2.4 Discussion.....	41
2.5 References.....	44
Chapter 3.....	46

3	A direct minimum energy method for designing shielding coils of arbitrary geometry.....	46
3.1	Introduction.....	46
3.2	Methods .....	48
3.3	Results.....	52
3.3.1	Cylindrical gradient.....	52
3.3.2	Planar gradient .....	54
3.3.3	Cylindrical gradient with rectangular shield .....	55
3.4	Discussion.....	57
3.5	References.....	61
Chapter 4.....		63
4	Design and construction of a high-power insert gradient and shim system for dynamic shimming in small animal MRI .....	63
4.1	Introduction .....	63
4.2	Methods .....	66
4.2.1	Design methods.....	66
4.2.2	Minimization of mutual interactions.....	66
4.2.3	Cooling strategy .....	68
4.2.4	Fabrication.....	68
4.2.4.1	Zonal shims.....	68
4.2.4.2	Transverse shims .....	69
4.2.4.3	Integration.....	69
4.2.5	Testing.....	70
4.3	Results.....	72
4.3.1	Design results .....	72
4.3.2	Minimization of coupling.....	76
4.3.3	Cooling.....	77
4.3.4	Fabrication.....	78
4.3.4.1	Zonal shims.....	78
4.3.4.2	Transverse shims .....	80
4.3.4.3	Integration.....	82
4.4	Discussion.....	84
4.5	References.....	87
Chapter 5.....		89
5	A new approach to the challenges of siting MRI systems: active room shielding .....	89
5.1	Introduction .....	89
5.2	Methods .....	93
5.2.1	Static MR room.....	95
5.2.2	Static adjacent room.....	97
5.2.3	Static equipment cabinet .....	99
5.2.4	Dynamic equipment cabinet.....	101
5.2.5	Dynamic equipment cart .....	101
5.2.6	Performance calculations .....	102
5.3	Results.....	103
5.3.1	Static MR room.....	103
5.3.2	Static adjacent room.....	107
5.3.3	Static equipment cabinet .....	114
5.3.4	Dynamic equipment cabinet.....	117

5.3.5 Dynamic equipment cart .....	120
5.4 Discussion .....	123
5.5 References.....	127
Chapter 6.....	131
6 Discussions and future work .....	131
6.1 Thesis summary .....	131
6.2 Future work.....	132
6.2.1 Eddy current measurments .....	132
6.2.2 Minimum energy method.....	133
6.2.3 Dynamic shim set.....	134
6.2.4 Room shielding .....	135
6.3 References.....	136
A Minimum energy method and historical method equivalency.....	137
A.1 References.....	141
Curriculum Vitae .....	142

# List of tables

## Table

1.1	The name and functional form for the most common shim orders .....	17
2.1	Performance data for both shielded gradient axes .....	37
2.2	Eddy current time constants .....	40
3.1	Efficiency and inductance values for the cylindrical gradient set .....	53
3.2	Efficiency and inductance values for the rectangular shield .....	55
4.1	Efficiency, inductance and resistance values for each shim coil.....	74
4.2	Shielding efficiency ratios for zonal shims .....	74
4.3	Simulated and measured mutual inductance for shielded shims .....	76
4.4	Power values for each shim axes .....	78
4.5	Cooling capacity for each cooling layer .....	78
5.1	The specifications for each coil in the 1.0 T main magnet.....	95
5.2	Performance parameters for the MR room shield .....	106
5.3	The performance parameters of both the adjacent room shields .....	110
5.4	Performance values for the shielded cabinet .....	117
5.5	Current values for each cabinet shield and field values .....	118
5.6	Current values for all shields in the cart .....	120

# List of figures

## Figure

1.1	Depiction of the magnetization vector.....	3
1.2	A schematic representation of a typical MR system .....	6
1.3	A picture of two gradient coils .....	14
1.4	The magnetic field profile for a spherical piece of iron .....	21
2.1	The primary $z$ -gradient wire pattern .....	30
2.2	Both the $z$ -primary and $z$ -shield.....	31
2.3	The individual quadrants of the $y$ -coil.....	32
2.4	Fully constructed insert coil .....	32
2.5	The geometry of the gradient insert coil.....	33
2.6	Bench measurement setup for insert coil.....	34
2.7	Illustration of the pulse sequence .....	35
2.8	Inductance plots for insert coil .....	38
2.9	Frequency measurements at two RF positions .....	39
2.10	Fit frequency data and residual.....	40
2.11	Frequency offsets at each RF position.....	41
3.1	The current density profile along the $z$ -axis .....	53
3.2	The magnetic field profiles for the $z$ -gradient .....	54
3.3	The wire pattern for the planar $y$ -gradient coil.....	55
3.4	The wire patterns for the cylindrical gradient and shields.....	56
3.5	The magnetic field profiles for the gradient with rectangular shield .....	57
4.1	Simulated wire pattern for each coil in the shim set.....	73
4.2	Fitted and simulated magnetic field profiles .....	75
4.3	Schematic representation showing the ordering of the shim layers .....	77
4.4	A photograph of the $z^0$ -primary coil.....	79
4.5	A photograph of the $z_B$ -layer .....	80
4.6	A photograph of a thumbprint of the $xz$ -shim.....	81
4.7	A photograph of the $xz$ -shim after rolling .....	81
4.8	A photograph of the $xz$ -shim coil being fastened to the insert coil .....	82
4.9	A photograph of the return path layer .....	83
4.10	A photograph of the basic potting procedure for each layer .....	83
5.1	A cut-through schematic representation of the 1.0 T MR system.....	94
5.2	Meshed shielding surface and schematic for MR room shield.....	96
5.3	Meshed surface and schematic for the adjacent room shield .....	98
5.4	Meshed cabinet surface and schematic.....	100
5.5	Wire pattern for the MR room shield .....	103
5.6	Conductor paths on each wall of the room .....	104
5.7	Plot of the magnetic field lines for MR room shield .....	105
5.8	Field histograms over the rectangular surface outside the MR room.....	106

5.9	Wire pattern of the room adjacent along the $x$ -direction .....	107
5.10	Wire patterns on each of the individual walls of the adjacent room .....	108
5.11	The field lines for the MR system and transverse adjacent room shield .....	109
5.12	The histograms of field magnitudes with transverse shield .....	110
5.13	Wire pattern for the room adjacent to the MR system along the $z$ -direction.....	111
5.14	Wire patterns of each wall for the longitudinally adjacent shielded room .....	112
5.15	Magnetic field lines for the longitudinally adjacent room shield .....	113
5.16	Histograms of field magnitude for longitudinally adjacent room shield.....	114
5.17	Wire pattern for the shielded cabinet.....	114
5.18	Individual wire patterns on each face of the cabinet .....	115
5.19	Magnetic field lines for the MR system and shielded cabinet.....	116
5.20	Magnetic field histograms for shielded cabinet.....	117
5.21	Magnetic field histograms for dynamic cabinet .....	119
5.22	Translational motion field histograms for dynamic cart shield .....	121
5.23	Rotational motion field histograms for dynamic cart shield .....	122

# Chapter 1

## 1 Introduction

### 1.1 Introduction to magnetic resonance imaging

Magnetic resonance imaging (MRI) is an imaging technique that is renowned for its ability to generate excellent anatomical images of soft tissues, as well as functional images of many varieties. MRI measures the changing magnetic flux produced by non-zero magnetic moments precessing in a magnetic field. Typically it is the protons in fat and water in the human body of interest, but other nuclei with non-zero magnetic moments can be imaged as well. The signal acquired in MRI is proportional to the density of magnetic moments in the sample and is weighted by their phenomenological relaxation rates, which are tissue or material specific.

The purpose of this introductory chapter is not to provide a complete overview of MRI, but rather to highlight certain areas that are of particular importance to understanding the methods and techniques that are presented in this work. This chapter will discuss the signal acquired in a basic MR experiment from a classical perspective, focusing on the constituents that are relevant to the work presented in this thesis. The main hardware components of a typical MR system and their impact on the acquired signal will be discussed. Finally, several types of magnetic field imperfections and their effects on the imaging process will be addressed.

The concepts presented in this chapter only represent a small fraction of the MR basics. For a complete treatment of MRI several textbooks can be consulted (1-4).

### 1.2 Nuclear magnetic resonance (NMR) and signal

In conventional MRI a sample is placed in a strong, static, and homogenous magnetic field, with direction along the axis of the MR system ( $z$ -axis) and magnitude  $B_0$ . The result of the magnetic field is two-fold: a preferential alignment of the magnetic moments in the sample along the direction of the magnetic field will occur at equilibrium, along

with a precession about the magnetic field axis at a frequency,  $\omega_0$ , given by the Larmor equation:

$$\omega_0 = \gamma B_0, \quad (1.1)$$

where  $\gamma$  is the gyromagnetic ratio, which is  $2.68 \times 10^8$  rad/s/T for protons. The preference for the moments to align with the field is on the order of a few parts per million (ppm). However, the presence of Avogadro's number of magnetic moments results in a net magnetization,  $\mathbf{M}(\mathbf{r}, t)$ , of the sample. When the magnetic moments are in thermal equilibrium, the magnitude of magnetization generated is well approximated by:

$$M_0(\mathbf{r}) = \frac{\rho(\mathbf{r})\gamma^2\hbar^2 I(I+1)B_0}{3k_B T}, \quad (1.2)$$

where  $\hbar$  is Planck's constant divided by  $2\pi$ ,  $k_B T$  is the average thermal energy of the nuclei in the sample, and  $\rho(\mathbf{r})$  is the density of magnetic moments as a function of sample position.

By applying a time-varying magnetic field at the Larmor frequency and orthogonal to  $\mathbf{M}(\mathbf{r}, t)$ , the net magnetization can be perturbed and will precess around its equilibrium position in the transverse plane. This precession results in a changing magnetic flux that will induce a voltage in a radiofrequency (RF) coil if placed orthogonal to the main field as depicted in figure 1.1. The induced electromotive force (EMF) in the RF coil is linearly proportional to the signal acquired in MRI, and is given by the principle of reciprocity:

$$EMF = -\frac{d}{dt} \int_{sample} \mathbf{M}(\mathbf{r}, t) \cdot \mathbf{B}_{1, receive}(\mathbf{r}, t) d^3 r. \quad (1.3)$$

The principle of reciprocity describes the EMF as the summation of magnetization within the sample weighted by the sensitivity profile of the RF coil,  $\mathbf{B}_{1, receive}(\mathbf{r}, t)$ .



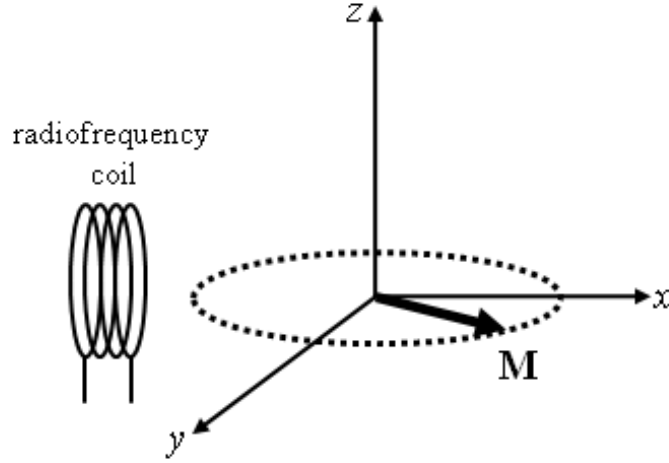


**Figure 1.1:** Depiction of the magnetization vector  $\mathbf{M}(\mathbf{r}, t)$  as it precesses in the transverse plane after it has been perturbed from equilibrium. The RF coil is placed orthogonal to the plane of precession and can detect the changing magnetic flux from the rotating magnetization.

The net magnetization in the transverse plane decays over time due to dephasing of the individual magnetic moments, and the original longitudinal magnetization recovers. Expressions for the longitudinal and transverse components of the magnetization can be solved for via the Bloch equation (5):

$$\mathbf{M}_z(\mathbf{r}, t) = M_z(\mathbf{r}, 0)e^{\frac{-t}{T_1(\mathbf{r})}} + M_0(\mathbf{r}) \left(1 - e^{\frac{-t}{T_1(\mathbf{r})}}\right) \quad (1.4)$$

$$\mathbf{M}_\perp(\mathbf{r}, t) = M_\perp(\mathbf{r})e^{i(-\omega t + \phi_0(\mathbf{r}))}e^{\frac{-t}{T_2^*(\mathbf{r})}}. \quad (1.5)$$

$M_\perp(\mathbf{r})$  is the magnetization in the transverse plane.  $T_1(\mathbf{r})$  is the phenomenological time constant that describes the rate at which longitudinal magnetization regrowth occurs.  $T_1(\mathbf{r})$  is tissue/material specific and varies with position in the sample.  $T_2^*(\mathbf{r})$  can then be given by:

$$\frac{1}{T_2^*(\mathbf{r})} = \frac{1}{T_2(\mathbf{r})} + \frac{1}{T_2'(\mathbf{r})}, \quad (1.6)$$

where  $T_2(\mathbf{r})$  is the phenomenological time constant that describes the decay of transverse magnetization due to dipole-dipole interactions between the magnetic moments within

the sample.  $T_2'(\mathbf{r})$  is the contribution to  $T_2^*(\mathbf{r})$  from all other sources of magnetic field. These include things like  $B_0$  inhomogeneity, field variations due to differences in magnetic susceptibility, and diffusion just to name a few. If all the longitudinal magnetization is tipped into the transverse plane then:  $M_{\perp}(\mathbf{r}) = M_0(\mathbf{r})$ . The  $x$ - and  $y$ -components of the net magnetization vector are given by:

$$M_x(\mathbf{r}, t) = \text{Re}\{\mathbf{M}_{\perp}(\mathbf{r}, t)\} \quad (1.7)$$

$$M_y(\mathbf{r}, t) = \text{Im}\{\mathbf{M}_{\perp}(\mathbf{r}, t)\}. \quad (1.8)$$

In order to spatially encode the signal generated in MRI, a magnetic field gradient is applied across the sample. When this gradient,  $\mathbf{G}(\mathbf{r}, t)$ , is applied, the transverse magnetization accrues extra phase depending on its position in the gradient field. This accrued phase is given by:

$$\phi(\mathbf{r}, t) = -\gamma \int_0^t \mathbf{G}(\mathbf{r}, \tau) \cdot \mathbf{r} d\tau. \quad (1.9)$$

The applied gradient field makes the phase and precession frequency of the magnetization a function of position in the sample – this spatial dependence is what allows images to be created. When we consider the extra phase accrued from the magnetic field gradients the expression for the net magnetization vector becomes:

$$\mathbf{M}_{\perp}(\mathbf{r}, t) = M_0(\mathbf{r}) e^{i(-\omega t + \phi(\mathbf{r}, t) + \phi_0(\mathbf{r}))} e^{\frac{-t}{T_2^*(\mathbf{r})}}. \quad (1.10)$$

By substituting the expressions for the longitudinal and transverse magnetization into the reciprocity relation (equation 1.3) the EMF induced in the detection coil can be solved for:

$$\begin{aligned} EMF = & - \int_{sample} \frac{d}{dt} \{M_0(\mathbf{r}) [\text{Re}\{e^{i(-\omega t + \phi(\mathbf{r}, t) + \phi_0(\mathbf{r}))}\}] B_{1x}(\mathbf{r}) + \\ & \text{Im}\{e^{i(-\omega t + \phi(\mathbf{r}, t) + \phi_0(\mathbf{r}))}\}] B_{1y}(\mathbf{r})\} e^{\frac{-t}{T_2^*(\mathbf{r})}} d^3r. \end{aligned} \quad (1.11)$$

Equation 1.11 can be simplified by taking the time derivative and accounting for the large discrepancies in orders of magnitudes between each term. At typical MR field strengths,

$1/T_1$  is on the order of  $10^0 - 10^1$  Hz,  $1/T_2^*$  is on the order of  $10^1 - 10^2$  Hz, and  $d\phi(\mathbf{r}, t)/dt$  is on the order of  $10^5 - 10^6$  Hz.  $\omega/2\pi$  is approximately  $10^7-10^8$  Hz and dominates the other terms, meaning they can be neglected. The result is:

$$EMF = -\omega \int_{sample} M_0(\mathbf{r}) [B_{1x}(\mathbf{r}) \sin(-\omega t + \phi(\mathbf{r}, t) + \phi_0(\mathbf{r})) - B_{1y}(\mathbf{r}) \cos(-\omega t + \phi(\mathbf{r}, t) + \phi_0(\mathbf{r}))] e^{\frac{-t}{T_2^*(\mathbf{r})}} d^3r. \quad (1.12)$$

Equation 1.12 can be further simplified by expressing the individual components of the RF magnetic field in terms of their magnitude and angle:

$$B_{1x}(\mathbf{r}) = B_{1\perp}(\mathbf{r}) \cos(\theta_{B1}(\mathbf{r})) \quad (1.13)$$

$$B_{1y}(\mathbf{r}) = B_{1\perp}(\mathbf{r}) \sin(\theta_{B1}(\mathbf{r})). \quad (1.14)$$

The EMF is then given by:

$$EMF = -\omega \int_{sample} M_0(\mathbf{r}) B_{1\perp}(\mathbf{r}) \sin(-\omega t + \phi(\mathbf{r}, t) + \phi_0(\mathbf{r}) + \theta_{B1}(\mathbf{r})) e^{\frac{-t}{T_2^*(\mathbf{r})}} d^3r. \quad (1.15)$$

If a complex MR signal is defined such that:  $s(t) = s_{Re}(t) + i s_{Im}(t)$ , then the acquired MR signal is given by the relation:

$$s(t) \propto -\omega \frac{\gamma^2 \hbar^2 I(I+1) B_0}{3k_B T} \int_{sample} \rho(\mathbf{r}) B_{1\perp}(\mathbf{r}) e^{i(\omega t + \phi(\mathbf{r}, t) + \phi_0(\mathbf{r}))} e^{\frac{-t}{T_2^*(\mathbf{r})}} d^3r. \quad (1.16)$$

This expression does not explicitly consider every aspect of the MR signal; other factors can influence the MR signal. However, the factors considered are the most important for the work that will follow. Of particular importance are the effects associated with the term  $e^{i\phi(\mathbf{r}, t)}$ , which will be discussed many times throughout this thesis.

### 1.3 MRI hardware

A typical MR system consists of four major hardware subsystems: the main magnet, radiofrequency coils, gradient coils and shim coils, as depicted in figure 1.2. Each hardware subsystem is vital to the imaging process and has an influence on the signal

equation derived above (equation 1.16). This section provides a discussion of each hardware component and highlights its effect on the signal equation. In the case of gradient and shim coils a more thorough outline will be given as necessary background for this work.

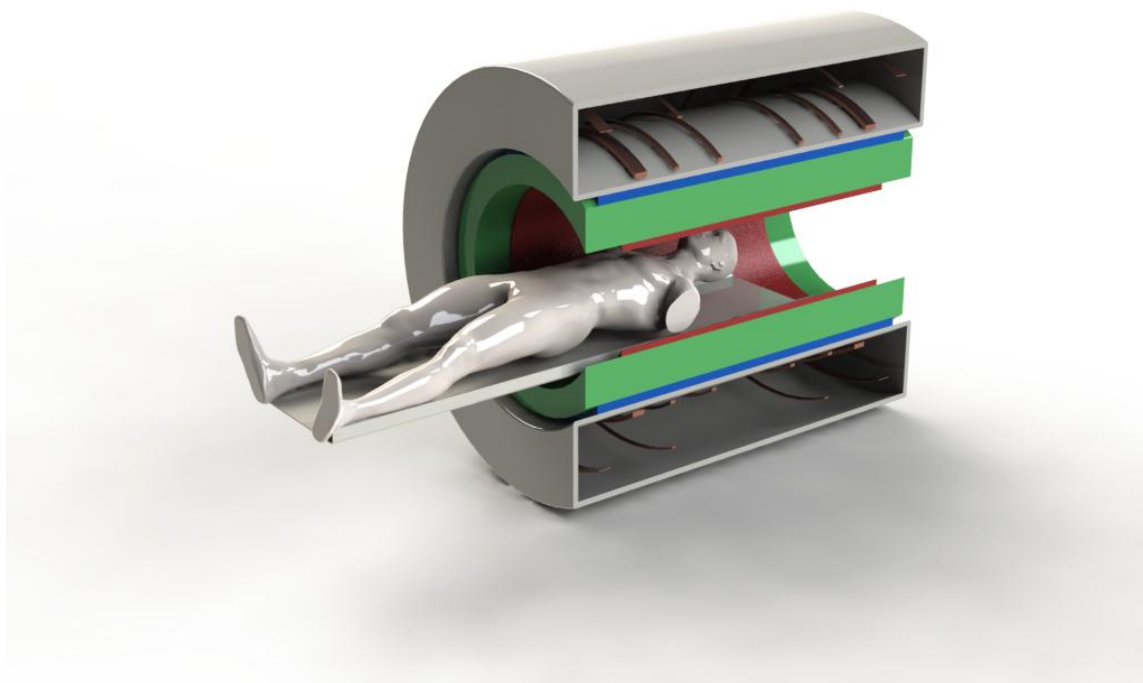


**Figure 1.2:** A schematic representation of a typical MR system. Part of the system is cut away so the various hardware components are visible. The brown bundles inside the gray casing are the superconducting main magnet wire. The shim coils are shown in blue, the gradients in green and the RF coil is represented by the red cylinder. Image courtesy Will Handler.

### 1.3.1 Main magnets

The primary function of the main magnet in an MR scanner is to force a population of magnetic moments to align with the main magnetic field, resulting in a net magnetization of the sample. Because MRI is a very low signal-to-noise (SNR) phenomenon the field produced by the main magnet needs to be very strong, but also time independent and spatially homogeneous. This is achieved in clinical MR systems by the use of

superconducting material, almost always niobium-titanium (Nb-Ti), which can support a high amount of current with negligible resistance. Nb-Ti has a critical superconducting temperature of 10 K, which means it must be continuously cooled in order to remain superconducting. To remain at the critical temperature the superconducting wires are typically immersed in liquid helium, which has a boiling point of 4.2 K. Research scanners have been produced using resistive and permanent magnet technology (6), but superconducting systems remain dominant in the clinical setting.

The ultimate effect that the main magnetic field has on the signal acquired in a MR experiment comes from two separate parts of the imaging process. First, the amount of bulk magnetization present in a sample, as given by equation 1.2, is linearly proportional to  $B_0$ . Second, during the acquisition stage the EMF is dependent on the time derivative of the magnetization vector, given by equation 1.3, which makes the signal proportional to the Larmor frequency as well. Provided  $B_0$  is responsible for both the polarization of the sample and is present during the acquisition of signal, the resulting dependency on the main field is  $B_0^2$ . This dependence on field strength is responsible for the continual trend towards higher field strengths in MRI.

Magnetic field strengths for clinical whole-body systems range from about 0.5 – 3.0 T at present. However, research systems are available up to 7.0 T above. Small animal scanners routinely operate at higher fields, and NMR spectrometers are available at field strengths even higher yet. For clinical MRI current regulations prohibit the use of field strengths over 3.0 T (7).

In addition to being strong, the main field must also be extremely homogeneous. The homogeneity requirement comes from the  $\phi(r,t)$  dependence in the signal equation. The inhomogeneities of the main field must be sufficiently small so they do not dominate the applied gradient ( $\mathbf{G}_{\text{applied}} \gg \mathbf{G}_{\text{inhomo}}$ ). This places a stringent requirement on main field uniformity. At present modern scanners have main magnetic fields that can be homogenous to 1 ppm over 50.0 cm imaging volumes with the help of superconducting and ferromagnetic shims, which will be discussed later. In addition to the spatial homogeneity requirement, the static field must also be relatively homogenous over time.

Superconducting magnets produce fields that can vary less than a  $\mu\text{T}/\text{hour}$ ; a field varying less than a few ppm over the total imaging time would be considered time independent for most MR applications, thus superconducting fields are sufficiently stable for MRI. That is not the case for systems using resistive technology (8).

Aside from the critical properties discussed, other desirable characteristics that must be considered in the design of a main magnet consist of: patient access and comfort, cost of the magnet, fringe field minimization, weight and size.

### 1.3.2 RF coils

Radiofrequency (RF) coils are responsible for both the excitation and acquisition of the MR signal. Looking back at the signal equation it can be seen that the signal received is weighted by the sensitivity profile of the RF coil ( $\mathbf{B}_1(\mathbf{r})$ ). This means that RF field profiles need to be uniform to avoid intensity shading in images, and that more sensitive coils will give larger signals. RF coils are tuned to resonate at the Larmor frequency of the nuclei that is being imaged, which is 63.87 MHz at 1.5 T and 127.7 MHz at 3.0 T for protons.

A single coil can be used to excite the magnetization (transmit) and detect (receive), however, it is also possible to use separate coils. Because desirable characteristics differ for transmission and reception, often two separate coils are used.

The driving quality behind transmit RF coils is the need to generate a homogeneous excitation across the sample. Many types and geometries of transmit coils exist, but because of the homogeneity requirement transmit coils tend to be larger volume coils as compared to receive coils. A very common geometric design for transmit coils is the birdcage coil (9). However, the trend towards higher field MR systems has caused RF engineers to rethink the traditional transmit RF coils (10).

A second consideration in designing an RF transmit coil is the time it takes for the RF coil to tip the magnetization vector into the transverse plane. The angle at which the magnetization vector is tipped (flip angle) is given by:

$$\theta = \gamma B_1 \tau_{rf}. \quad (1.17)$$

So the stronger the  $B_1$  field the less time required for a given flip angle, which is important because time is always paramount in MRI.

Another extremely important aspect of RF transmit coils is power deposition. When transmit fields perturb the magnetization from thermal equilibrium, energy is deposited in the sample as heat via a Faraday induction effect. Guidelines and regulations have been established that dictate acceptable limits on specific absorption rates (SAR) of radiation deposited in the body (7,11). Limiting local SAR values in the human body to approximately 8 W/kg, ensures no significant temperature increase will occur. At 1.5 T the RF wavelengths are long enough that SAR deposition is relatively uniform, but as field strength increases, wavelength decreases, and local hot spots become a major concern.

The two major factors that drive RF receive coil design are the sensitivity profile and noise characteristics of the coil. RF receive coils can take on many geometrical forms as a result of trying to optimize for both of these considerations (12). The sensitivity profile of a receive coil is heavily dependent on its geometry. In particular it is extremely important to get the RF coil as close to the sample as possible. This requirement is evident in a clinical setting, where RF coils have been customized to enclose almost every part of the human body.

The noise in an RF receive coil results from the intrinsic noise in the RF coil itself, and the coupling between the RF coil and the sample (as well as radiation coupling in principle). When sample noise is a dominant factor, reducing the volume of the sample that the coil is sensitive over will reduce the noise. The trade off is that the field of view of the RF coil is reduced – a problem solved by using multiple receive coils.

Phased array RF coils are sets of coils that can have their signals combined to be sensitive over a volume larger than that of any of the individual coils. Smaller coils have better SNR because they have small noise volumes. So it can be beneficial to combine many small coils to image over a certain volume, as compared to just using a single large

coil. For array coils to benefit from the noise reduction associated with smaller coils, the noise of each individual RF coil must be uncorrelated with the others. Parallel imaging techniques that greatly reduce the acquisition times for many types of MR sequences are largely made possible by phased array RF coils (13,14). Phased array coils are also showing promise in dealing with the problems of transmission field homogeneity in higher field MR (15).

### 1.3.3 Gradient coils and shim coils

For ease of explanation and to stay with conventional thought, gradient coils and shim coils will be discussed as separate entities. However, the idea that these sets of coils should, and in the future, hopefully will be thought of as a single set of coils responsible for “dynamic field control” during the imaging process is briefly discussed.

Traditionally in MRI gradient coils and shim coils have been thought of as separate hardware subsystems, each playing a different role in the imaging process. Although each set of coils does in fact play a different role in terms of functionality, they both accomplish the same task, which is to control the magnetic field during the imaging process. To further strengthen the argument that gradient and shim coils should and can be viewed as a single entity, it is noted that each coil is just an individual term in a harmonic expansion of the magnetic field and that gradients play a direct role in the shimming process as the linear shims. Lastly, both types of coils leave their mark on the same term ( $e^{i\phi(\mathbf{r},t)}$ ) in the MR signal equation. For this work it is instructive to think of the gradients as being a special subset of the shim coils that provide the image encoding fields.

#### 1.3.3.1 Gradient coils

The primary responsibility of the gradient coils is to spatially encode the position of the magnetic moments in a sample. They accomplish this task via a linearly varying magnetic field across the sample, which makes the precession frequency, or phase, of the nuclei at each position different. This allows differentiation between locations in the sample and image formation. There are three separate gradient coils in MRI, one for



each Cartesian axis, that produce a magnetic field such that its  $z$ -component varies linearly along the direction that defines that coil:

$$G_x = \frac{\partial B_z}{\partial x} \quad (1.18 \text{ a})$$

$$G_y = \frac{\partial B_z}{\partial y} \quad (1.18 \text{ b})$$

$$G_z = \frac{\partial B_z}{\partial z} . \quad (1.18 \text{ c})$$

$G_x$  is the  $x$ -gradient,  $G_y$  is the  $y$ -gradient and  $G_z$  is the  $z$ -gradient. The  $G_x$  and  $G_y$  gradients are commonly referred to as transverse gradients and the  $G_z$  gradient is known as the longitudinal gradient.

There are numerous properties associated with gradient coils that determine their effectiveness. Among the most important design characteristics are: gradient efficiency, switching speed, gradient uniformity, inductance, and power deposition. Efficiency, uniformity, inductance and resistance are properties of the gradient coil itself, while gradient strength, slew-rate, and power deposition are properties of both the gradient coil and its amplifier together. The gradient strength, measured in mT/m or G/cm, is important because it dictates the resolution that can be achieved for a given imaging time. The switching speed, or slew rate, is measured in mT/m/ms and tells how fast a gradient coil can be turned on and off. Fast imaging applications require gradients that can be switched very quickly (greater than 1.0 kHz). Gradient uniformity is the size of volume over which the gradient field is sufficiently uniform for imaging, and is a major consideration in gradient coil design as it dictates the physical size of the coil, a property that influences almost all other coil characteristics. The inductance and power of a gradient coil are important as they must be considered when selecting an amplifier. In addition to amplifier matching, the power dissipated in a gradient also effects the duty cycle that can be achieved and the need, or lack thereof, for external cooling.

Other aspects that are important to the design of a gradient coil might include: forces and torques on the coil, acoustic noise and patient access. Switching the gradient coils on and off inside the main magnetic field results in large Lorentz forces on the

individual wires themselves and could result in large net forces or torques on the entire structure if one is not careful. This rapid switching also results in significant acoustic noise as the switching frequencies are usually in the audible range.

Evaluating the overall performance of a gradient coil can be a difficult task given that there is a tradeoff between many of the performance metrics for gradient coils. Two quantities that are relevant in quantifying practical gradient performance are: gradient strength and switching speed. These quantities are dependent on not only the gradient coil, but also the amplifier, and are given by:

$$G = \eta I \quad (1.19)$$

$$\text{Slew Rate} = \eta \frac{V}{L}, \quad (1.20)$$

where  $\eta$  is the gradient efficiency in mT/m/A,  $I$  is the current in the coil,  $V$  is the voltage applied, and  $L$  is the inductance of the coil. Comparing different gradient coils via equations 1.19 and 1.20 poses a problem in that the gradient efficiency and inductance of the coil are heavily dependent on the size of the imaging region, size of the coil, and most importantly the number of windings used. One solution is to use figure of merit metrics (16):

$$M_L = \frac{\eta \cdot r^{5/2}}{\sqrt{L}} \quad (1.21)$$

$$M_R = \frac{\eta \cdot r^{5/2}}{\sqrt{R}}, \quad (1.22)$$

where  $r$  is the radius of the coil,  $L$  is the coil inductance, and  $R$  is the coil resistance.  $M_L$  is known as the inductive merit and  $M_R$  is known as the resistive merit and these values are independent of coil size making them acceptable for direct comparison.

Another important aspect of gradient coils is the concomitant magnetic fields that are produced along with the desired linear field variation. The linear field variation that is desired for gradient coils does not in fact exist as a solution to Laplace's equation

without accompaniment of other fields. As an example consider a linearly varying field along  $x$  ( $x$ -gradient):

$$\mathbf{B} = G_0 x \hat{z}. \quad (1.23)$$

If no sources are present then:  $\nabla \cdot \mathbf{B} = 0$ , but:  $\nabla \times (G_0 x) \hat{z} = -G_0 \hat{y}$ , so it can be seen that another field component must be present to satisfy Maxwell's equations. These concomitant magnetic fields can result in image artefacts if sufficiently large, although at higher field MR (1.5 T and up) they are not a major concern.

It was noted in the discussion of radiofrequency coils that the performance of such coils was ultimately limited by the amount of energy deposited in the body. Gradient coils do not cause heating in body tissue because they operate at lower frequencies than RF coils, which means they have lower  $dB/dt$  values. However, another physiological effect limits the full use of their capabilities – peripheral nerve stimulation (17). Peripheral nerve stimulation occurs because the gradient coils are switched on and off rapidly, resulting in time varying magnetic fields that happen to be at the right frequency for reaction with the peripheral nervous system of humans.

For this work a brief look at the history of gradient design and the current state of gradient technology is warranted. Initial gradient design methods were crude yet robust in that they produced coils that were sufficient enough to survive for a significant period of time. The two classic examples of these early “building block” gradient coils are the common Maxwell pair (18) (longitudinal gradient) and the Golay coil (19) (transverse gradient). Both these designs are achieved by expanding the magnetic field generated from an arch of wire and solving for the positions of the arch, such that the only field term left is the one desired. These early types of gradient coils were less efficient and not capable of the switching speeds of today's gradient coils. It was not until the 1980's that the need for faster and stronger gradients was even apparent (20). New imaging techniques began to place higher demands on gradient technology and the result was distributed winding gradient coils. Distributed winding coils are better approximations to continuous current densities than previous coils. A visual comparison of distributed winding coils and early “building block” coils is given in figure 1.3.

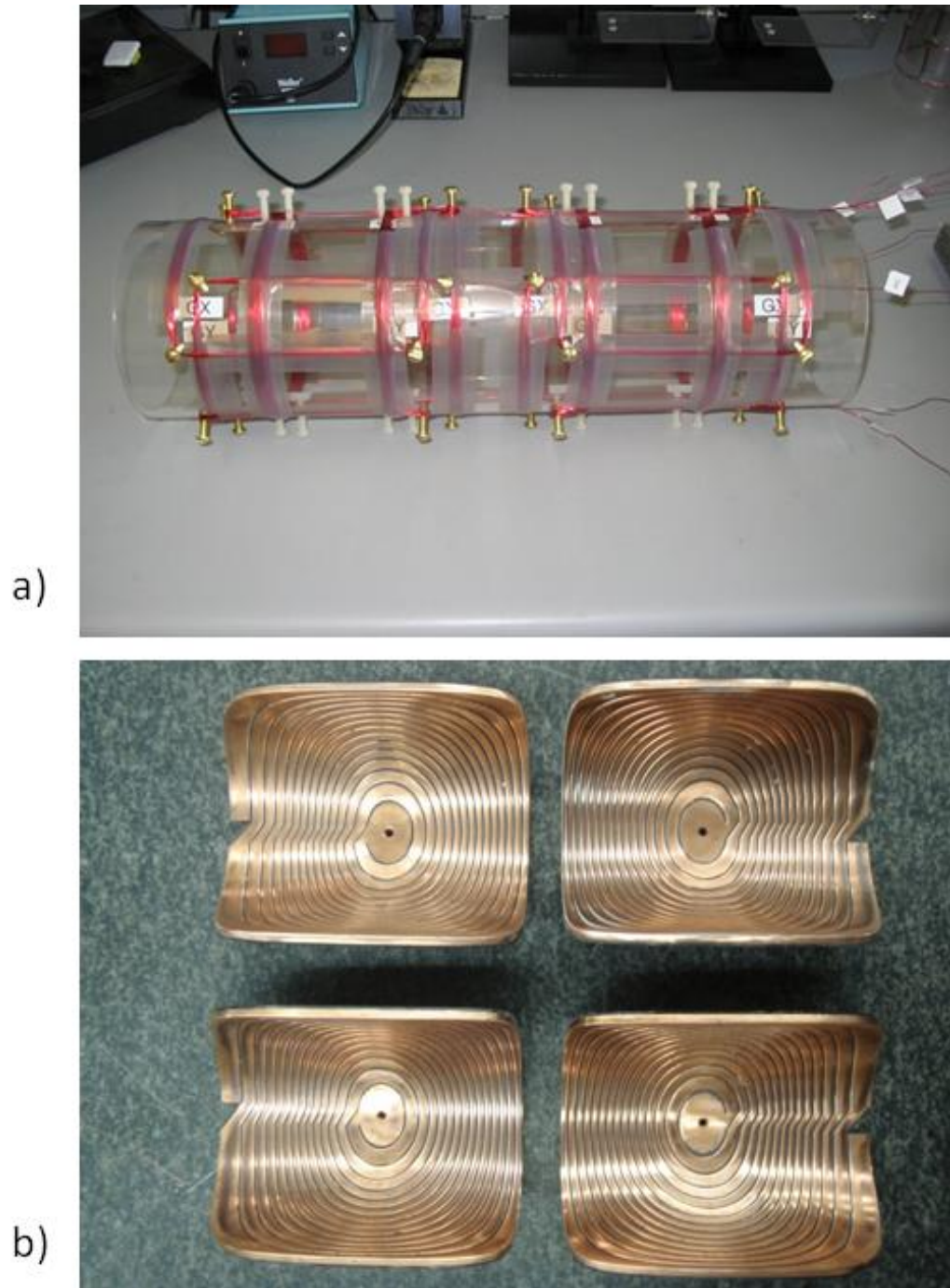


**Figure 1.3:** A picture of two Golan coils wound on a former (a). It can be seen that these types of gradient coils are made up of fairly crude elements. (b) shows the wire pattern for a modern distributed winding gradient coil. The conductors in (b) have not yet been fastened to a former and wired together. Note that these coils are both transverse gradients. Figure 1.3 (a) is courtesy Kyle Gilbert.

Many design methods exist for distributed winding gradient coils: matrix inversion methods (21), stream function methods (22), and target field methods (23), but the basic idea is the same for all. The desired magnetic field profile is parameterized in terms of the current density on a coil former (usually a cylinder), and then that current density is solved for. An approximation method is then used to determine where to place wires to best represent that continuous current density. Many of these methods have the ability to optimize gradient designs with respect to particular parameters, such as power or inductance (24,25). The technique for this is to parameterize not just the magnetic field but the desired characteristic in terms of current density and minimize an error function that contains both. Modern gradient design techniques have now pushed past the restriction to simple geometries using Boundary Element (BE) methods (26,27,28) and the ability to create gradient coils on any arbitrary geometry is now possible. Today's state of the art clinical whole body gradient coils are capable of 50.0 mT/m and slew rates of several hundred mT/m/ms. Research gradients are available that routinely reach much higher gradient strengths and much faster slew rates, although over smaller imaging volumes, making them not directly comparable (29).

### 1.3.3.2 Shim coils

As was mentioned above, the shim coils in an MR system influence the  $e^{i\phi(\mathbf{r},t)}$  term in the signal equation, just like the gradients. However, the goal of the shim coils is not to create a frequency or phase dispersion across the sample, but to correct for the one that exists from sources other than the gradients.

Shim coils accomplish this correction by producing specific magnetic field variations that attempt to cancel out the field variations that arise from  $B_0$  inhomogeneity, and other sources, which will be discussed in further detail below. There are typically two sub-categories of shim coils in a conventional MR scanner. The first category is passive shim coils. Passive shim coils are responsible for correcting (shimming) the field distortions that result from imperfections in the system and the magnetic environment around the system. There are often two sets of passive shims: a set of superconducting wire wound shim coils housed inside the cryostat with the main magnet windings, and a set of ferromagnetic shims placed inside the scanner bore. These ferromagnetic shims are

typically trays of iron discs that are strategically placed to correct for field distortions. Both the superconducting and ferromagnetic passive shims are optimized when the magnet is installed, and are rarely adjusted afterwards.

The second category of shim coils, and the one of greatest importance to this work, is room temperature resistive shims. Just like the gradient coil set, these shim sets consist of resistive wire wound electromagnets grouped together inside the bore of the scanner. What makes these different from passive shims is that the current can be adjusted to change the field variation that the shim set creates. Room temperature shims must correct for field distortions that are sample specific (more on sample specific distortions later), which means they must be adjustable and capable of generating a variety of different field variations.

The most common method for generating a shim set that is capable of correcting a wide variety of fields is to make individual coils that approximate orthogonal field variations over the volume of interest and use those coils in linear combinations with each to approximate the necessary shim field. Because there is no current flowing in the imaging region over which shimming is to occur, the coils of interest are ones that satisfy Laplace's equation. It has been described by Roméo and Hoult (30) that the shim field can be characterized by spherical harmonics which are solutions to Laplace's equation:

$$B_z(r, \phi, \theta) = \sum_{l=0}^{\infty} \sum_{m=-l}^l P_l^m(\cos\theta) r^l (A_{lm} \cos(\phi) + B_{lm} \sin(\phi)), \quad (1.24)$$

where  $P_l^m$  are the associated Legendre polynomials. The desired field variation for each shim coil is given by the corresponding harmonic term, and solving for the current necessary on a coil former is accomplished via any of the methods previously discussed for gradients. Modern shim sets typically consist of all zero, first and second order spherical harmonics, and often third order coils are added for further corrective power. The more orders that are added the greater the shimming ability, but bore space and the Biot-Savart law ultimately place constraints on how many shims can effectively be added. Table 1.1 gives the name and functional form of spherical harmonic shims up to third order.

**Table 1.1:** The name and functional form for the most common shim orders.  $l$  and  $m$  are given by equation 1.24.

<b>l</b>	<b>m</b>	<b>Shim Name</b>	<b>Functional Form</b>
1	0	$z$	$z$
1	1	$x$	$x$
1	-1	$y$	$y$
2	0	$z^2$	$z^2 - (x^2 + y^2)/2$
2	1	$zx$	$zx$
2	-1	$zy$	$zy$
2	2	$x^2 - y^2$	$x^2 - y^2$
2	-2	$xy$	$2xy$
3	0	$z^3$	$z^3 - 3z(x^2 + y^2)/2$
3	1	$z^2x$	$z^2x - x(x^2 + y^2)/4$
3	-1	$z^2y$	$z^2y - y(x^2 + y^2)/4$
3	2	$z(x^2 - y^2)$	$z(x^2 - y^2)$
3	-2	$zxy$	$zxy$
3	3	$x^3$	$x^3 - 3xy^2$
3	-3	$y^3$	$3x^2y - y^3$

Other unconventional shim systems exist outside the standard spherical harmonic room temperature shim set that deserve some attention. One such method uses ferromagnetic material to shim sample specific field distortions (31). Because certain parts of the human anatomy are frequently imaged, it is possible to create an array of ferromagnetic material that accurately shims part of the human body, provided that the field distortions from person to person are similar enough. A second type of unconventional shim set makes use of many circular loops, like an RF array, to construct the necessary shim fields (32). This method is inherently low power, and gives the ability to produce higher order harmonic terms that aren't generally available in a traditional shim set. Furthermore, it has the ability to produce field variations that are not approximated by a sum of low order spherical harmonics. This method attempts to overcome the limitations placed on shim sets by the bore and Biot-Savart law. Another technique for overcoming these constraints is introduced in chapter 4 of this work.

## 1.4 Magnetic field imperfections

Throughout this chapter the major imaging fields in MR have been discussed (the static main field, the radiofrequency fields, and the gradient fields) and the idea that these

magnetic fields are not perfect in reality has been introduced through the concepts of homogeneity and the need for shim coils. Magnetic field imperfections are very common in MR. They result from many different sources and can affect any one of the fields necessary for imaging. In this section several sources of magnetic field imperfections will be discussed: system and sample related  $B_0$  inhomogeneities, and eddy currents.

As has been the theme so far, field imperfections impact the  $e^{i\phi(\mathbf{r},t)}$  term in the signal equation. It was mentioned previously that there is a phase dispersion across the sample that is related to the applied gradient field. However, if field imperfections exist then the phase across the sample is not just a result of the applied gradient ( $\mathbf{G}(\mathbf{r}, t)$ ), but also any inhomogeneities ( $\Delta B_0$ ). If these effects are accounted for, the phase accrued is actually:

$$\phi(\mathbf{r}, t) = -\gamma \int_0^t (\mathbf{G}(\mathbf{r}, \tau) \cdot \mathbf{r} + \Delta B_0(\mathbf{r}, \tau)) d\tau. \quad (1.25)$$

The first type of magnetic field distortions are those that arise from imperfections in the system and its immediate environment. These kinds of imperfections are usually quite static in nature, although not always. What separates them from others is that they are corrected for when the MR system is installed and do not require constant attention. These field distortions may occur because the windings inside an MR system may not be positioned perfectly. No matter how careful the manufacturing process, windings cannot be exact, and even so, they can experience considerable electromagnetic and gravitational forces, which often results in settling over time. Inhomogeneities can also arise from the surroundings of an MR system. Steel beams in the walls or support structures of the building can become magnetized and degrade the imaging field. Ferromagnetic material placed near the scanner for the purpose of shielding can give rise to field distortions. There can be many field distortions associated with the MR environment, but if they are static then they can be corrected for during installation, just like the system imperfections.

A second category of field distortions results from the samples themselves, and these are typically harder to deal with, as they have to be corrected on a sample by



sample basis. For most materials the magnetization is sustained by the field and is proportional to it (paramagnetic and diamagnetic). These materials are called linear media and the induction field, the auxiliary field, and the magnetization are related via the following equations (33):

$$\mathbf{B} = \mu\mathbf{H} \quad (1.26)$$

$$\mathbf{M} = \chi\mathbf{H}, \quad (1.27)$$

where  $\mu$  is the magnetic permeability, and  $\chi$  is the magnetic susceptibility of the material. For paramagnetic material:  $\chi > 0$ , and for diamagnetic material:  $\chi < 0$ . Biological tissue has a magnetic susceptibility of approximately -9.2 ppm and air has a magnetic susceptibility of approximately 0.3 ppm, which can result in small but significant field distortions at air-tissue boundaries. The magnetic permeability and magnetic susceptibility are related by:

$$\mu = \mu_0(1 + \chi). \quad (1.28)$$

Using equations 1.26 – 1.28 the magnetic field can be expressed as:

$$\mathbf{B} = \frac{1+\chi}{\chi}\mu_0\mathbf{M}. \quad (1.29)$$

So it can be seen that the magnetic field can vary across different material and the discontinuities at boundaries can give rise to field distortions.

As a practical example consider a spherical piece of material with a magnetic susceptibility that is different from its surroundings placed in a magnetic field:  $\mathbf{B} = B_0\hat{z}$ . The magnetic field outside can be approximated as a constant term plus a dipole field:

$$\mathbf{B}_{out}(\mathbf{r}) = B_0\hat{z} + \frac{\mu_0}{4\pi} \frac{3(\mathbf{m}\cdot\hat{r})\hat{r} - \mathbf{m}}{r^3}, \quad (1.30)$$

Where the magnetic dipole moment of the sphere is calculated as:

$$\mathbf{m} = \frac{4\pi}{3}a^3M(\chi)\hat{z}. \quad (1.31)$$

The field inside is given by equation 1.29:

$$\mathbf{B}_{in} = \frac{1+\chi}{\chi} \mu_0 M(\chi) \hat{z}. \quad (1.32)$$

To obtain a solution for  $M(\chi)$  boundary conditions must be considered. First the normal component of  $\mathbf{B}$  and the tangential components of  $\mathbf{H}$  must be continuous across the spherical surface, also very far from the sphere the field must be  $B_0$ . Given these conditions:

$$\mathbf{M}(\chi) = \frac{3\chi}{3+\chi} \frac{B_0}{\mu_0} \hat{z}. \quad (1.33)$$

Combining equations 1.31-1.33 the solutions for the fields outside and inside the magnetic sphere are:

$$\mathbf{B}_{out} = B_0 \left( \hat{z} + \frac{\chi}{3+\chi} \left( \frac{a}{r} \right)^3 (3 \cos \theta \hat{r} - \hat{z}) \right) \quad (1.34)$$

$$\mathbf{B}_{in} = 3B_0 \hat{z} \frac{1+\chi}{3+\chi}. \quad (1.35)$$

Using equations 1.34 and 1.35 the phase shift that results from the magnetic field difference can be calculated, making simple models such as this quite useful. Figure 1.4 shows the magnetic field profile for a spherical piece of stainless steel placed in a 1.0 T uniform field.

Sample induced inhomogeneities are the dominant source of field distortions in MRI. They can be very difficult to deal with because they are different for every sample. These inhomogeneities range widely in size, and can be quite severe in places like the sinus cavity. More exotic situations, such as metallic medical implants, can be so severe that correction, and thus imaging, is not even possible in the vicinity of the implant (34).

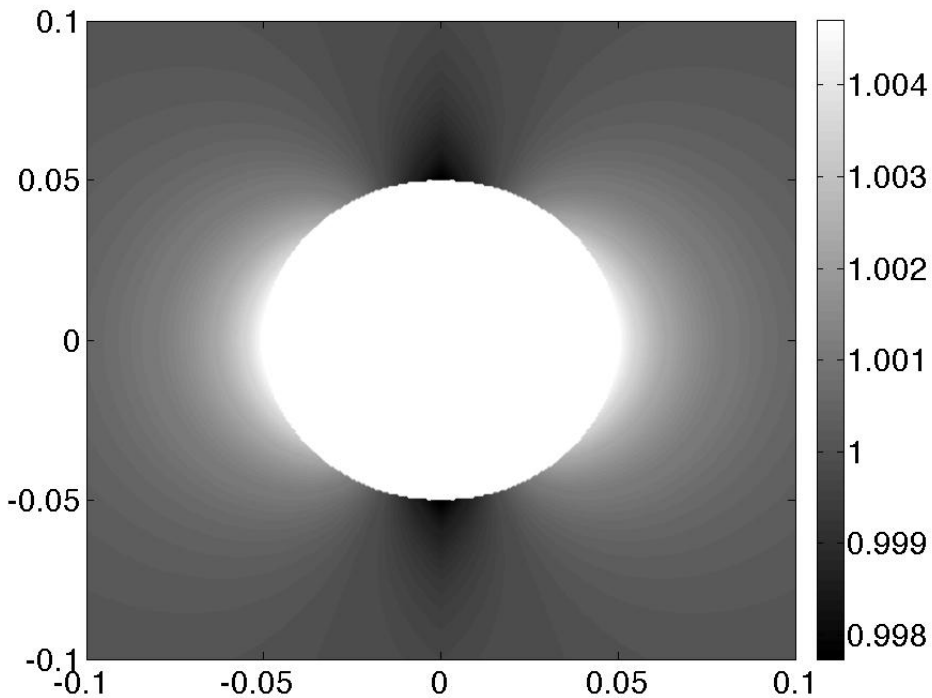


**Figure 1.4:** The magnetic field profile on a plane cut through the center of a spherical piece of stainless steel (10.0 cm diameter) placed in a 1.0 T uniform field.

The last type of field error this chapter will address is that of eddy currents. Eddy currents are not usually mentioned alongside  $B_0$  inhomogeneities, but they are magnetic field imperfections nonetheless.

The dominant cause of eddy currents in MR is the rapidly switching gradient fields. The MR system itself is constructed of many conducting materials, some of which are held at very low temperatures inside or in close proximity to the cryostat. These conductors have the ability to house eddy currents if exposed to large time varying magnetic fields, which is common to MRI in the form of gradient fields. The mechanism for eddy current induction is a two step process. First time-varying magnetic fields give rise to induced electric fields via Faraday's Law:

$$\oint_C \mathbf{E} \cdot d\mathbf{l} = -k \frac{d}{dt} \int_S \mathbf{B} \cdot d\mathbf{A}. \quad (1.36)$$

Then, if a conductor is present, the induced electric fields result in a force on the electrons:

$$\mathbf{F} = q\mathbf{E}, \quad (1.37)$$

which gives rise to eddy currents.

Because of the symmetry of the MR system the eddy fields generally mirror the pulsed gradient fields that caused them, resulting in less efficient gradients. However, this is not always the case (35). Time scales for eddy currents in MR vary widely from a few milliseconds to well over a second for eddy currents that exist in the coldest structures of the MR system (36). These long time-constant eddy currents are extremely problematic for imaging, as settling is often required before imaging can continue. The magnitude of an eddy current is heavily dependent on the system in question, particularly, the distance between the switching coil and the conducting structures.

There are two standard and widely employed methods for dealing with eddy currents generated via the gradient coil – pre-emphasis and shielding. Pre-emphasis is a technique that alters the current waveform sent to the gradient coil, such that the gradient pulse plus the eddy current it generates will give the desired gradient waveform. Shielding the gradient coils is also a common method. Almost all whole-body gradient sets today are actively shielded, which involves placing a second coil between the initial gradient coil and the rest of the MR system so the field from the initial gradient will be cancelled at, and beyond, the radius of the shielding coil. This is a technique that will be discussed heavily throughout this work.

## 1.5 Thesis overview

This thesis describes advancements made in the design and development of insert gradient and shim technology. The same design principles applied to insert coils have also been extended and applied to the fringe field problem posed by MRI.

Chapter 2 examines the size and timing associated with eddy currents generated using a small animal gradient insert coil. A custom insert gradient coil was designed and

built specifically to measure the construction tolerances associated with shield placement. Eddy current measurements were conducted in a 7.0 T head only Varian scanner as a function of the relative shield position with respect to the primary coils. Several unique eddy currents were isolated and reported.

Chapter 3 outlines a new design tool that allows for shielding coils to be optimized over any arbitrary geometry without the constraints of previous methods. This new design method is compared to previous techniques for validation and then applied to a more exotic situation that extends beyond the capabilities of older analytical methods. A version of this chapter has been submitted to IEEE Transactions on Magnetic for publication.

In chapter 4 a shim set is designed for the purpose of dynamic shimming, a technique that requires shim currents to be updated during an acquisition. This high power customized shim set is designed, fabricated and bench tested. Performance and field measurements are reported and the technical challenges associated with designing and building such an insert shim set are discussed.

In chapter 5 the minimum energy shielding method presented in chapter 3 is extended and applied to several shielding applications involving the fringe field of an MR system. Large room-size active shields are designed to limit the extent of the magnetic field from a 1.0 T MR system. A smaller cabinet-sized shield is designed for the purpose of protecting non-MR compatible equipment. Lastly, two smaller multi-layer shields are designed to react dynamically to motion relative to the MR system. The performance of the shields are reported and the practical feasibility is discussed.

Finally chapter 6 discusses the conclusions that can be drawn from the work presented. Work that has yet to be completed along with interesting future directions for the methods outlined in this thesis are also discussed.

## 1.6 References

1. Haacke EM, Brown RW, Thompson MR, Venkatesan R. *Magnetic Resonance Imaging: Principles and Sequence Design*. New York: John Wiley & Sons Inc.; 1999.
2. Bernstein MA, King KF, Zhou XJ. *Handbook of MRI Pulse Sequences*. Burlington: Elsevier Academic Press; 2004.
3. Cowan B. *Nuclear Magnetic Resonance and Relaxation*. Cambridge: Cambridge University Press; 1997.
4. Levitt MH. *Spin Dynamics: Basics of Nuclear Magnetic Resonance*. West Sussex: John Wiley & Sons Ltd.; 2001.
5. Bloch F. 1946 Nuclear Induction. *Physical Review*;70(7-8):460-474.
6. Gilbert KM, Handler WB, Scholl TJ, Odegaard JW, Chronik BA. 2006 Design of field-cycled magnetic resonance systems for small animal imaging. *Physics in Medicine and Biology*;51(11):2825-2841.
7. Zaremba LA. FDA Guidelines for Magnetic Resonance Equipment Safety. In: Administration FaD, editor. Center for Devices and Radiological Health; 2011.
8. Gilbert KM, Scholl TJ, Handler WB, Alford JK, Chronik BA. 2009 Evaluation of a Positron Emission Tomography (PET)-Compatible Field-Cycled MRI (FCMRI) Scanner. *Magnetic Resonance in Medicine*;62(4):1017-1025.
9. Hayes CE, Edelstein WA, Schenck JF, Mueller OM, Eash M. 1985 An Efficient, Highly Homogeneous Radiofrequency Coil for Whole-Body Nmr Imaging at 1.5-T. *Journal of Magnetic Resonance*;63(3):622-628.
10. Ibrahim TS, Lee R, Baertlein BA, Abduljalil AM, Zhu H, Robitaille PML. 2001 Effect of RF coil excitation on field inhomogeneity at ultra high fields: A field optimized TEM resonator. *Magnetic Resonance Imaging*;19(10):1339-1347.
11. Collins CM, Li SZ, Smith MB. 1998 SAR and B-1 field distributions in a heterogeneous human head model within a birdcage coil. *Magnetic Resonance in Medicine*;40(6):847-856.
12. Doty FD, Entzminger G, Kulkarni J, Pamarthy K, Staab JP. 2007 Radio frequency coil technology for small-animal MRI. *Nmr in Biomedicine*;20(3):304-325.

13. Sodickson DK, Manning WJ. 1997 Simultaneous acquisition of spatial harmonics (SMASH): Fast imaging with radiofrequency coil arrays. *Magnetic Resonance in Medicine*;38(4):591-603.
14. Boesiger P, Pruessmann KP, Weiger M, Scheidegger MB. 1999 SENSE: Sensitivity encoding for fast MRI. *Magnetic Resonance in Medicine*;42(5):952-962.
15. Katscher U, Bornert P, Leussler C, van den Brink JS. 2003 Transmit SENSE. *Magnetic Resonance in Medicine*;49(1):144-150.
16. Turner R. 1993 Gradient Coil Design - a Review of Methods. *Magnetic Resonance Imaging*;11(7):903-920.
17. Chronik BA, Rutt BK. 2001 Simple linear formulation for magnetostimulation specific to MRI gradient coils. *Magnetic Resonance in Medicine*;45(5):916-919.
18. Bangert V, Mansfield P. 1982 Magnetic-Field Gradient Coils for Nmr Imaging. *Journal of Physics E-Scientific Instruments*;15(2):235-239.
19. Golay M; Magnetic field control apparatus. US patent 3,515,979. 1957 November 4.
20. Suits BH, Wilken DE. 1989 Improving Magnetic-Field Gradient Coils for Nmr Imaging. *Journal of Physics E-Scientific Instruments*;22(8):565-573.
21. Wong EC, Jesmanowicz A, Hyde JS. 1991 Coil Optimization for Mri by Conjugate-Gradient Descent. *Magnetic Resonance in Medicine*;21(1):39-48.
22. Edelstein W, Schenck J; A stream function method for coil construction. U.S. 1987.
23. Turner R. 1986 A Target Field Approach to Optimal Coil Design. *Journal of Physics D-Applied Physics*;19(8):L147-L151.
24. Carlson JW, Derby KA, Hawryszko KC, Weideman M. 1992 Design and Evaluation of Shielded Gradient Coils. *Magnetic Resonance in Medicine*;26(2):191-206.
25. Turner R. 1988 Minimum Inductance Coils. *Journal of Physics E-Scientific Instruments*;21(10):948-952.
26. Pissanetzky S. 1992 Minimum Energy Mri Gradient Coils of General Geometry. *Measurement Science & Technology*;3(7):667-673.

27. Lemdiasov RA, Ludwig R. 2005 A stream function method for gradient coil design. *Concepts in Magnetic Resonance Part B-Magnetic Resonance Engineering*;26B(1):67-80.
28. Poole M, Bowtell R. 2007 Novel gradient coils designed using a boundary element method. *Concepts in Magnetic Resonance Part B-Magnetic Resonance Engineering*;31B(3):162-175.
29. Chronik BA, Alejski A, Rutt BK. 2000 Design and fabrication of a three-axis edge ROU head and neck gradient coil. *Magnetic Resonance in Medicine*;44(6):955-963.
30. Romeo F, Hoult DI. 1984 Magnet Field Profiling - Analysis and Correcting Coil Design. *Magnetic Resonance in Medicine*;1(1):44-65.
31. Juchem C, Muller-Bierl B, Schick F, Logothetis NK, Pfeuffer J. 2006 Combined passive and active shimming for in vivo MR spectroscopy at high magnetic fields. *Journal of Magnetic Resonance*;183(2):278-289.
32. Juchem C, Nixon TW, McIntyre S, Rothman DL, de Graaf RA. 2010 Magnetic field modeling with a set of individual localized coils. *Journal of Magnetic Resonance*;204(2):281-289.
33. Jackson JD. *Classical Electrodynamics*. New York: John Wiley & Sons Inc.; 1998.
34. Ganapathi M, Joseph G, Savage R, Jones AR, Timms B, Lyons K. 2002 MRI susceptibility artefacts related to scaphoid screws: The effect of screw type, screw orientation and imaging parameters. *Journal of Hand Surgery-British and European Volume*;27B(2):165-170.
35. Gilbert KM, Gati JS, Klassen LM, Menon RS. 2010 A cradle-shaped gradient coil to expand the clear-bore width of an animal MRI scanner. *Physics in Medicine and Biology*;55(2):497-514.
36. Liu Q, Hughes DG, Allen PS. 1994 Quantitative Characterization of the Eddy-Current Fields in a 40-Cm Bore Superconducting Magnet. *Magnetic Resonance in Medicine*;31(1):73-76.



## Chapter 2

### 2 Construction tolerances of small animal insert gradient coils

#### 2.1 Introduction

Many applications in MR imaging benefit from increased gradient strength and faster switching times, and numerous new applications are emerging that place similar demands on shim coils (1,2,3). These stronger, faster gradient and shim sets have the potential to interact with each other and with the conducting structures of the MR system, which give rise to eddy currents. Eddy currents are problematic for many MR applications (4,5). Decreased system stability can result from rapidly switched electromagnets coupling with the superconducting coils of the main magnet, particularly even-order zonal coils. Aside from causing image artefacts, the induced currents deposit power in the cold structures of the MR system and can cause increased helium boil-off.

Several methods exist to minimize eddy currents in MR imaging. A common method is to apply a pre-emphasis pulse to cancel eddy current effects, a compensation technique that requires prior knowledge about the eddy currents that are induced (6,7,8). Another widely employed method is to add shielding for the coils that are causing the eddy currents (9). Shielding can be accomplished using either passive shields that make use of induced currents, a method that is no longer common, or active shields driven in unison with the primary coil. Both pre-emphasis and active shielding are standard features on virtually all commercially available MR systems.

Limited practical work has been done in the area of eddy current characterization for different types of gradient coils (10,11,12). Both the design and construction of gradient and shim insert coils give rise to imperfections in the positioning of primary and secondary current windings. Efforts to address the effects of construction and alignment tolerances of shielded gradient coils in a theoretical setting have been made (13); however, the issue of physically measuring these effects has largely been unexplored. Modern CNC equipment can operate to tolerances as small as 0.1 mm or less, which

results in extremely accurate wire patterns for a single coil. However, in an insert coil that contains multiple coils and primary-shield pairs that procedure of coil alignment with respect to other coils can introduce considerable uncertainty. Often the result is a set of electromagnets with very accurate current distributions that are offset with one another.

The purpose of this work is to measure the construction tolerances associated with shield positioning in a shielded gradient insert coil. Insert coils differ from whole body gradient sets in that they are located further from the conducting structures of the MR system, which places less stringent requirements on the positioning of shielding coils with respect to primary coils. A special two-axis ( $x$ , *i.e.* transverse and  $z$  *i.e.* longitudinal) shielded gradient insert coil was constructed for this experiment. This shielded insert is unique in that both the transverse and longitudinal shields can be reproducibly positioned with respect to the primary coils for the purpose of measuring the eddy current effects related to any shield positioning error.

## 2.2 Methods

### 2.2.1 Gradient coil design

Electromagnetic design techniques for gradient and shim coils fall into two rather broad categories: analytical methods (14,15) and numerical methods (16,17). Analytical design methods are typically used for simple coil geometries, such as cylinders, planes or even spheres. Numerical methods can be equally effective at designing coils with simple geometries, but have an advantage for more convoluted designs at the expense of additional complexity and computation time.

Cylindrical geometry gradient coils were designed for this study using a straightforward analytical Fourier series minimization method (18). This method was implemented to design gradient coils of predetermined fixed lengths by expanding the current density over a specified interval as a Fourier series. Outside the interval the current density is set to zero. Magnetic field deviation and resistance are expressed in terms of the Fourier transform of the current density, which allows for a functional,  $U$ , that reflects these parameters to be minimized:

$$U = \sum_{q=1}^Q [B_{z,q} - B_z(r_q)]^2 + \beta P. \quad (2.1)$$

Here  $B_{z,q}$  represents the set of target field points and  $B_z(r_q)$  is the set of calculated field values at the each target point. For the designs in this study 21 target points were used.  $\beta$  is the weighting factor for the power term ( $P$ ), which is determined in an iterative fashion by comparing coil designs.

The current density for the required shielding coils was calculated using an analytical method previously developed for use with cylindrical coils (19). In this method, the shielding current density is expressed as a filtered and scaled version of the primary coil current density. The scaling function is a ratio of the radii of the primary and shield coils for cylindrical coils:

$$j_z^m(k) = -J_z^m(k) \frac{R_p^2 I_m'(kR_p)}{R_s^2 I_m'(kR_s)} \quad (2.2)$$

$$j_\phi^m(k) = -J_\phi^m(k) \frac{R_p I_m'(kR_p)}{R_s I_m'(kR_s)}. \quad (2.3)$$

Here  $j_z^m$  and  $j_\phi^m$  represent the Fourier transforms of the  $z$ - and  $\phi$ -components of the shielding current density, and  $J_z^m$  and  $J_\phi^m$  are the Fourier transforms of the  $z$ - and  $\phi$ -components of the primary current density. The radii of the primary and shield are given by  $R_p$  and  $R_s$ , and  $I_m$  is a modified Bessel function of the first kind.

### 2.2.2 Gradient coil construction

The shielded transverse and longitudinal gradients were constructed using two different techniques because the fabrication of the longitudinal gradient was much simpler than that of the transverse. Since the azimuthal component of current density is constant in both the longitudinal gradient and shield, a winding groove could be machined directly into a cylindrical former as concentric loops. A “trough” was machined in the longitudinal direction all the way down the length of the former for the purpose of joining

each loop of current to the other (figure 2.1). The formers used were two lengths of Schedule 40 polyvinyl chloride (PVC) pipe with inner and outer diameters of 12.7 cm and 14.1 cm for the primary, and 20.3 cm and 21.9 cm for the shield, which are shown in figure 2.2. The  $z$ -gradient (longitudinal) primary wire pattern was machined directly into the 14.1-cm-diameter former and the corresponding shielding wire pattern was milled directly into the 10.95-cm-diameter former, both to a depth of 2.0 mm from the outer edge. 10-gauge copper wire was then wound into each winding form and the primary coil and shielding coil were then wired in series for simultaneous operation.

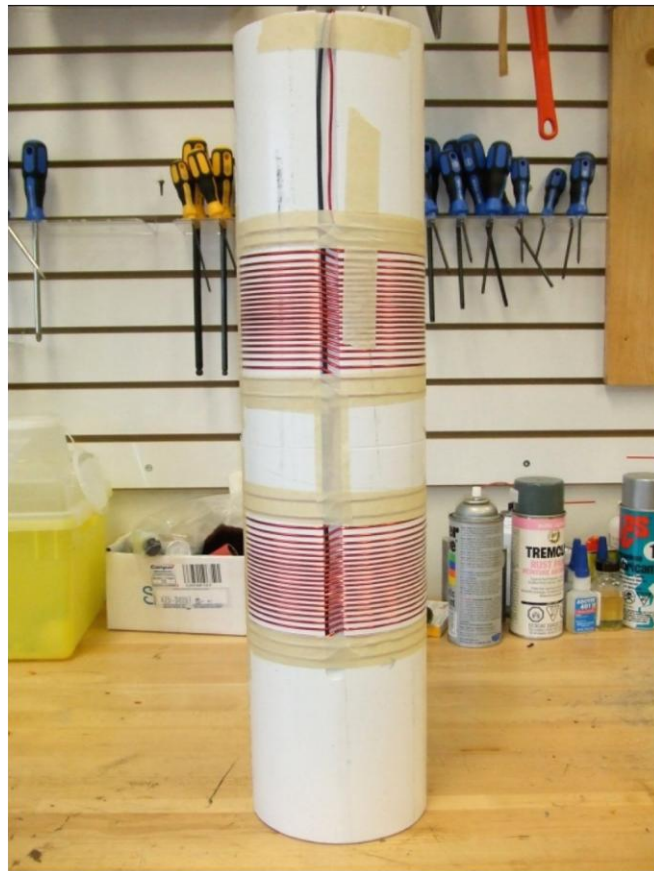


**Figure 2.1:** The primary  $z$ -gradient wire pattern that has been machined into a PVC former. Consecutive loops were cut into the former and the wire was jogged between loops.



**Figure 2.2:** Both the  $z$ -primary and  $z$ -shield before they were connected together in series.

The transverse gradient was constructed by milling the wire pattern into a 2.91-mm-thick sheet of copper using a 1.2-mm-diameter cutting tool. This produces the “negative” of the desired wire pattern, which was then used as the current carrying portion of the gradient coil (12, 20). This method allows for improved thermal properties through reduced resistance, as a greater amount of copper is used in the current-carrying portion of the coil. The minimum resulting conductor width was 2.0 mm. A layer of flexible low-viscosity epoxy (10-3004 epoxy adhesive, Epoxies, Etc, Cranston, USA) was applied to the back of each section of the coil to hold the copper conductors in place during the milling process. The transverse gradient and shielding coils were constructed one quadrant at a time (figure 2.3).

The gradient thumbprints were rolled to a specified radius prior to being attached to their respective cylindrical forms. To aid in the rolling process, the quadrants, comprised of copper and epoxy backing, were heated to approximately 60° C. The epoxy

helped to keep the wire patterns from distorting during the rolling process. After rolling, each section was bonded to the appropriate former used to wind the longitudinal coil. All four quadrants were individually wired together for the primary and shielding coils and finally, the primary and shielding coils were wired together in series, so as they could be driven in unison. As a final step, another layer of epoxy was applied to both the primary and shielding coils to reinforce the bonded wires during operation.



**Figure 2.3:** The individual quadrants of the y-primary coil prior to being rolled and fastened to the formers.

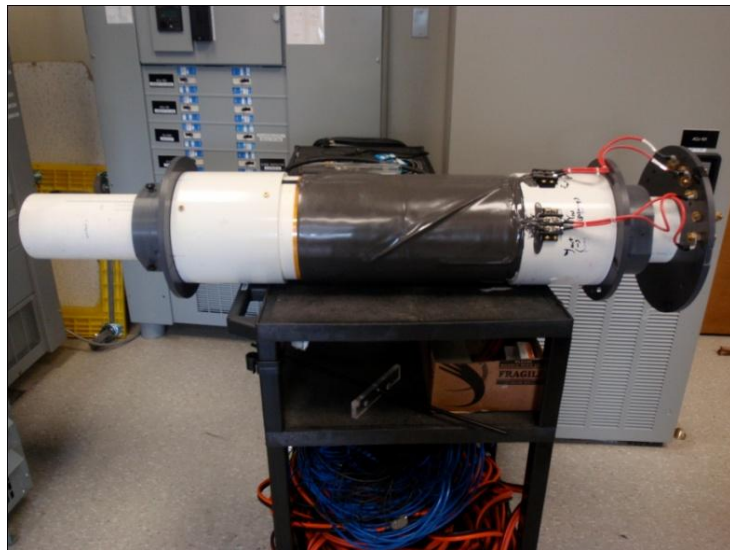


**Figure 2.4:** The fully constructed insert coil with its mechanical collars and mounting bracket is shown.

Construction of the coil supporting structure for this gradient insert was fairly complex compared to that of more standard insert coils. In order to examine the effects of shield misalignment, a supporting structure for the shield was designed to facilitate reproducible translation of the shield in three dimensions from its ideal position. To achieve this, purpose-built PVC collars were constructed that fastened the shield to the primary coil allowing for relative positioning, which are shown in figure 2.4. The collars were fastened to the shield former using brass screws and were machined to slide smoothly along the primary former. This gave freedom of motion (figure 2.5) in both the azimuthal ( $\pm 90^\circ$  in  $2^\circ$  increments) and longitudinal ( $-50.0$  to  $+150.0$  mm in  $1.0$  mm increments) directions with setscrews available for fixing position. A series of holes were also machined in the collars to allow for radial displacement ( $\pm 50.0$  mm in  $5.0$  mm increments). The completed insert coil assembly is shown in figure 2.4.

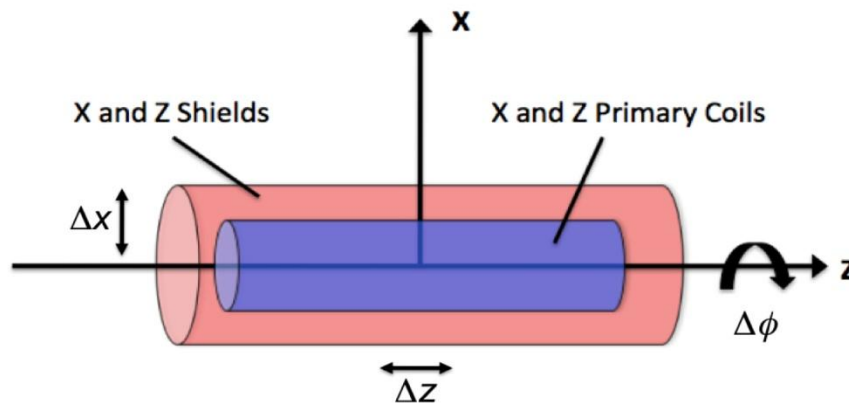


**Figure 2.5:** The geometry of the gradient insert coil and the range of motion available for the shield to move with respect to the primary.

An artificial bore made of  $1.0$  cm thick copper, which represents approximately five skin depths at  $1.0$  kHz, was fabricated to mimic a small-bore scanner that could be numerically simulated. The artificial bore was  $90.0$  cm in length and had a  $35.8$ -cm outer-diameter and  $33.8$ -cm inner-diameter. The copper sheet was rolled into a cylinder

using a hydraulic roller and the seam was lap-joined and soldered to achieve a continuous conducting cylindrical surface (figure 2.6).

### 2.2.3 Bench testing

Inductance and resistance measurements of the finished insert coil were made at three different frequencies: 0.012, 0.1, and 1.0 kHz with an INSTEK LCR-800 LCR meter outside of the MR system. These measurements were recorded as a function of relative shield position in all three directions (azimuthal, longitudinal and radial). The measurements were then repeated with the gradient insert placed inside the artificial copper bore, but not inside the actual MR system (figure 2.6).

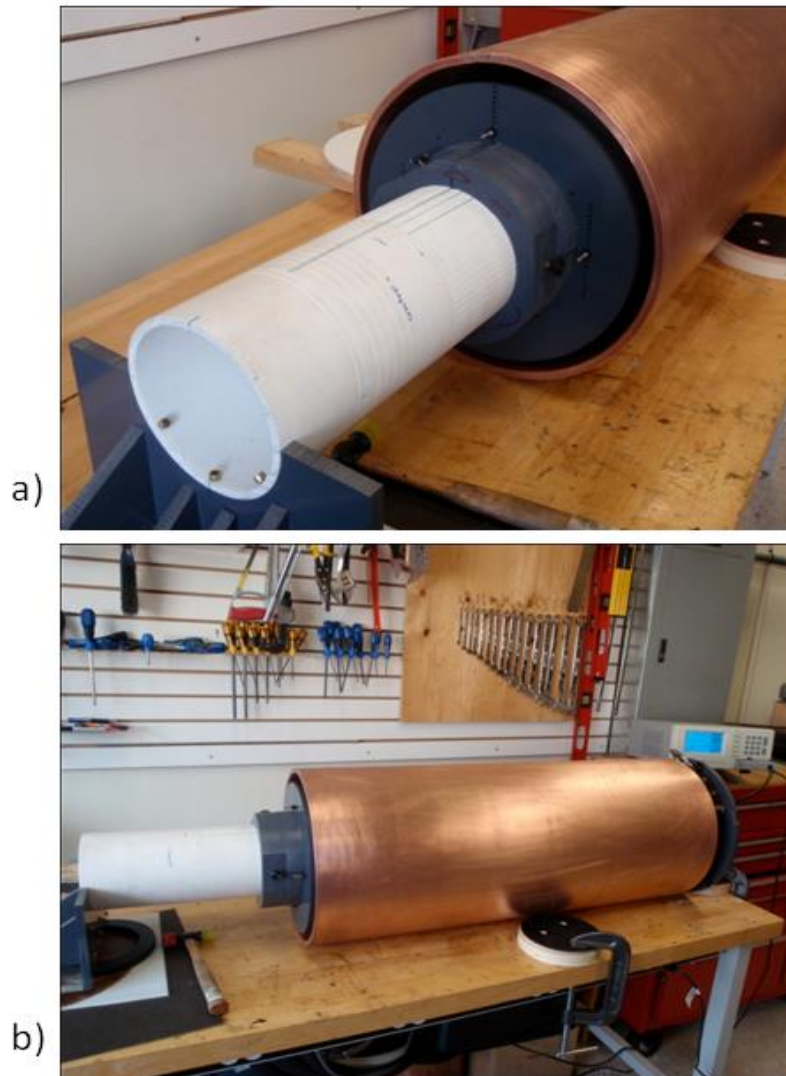




**Figure 2.6:** (a) depicts the seamless copper cylinder that was used to mimic the bore of the MR system, along with the measurement grid that was machined directly into the primary former. (b) shows the entire bench setup used to examine the inductive coupling.

## 2.2.4 Eddy current measurements

The experiment was conducted on a 36-cm-bore head-only 7.0-T Varian system. The  $y$ -gradient of the Siemens AC84 asymmetric head gradient set was used in conjunction with the insert gradient for the purpose of first-order shim correction.

The eddy current experiments were conducted inside the artificial bore, which was symmetrically positioned inside the scanner bore. The gradient insert coil was placed inside the artificial bore and held in place using a purpose-built bracket. At the patient-end of the scanner, the coil was supported by another custom bracket that attached to the patient bed. A positioning grid was milled into the PVC former of the gradient insert at the patient end to aid in measuring the location of the shields while inside the scanner.

The spatial and temporal frequency variations were measured as functions of shield misalignment in all three cylindrical directions (azimuthal, longitudinal, and radial) for both the  $x$ -gradient and  $z$ -gradient. A long gradient pulse of 3.0 s, with a 108.0  $\mu$ s rise time, was used to excite eddy currents followed by RF excitation for measurement. This sequence was repeated with varying RF time delays 50.0 ms apart starting at 0.25 ms and ending at 550.25 ms between the gradient pulse and excitation. Figure 2.7 depicts the pulse sequence.

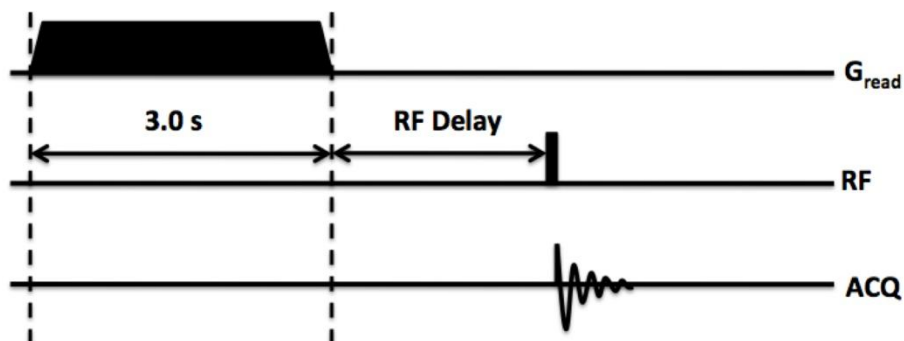


**Figure 2.7:** Illustration of the pulse sequence used for the generation and measurement of eddy currents.

A small solenoid RF coil was used to excite and measure the sample free induction decay (FID) at two positions (position 1 and position 2) 4.0-cm apart, along each gradient axis. The sample was comprised of a small 3.0-mm-diameter sphere, filled with a solution of distilled water and copper sulfate.  $B_0$  and linear eddy currents were determined from the two FIDs using the method described by *Gilbert et al.* (12).

### 2.2.5 Data analysis

Knowledge of the local magnetic field, derived from the FIDs at each sample position, along with the distance between the two positions allows for calculation of the  $B_0$  and linear eddy currents. This calculation assumes that only  $B_0$  and first order eddy currents are produced - higher-order eddy current determination would require more measurements along each axis.

The data collected at each position is the frequency as a function of time at each RF position, so determining the spatial variation of the eddy current at any point in time is just a matter of extracting the frequency for each sample position, calculating the magnetic field, and linearly interpolating between the two positions.

The frequency data were fit with a sum of decaying exponential terms using a Levenberg-Marquardt routine. The fitting function was determined by examining the reduced chi-squared as each additional decaying exponential term was added. A two-term decaying exponential resulted in the best fit for most of the data and also captured the hypothesized eddy current behavior quite well. For shield positions very close to being properly aligned, a single-term decaying exponential best captured the eddy current behavior, as the longest time constant term seemed to disappear. The error in the eddy current amplitude was estimated by examining the residuals of each fit, and taking the standard deviation over the last 100.0 ms of the residual. The first 5.0 ms was removed from each data set before fitting to eliminate the effect of current decaying in the gradient coils.

## 2.3 Results

### 2.3.1 Bench testing

As expected, the inductance of each gradient axis was minimized when the shield was perfectly aligned, and inductance changed significantly as the shields were displaced in each direction (figures 2.8(a-d)). The inductance and resistance values for both the transverse and longitudinal gradients, when the shield was properly aligned, can be found in table 2.1. Misalignment of the shield produced up to 30% increases in the inductance measurements compared with those taken at perfect alignment. When the measurements were repeated inside the artificial bore, it was found that the presence of the artificial bore reduced the total inductance of the system as the shield was displaced (figures 2.8 (e) and 2.8 (f)) indicating an inductive interaction between the gradient insert and the artificial bore.

**Table 2.1:** The performance data, both measured and modeled, for both shielded gradient axes.

	Modeled			Measured		
	L [ $\mu$ H]	R [ $\Omega$ ]	$\eta$ [mT/m/A]	L [ $\mu$ H]	R [m $\Omega$ ]	$\eta$ [mT/m/A]
x-unshielded	137	0.15	2.7	135.1 $\pm$ 0.7	75.0 $\pm$ 0.5	2.2 $\pm$ 0.1
z-unshielded	130	0.14	2.2	123.3 $\pm$ 0.7	130.0 $\pm$ 0.5	2.1 $\pm$ 0.1
x-shielded	118	0.21	2.3	116.9 $\pm$ 0.7	94.0 $\pm$ 0.5	1.9 $\pm$ 0.1
z-shielded	103	0.23	1.9	99.8 $\pm$ 0.7	220.0 $\pm$ 0.5	1.5 $\pm$ 0.1

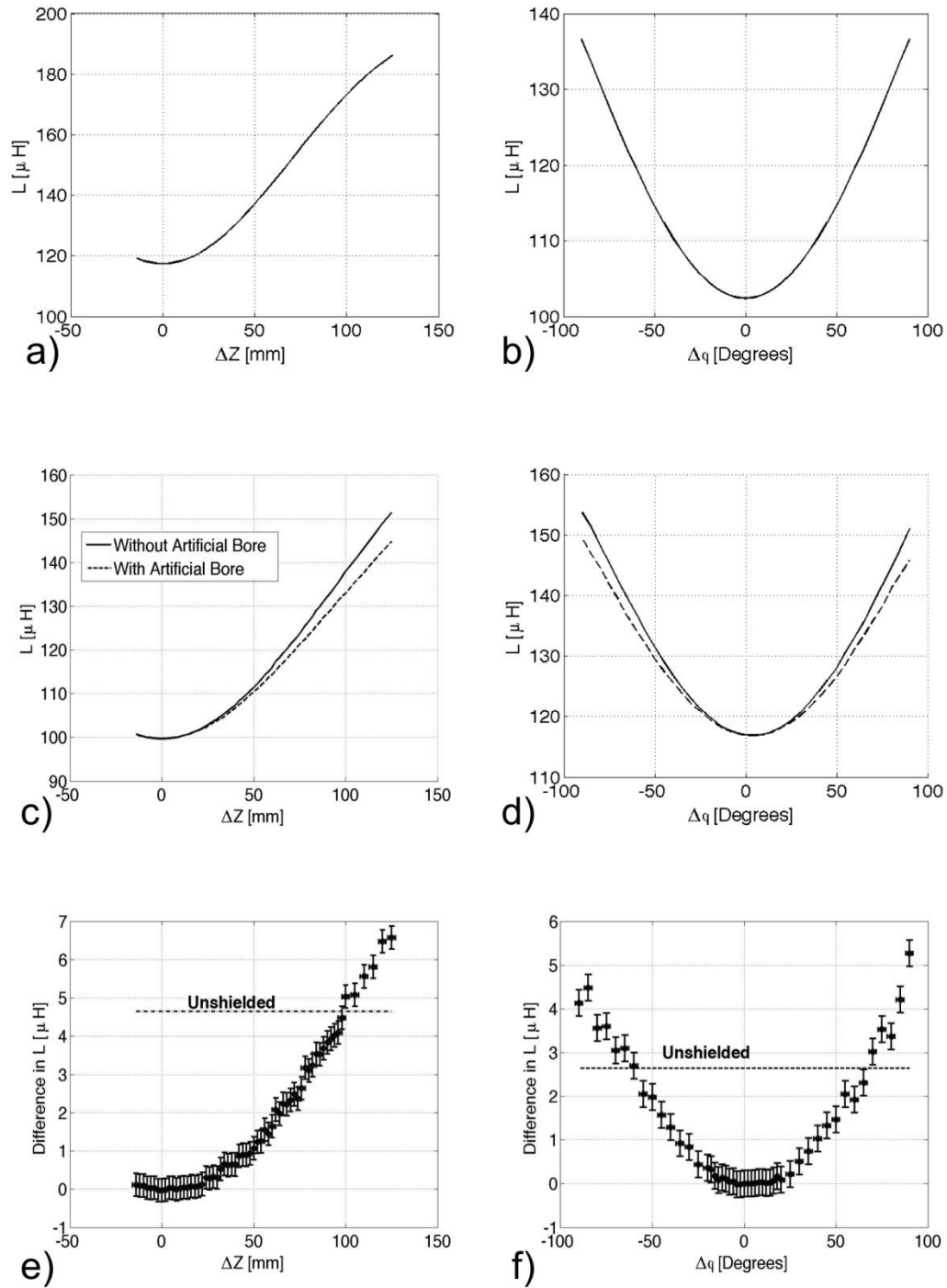


**Figure 2.8:** Part (a) is a plot of the simulated inductance values for the  $z$ -gradient as a function of shield position in the  $z$ -direction. Part (b) is a plot of the simulated inductance values for the  $x$ -gradient as a function of shield position in the  $\phi$ -direction. Part (c) shows the measured inductance values for the  $z$ -gradient as a function of shield position along the  $z$ -direction, with and without the artificial bore. Part (d) shows the

measured inductance values for the  $x$ -gradient as a function of shield position in the  $\phi$  direction, with and without the artificial bore. Parts (e) and (f) show the difference between the inductance values, with and without, the artificial bore for the  $z$ - and  $x$ -gradients respectively with reference to the inductance difference associated with completely removing each shield.

### 2.3.2 Eddy current measurements

Shown in figures 2.9 (a) and 2.9 (b) are examples of the frequency data obtained from analysis of FIDs for the  $z$ -gradient with various shield positions.

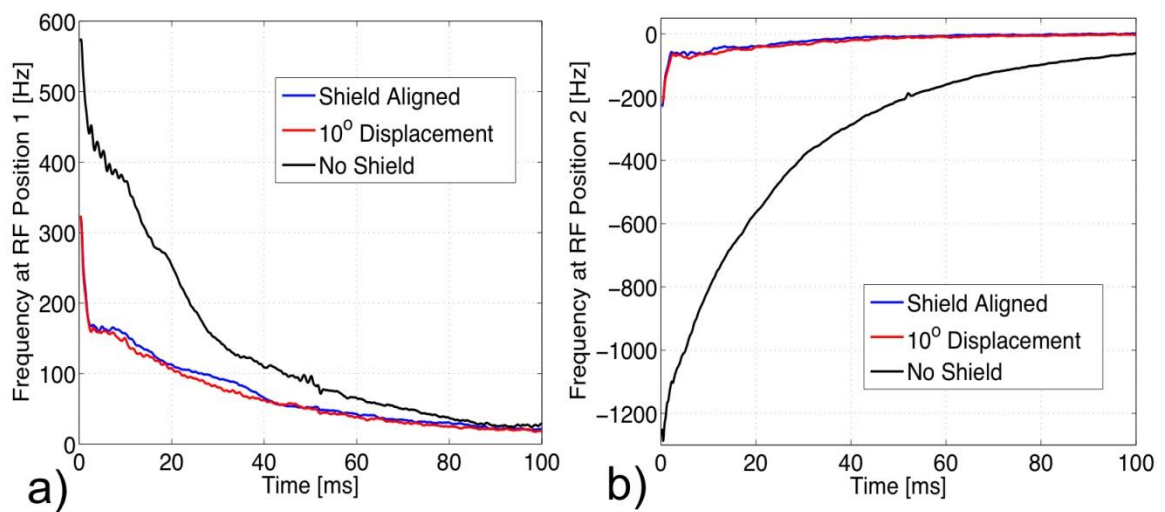


**Figure 2.9:** Shown here are the frequency measurements at two RF positions along the  $x$ -axis separated by 4.0 cm for four different primary-shield configurations for the  $x$ -gradient.

An example of the fit is shown in Figure 2.10 along with a corresponding residual plot. The time constants obtained for each decay term for three different primary-shield configurations are presented in Table 2.2 below.

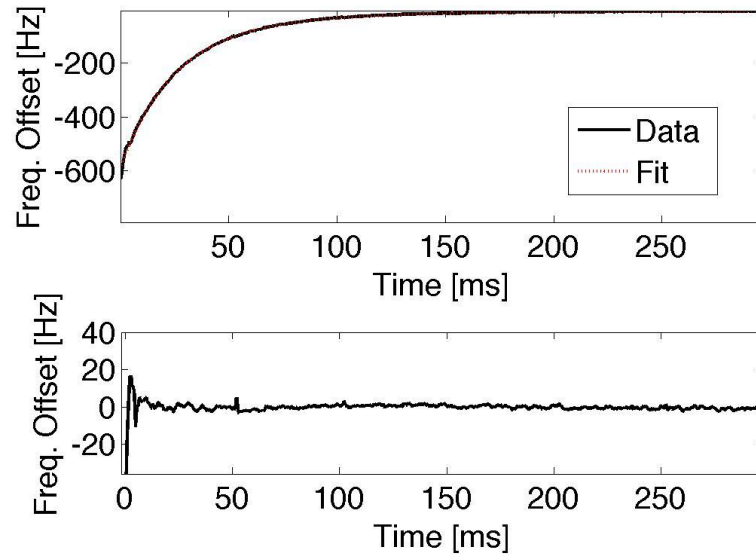


**Figure 2.10:** Shown above is an example of the frequency data gathered at a single RF position and the fitting function. Below is the residual for the fit, which highlights a decaying oscillation that was present across all the data sets.

**Table 2.2:** The time constants obtained from fitting the frequency data of three different primary-shield configurations.

	$\tau_1$ [ms]	$\tau_2$ [ms]
z-unshielded	$30.98 \pm 0.02$	$194 \pm 7$
x-unshielded	$27.07 \pm 0.04$	$75.9 \pm 0.5$
z-shielded	$29.05 \pm 0.04$	n/a
x-shielded	$30.69 \pm 0.05$	n/a
z ( $\Delta z=10\text{cm}$ )	$27.02 \pm 0.04$	$114 \pm 1$
x ( $\Delta \phi=10^\circ$ )	$29.5 \pm 0.4$	$96 \pm 8$

Figure 2.11 shows the interpolated field variation for various shield displacements for both gradient axes.

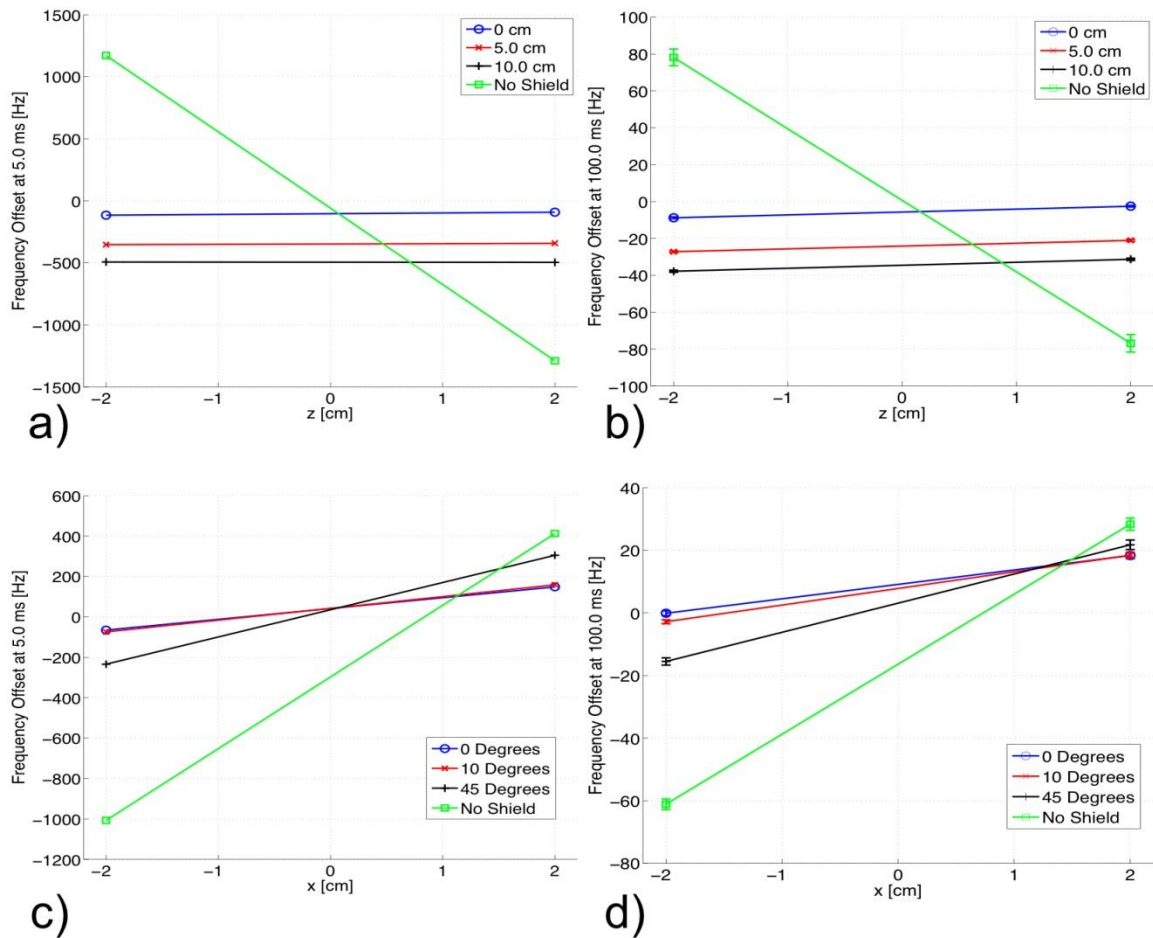


**Figure 2.11:** Plotted in (a) and (b) are the frequency offsets at each RF position along the  $z$ -axis for four different primary-shield configurations of the  $z$ -gradient at 5.0 ms (a), and 100.0 ms (b) after the gradient waveform. (c) and (d) show the same plots of the frequency offsets along the  $x$ -direction for four different primary-shield configurations for the  $x$ -gradient.

## 2.4 Discussion

Initial steps have been taken to explore the construction tolerances associated with shielding a gradient insert coil. The relationships between shield position relative to the primary coil and associated eddy current generation have been examined for both transverse and longitudinal gradient insert coil. These eddy current characteristics were examined by inductance measurements on the bench and by measuring frequency offsets inside an MR system.

The results of the bench testing give a good indication of the relationships between shield position and coupling. It was found that the inductance of each gradient axis was less when the artificial copper bore was present. This means that the bore acted as a shield itself, which indicates that eddy currents were generated on its surface. As the shield was displaced further from center, in each direction, the amount of coupling increased. Ultimately it was found that the  $z$ -axis shield could be misaligned up to 10 cm longitudinally before the inductive interaction with the bore was equal in magnitude to the unshielded gradient. For the  $x$ -axis, the angular misalignment could be as large as  $45^\circ$  before this happened. Positioning the primary and shielding coils relative to each other within these values is readily achievable.

Inside the MR system the shield displacements were even larger before the generated eddy currents were equal in size to the unshielded cases. This indicates that grossly misaligned shields still help to reduce overall field, and thus the inductive interaction with the surrounding MR system. As a practical example: a  $z$ -shield misaligned 5.0 mm longitudinally would result in a 130-Hz- $B_0$  eddy current and a  $G_z$  eddy current that is 0.05 % of the initial  $G_z$  impulse strength. An  $x$ -shield misaligned  $10^\circ$  azimuthally would result in 14-Hz- $B_0$  and 0.4-%- $G_x$  eddy currents. These values are very acceptable from an imaging standpoint, as pre-emphasis would easily be able to correct for eddy currents of these magnitudes. The dominant eddy current seen was dependent on the direction of shield displacement for each gradient axis. For the  $z$ -gradient, shield displacement along the  $z$ -direction resulted in a  $B_0$ -dominant eddy current. For the  $x$ -gradient shield displacement in the  $\phi$ -direction resulted in a  $B_0$ -dominant eddy current. However, shield displacement along  $z$  gave rise to a  $G_x$ -dominant eddy current.

There were two distinct eddy currents generated for most of the cases (after the removal of the first 5.0 ms of data). A large amplitude eddy current with a time constant of roughly 30 ms was always present, which was likely a result of the interaction with the artificial copper bore placed inside the scanner. Also a second long time constant, low-amplitude eddy current was present for geometries where the shield was not close to center. This suggests an interaction with structures of the MR system. This slow decaying term was not present when the shield was close to correct alignment, which



makes physical sense because the insert coil was a large distance from the actual bore of the MR system; thus the shield would have made the interaction extremely small.

One of the major challenges associated with this experimental setup is that the inductance of each gradient axis changes as a function of shield position. This poses a problem since the amplifiers were matched to the original inductance of each gradient axis- *i.e.* the inductance when the shields were aligned. As the shields were misaligned the inductance changed and the load became unmatched with the amplifier settings. It would have been very time consuming to continually impedance match every time the shield was moved, and thus it was not done. The oscillation that was present in all the data sets was likely a result of this impedance mismatch since the amplitude of the oscillation scaled with the size of the mismatch.

## 2.5 References

1. Koch KM, McIntyre S, Nixon TW, Rothman DL, De Graaf RA. 2006 Dynamic shim updating on the human brain. *Journal of Magnetic Resonance*;180(2):286-296.
2. van Gelderen P, de Zwart JA, Starewicz P, Hinks RS, Duyn JH. 2007 Real-time shimming to compensate for respiration-induced B-0 fluctuations. *Magnetic Resonance in Medicine*;57(2):362-368.
3. Balteau E, Hutton C, Weiskopf N. 2010 Improved shimming for fMRI specially optimizing the local BOLD sensitivity. *NeuroImage*;49:327-336.
4. Henkelman RM, Bronskill MJ. 1987 Artifacts in Magnetic-Resonance-Imaging. *Medical Physics*;14(3):506-507.
5. Hughes DG, Robertson S, Allen PS. 1992 Intensity Artifacts in Mri Caused by Gradient Switching in an Animal-Size Nmr Magnet. *Magnetic Resonance in Medicine*;25(1):167-179.
6. Mansfield P, Chapman B. 1986 Active Magnetic Screening of Gradient Coils in Nmr Imaging. *Journal of Magnetic Resonance*;66(3):573-576.
7. Vanvaals JJ, Bergman AH. 1990 Optimization of Eddy-Current Compensation. *Journal of Magnetic Resonance*;90(1):52-70.
8. Jehenson P, Westphal M, Schuff N. 1990 Analytical Method for the Compensation of Eddy-Current Effects Induced by Pulsed Magnetic-Field Gradients in Nmr Systems. *Journal of Magnetic Resonance*;90(2):264-278.
9. Boesch C, Gruetter R, Martin E. 1991 Temporal and Spatial-Analysis of Fields Generated by Eddy Currents in Superconducting Magnets - Optimization of Corrections and Quantitative Characterization of Magnet Gradient Systems. *Magnetic Resonance in Medicine*;20(2):268-284.
10. Liu Q, Hughes DG, Allen PS. 1994 Quantitative Characterization of the Eddy-Current Fields in a 40-Cm Bore Superconducting Magnet. *Magnetic Resonance in Medicine*;31(1):73-76.
11. Chronik BA, Alejski A, Rutt BK. 2000 Design and fabrication of a three-axis edge ROU head and neck gradient coil. *Magnetic Resonance in Medicine*;44(6):955-963.
12. Gilbert KM, Gati JS, Klassen LM, Menon RS. 2010 A cradle-shaped gradient coil to expand the clear-bore width of an animal MRI scanner. *Physics in Medicine and Biology*;55(2):497-514.

13. Liu Q, Hughes DG, Allen PS. 1995 Constructional Tolerances of Shielded Gradient-Coil Sets in Relation to Artifacts in Mri and Errors in in-Vivo Mrs. *Journal of Magnetic Resonance Series B*;108(3):205-212.
14. Carlson JW, Derby KA, Hawryszko KC, Weideman M. 1992 Design and Evaluation of Shielded Gradient Coils. *Magnetic Resonance in Medicine*;26(2):191-206.
15. Turner R, Bowley RM. 1986 Passive Screening of Switched Magnetic-Field Gradients. *Journal of Physics E-Scientific Instruments*;19(10):876-879.
16. Romeo F, Hoult DI. 1984 Magnet Field Profiling - Analysis and Correcting Coil Design. *Magnetic Resonance in Medicine*;1(1):44-65.
17. Turner R. 1988 Minimum Inductance Coils. *Journal of Physics E-Scientific Instruments*;21(10):948-952.
18. Crozier S, Doddrell DM. 1993 Gradient-Coil Design by Simulated Annealing. *Journal of Magnetic Resonance Series A*;103(3):354-357.
19. Lemdiasov RA, Ludwig R. 2005 A stream function method for gradient coil design. *Concepts in Magnetic Resonance Part B-Magnetic Resonance Engineering*;26B(1):67-80.
20. Edelstein W, Schenck J; A stream function method for coil construction. U.S. 1987.

## Chapter 3

### 3 A direct minimum energy method for designing shielding coils of arbitrary geometry

#### 3.1 Introduction

Almost all applications in magnetic resonance require rapid switching of magnetic gradient fields within the scanner, and many emerging applications take advantage of rapidly switched magnetic shim coils. Eddy currents are generated in the conducting structures of the system by the use of these magnets, resulting in time varying and spatially varying magnetic fields that must be either minimized or corrected for. This problem is further complicated when non-cylindrical or asymmetrical insert electromagnets are used for specialized applications (1,2,3). Asymmetric coils generate more complex eddy currents, which generally produce non-linear magnetic fields within the system. Beyond effects on image quality, currents (and therefore power deposition) induced in the cold structures of the MR system cause increased helium boil-off. Rapidly switched electromagnets (particularly even-order zonal shim coils and similar devices) coupling with the superconducting coils of the main magnet may result in decreased system stability and, in the most extreme cases, quenching of the superconducting system.

Interruption of the coupling between an insert coil (gradient or otherwise) and the MR system is typically accomplished using active magnetic shielding (4). Active shielding is a technique that makes use of a second coil, typically driven in series with the primary coil, to cancel the field effects of the primary coil over a desired region. The standard shielded gradient coil is cylindrical with the shielding coil at a larger radius than the primary coil, such that the net inductive coupling with the rest of the MR system is greatly reduced. The use of non-cylindrical and asymmetric gradients has made the design of active shielding systems both more challenging and yet more important.

Many methods for designing shielding coils have been used in the past. These methods can be divided into two broad categories: analytic methods (5,6) and purely

numerical methods (7,8,9). The common theme in all methods is to make use of a magnetic field shielding condition, which constrains the magnetic field of the primary plus shield to be zero (or near zero) over some specified region. Most commonly this is the region radially outside the shielding coil diameter. This constraint is usually expressed as a boundary condition at the shield surface in analytic methods, and as a discrete set of field constraints in numerical methods.

Analytic methods solve for the continuous current density on the shielding surface required to cancel the field over the chosen region. Analytic solutions generally require the existence of a separable solution to Greens function for the geometry in question, or that the symmetry can be exploited in some way. Because of this, deriving an analytic solution for the shielding current density can generally only be accomplished in geometrically simple systems. The most common example is that of the cylindrical shielded gradient coil, for which an analytic solution for the shielding current density as a function of the primary current density exists (5). Exact shielding solutions have also been found for planes (10,11,12), ellipses (13), hyperbolic surfaces (14), spheres (15), and other simple geometries (16).

As they are not limited in geometry, numerical methods are much more flexible in terms of finding shielding solutions. For example, one could specify that a shield eliminate field in a particular region while minimally affecting another. Despite the additional freedom associated with numerical techniques, arriving at acceptable optimal shielding current densities is challenging. Depending on the sophistication and method of parameterization, computational power, computing time, and even convergence can be problems.

In this paper, a numerical method is presented which can be applied to shielding coils of any geometry and yet does not require use of the explicit shielding field constraints mentioned above. This method is based upon a simple assumption: that the shielding current density on a conductor of arbitrary geometry is simply that which minimizes the total magnetic energy for the combined primary-shield system. Consider a simple system consisting of a wire-wound coil (the primary) and a conducting surface of

any geometry positioned nearby. If the primary coil is driven with a time-varying current, an induced current will appear on the conductor that minimizes the change in flux created by the primary. If the assumption is made that the eddy current produced is that which minimizes the total magnetic energy in the system, then the connection to active shielding is made when one assumes that the induced (eddy) current density is actually the correct shielding current density for that specific geometry. It is important to note that this approach is based on the global minimization of magnetic energy in the system; therefore, the shield current density obtained is that which represents the optimal shield for all space. It would not necessarily result in a shield optimized for field cancellation over any particular region. In the following sections, the method is derived and cast in a form suitable for implementation using the Boundary Element Method (BEM) (17,18,2). In order to test the assumptions noted above, the equivalence of this method to analytic methods is then derived for the case of cylindrical shielding. Results obtained using this new method are shown for both cylindrical and planar coil geometries. Finally, a complex (though impractical) case of shielding a cylinder with a rectangular box-shaped shield coil is introduced to demonstrate the versatility of the approach in a geometry which would be exceedingly complicated to address using other methods.

## 3.2 Methods

Based on the assumption that obtaining the shield current density for a system consisting of a known primary coil and shielding surface is equivalent to the problem of minimizing the total magnetic energy of the system, the solution is obtained as follows. The energy stored in two conductors (19) is given by:

$$W = \frac{1}{2} \int \mathbf{J} \cdot \mathbf{A} dV, \quad (3.1)$$

where  $\mathbf{J}$  is the current density of both conductors, and  $\mathbf{A}$  is the vector potential resulting from the combined conductors. Equation (3.1) can be re-written (19) as:

$$W = \frac{\mu_0}{8\pi} \int dV \int dV' \frac{\mathbf{J}(\mathbf{r}) \cdot \mathbf{J}(\mathbf{r}')}{|\mathbf{r} - \mathbf{r}'|}. \quad (3.2)$$

$\mathbf{r}$  and  $\mathbf{r}'$  are the position vectors for each current density.

An arbitrary surface geometry for the shield is first selected and discretized into a finite element mesh of triangles, the vertices of which will be referred to as nodes. Next, using the same formalism as Lemdiasov and Ludwig (18), a stream function is defined,  $\psi(\mathbf{r})$ , over the surface of the mesh. The surface current density,  $\mathbf{J}(\mathbf{r})$ , is then represented by:

$$\mathbf{J}(\mathbf{r}) = \nabla \times [\psi(\mathbf{r})\mathbf{n}(\mathbf{r})], \quad (3.3)$$

where  $\mathbf{n}(\mathbf{r})$  is a vector of unit length perpendicular to the surface. The stream function,  $\psi(\mathbf{r})$ , can be approximated by a weighted sum of basis functions:

$$\psi(\mathbf{r}) \approx \sum_{n=1}^N i_n \psi_n(\mathbf{r}), \quad (3.4)$$

where the coefficients  $i_n$  are unknown and  $N$  is the total number of nodes in the surface. The result of this approach is the following approximation for the surface current density:

$$\mathbf{J}(\mathbf{r}) \approx \sum_{n=1}^N i_n \nabla \times [\psi_n(\mathbf{r})\mathbf{n}(\mathbf{r})] = \sum_{n=1}^N i_n \mathbf{f}_n(\mathbf{r}), \quad (3.5)$$

where  $\mathbf{f}_n(\mathbf{r})$ , are basis functions defined that describe the current circulating around each node. These are the very same current density basis functions described by Lemdiasov and Ludwig (18). The total current density for the primary-shield system can be decomposed into its individual components:

$$\mathbf{J}(\mathbf{r}) = \mathbf{J}_p(\mathbf{r}) + \mathbf{J}_s(\mathbf{r}), \quad (3.6)$$

where  $\mathbf{J}_p(\mathbf{r})$  and  $\mathbf{J}_s(\mathbf{r})$  represent the primary and shielding current densities respectively. Using (3.5) the primary and shield current densities can be expressed as:

$$\mathbf{J}_p(\mathbf{r}) \approx \sum_{n=1}^N i_p^n \mathbf{f}_p^n(\mathbf{r}) \quad (3.7)$$

$$\mathbf{J}_s(\mathbf{r}) \approx \sum_{m=1}^M i_s^m \mathbf{f}_s^m(\mathbf{r}). \quad (3.8)$$

Combining (3.2), (3.6), (3.7), and (3.8) yields:

$$\begin{aligned} W = & \frac{\mu_0}{8\pi} \sum_{n=1}^N \sum_{n'=1}^N i_p^n i_p^{n'} \int dS_p \int dS_p' \frac{\mathbf{f}_p^n(\mathbf{r}) \cdot \mathbf{f}_p^{n'}(\mathbf{r}')}{|\mathbf{r} - \mathbf{r}'|} \dots \\ & + \frac{\mu_0}{8\pi} \sum_{m=1}^M \sum_{m'=1}^M i_s^m i_s^{m'} \int dS_s \int dS_s' \frac{\mathbf{f}_s^m(\mathbf{r}) \cdot \mathbf{f}_s^{m'}(\mathbf{r}')}{|\mathbf{r} - \mathbf{r}'|} + \frac{\mu_0}{4\pi} \sum_{n=1}^N \sum_{m=1}^M i_p^n i_s^m \int dS_p \int dS_s' \frac{\mathbf{f}_p^n(\mathbf{r}) \cdot \mathbf{f}_s^m(\mathbf{r}')}{|\mathbf{r} - \mathbf{r}'|}. \end{aligned} \quad (3.9)$$

For this problem it is assumed that the primary current density is known (i.e. the set of  $i_p$  values are known), and the shielding current density (i.e. the set of  $i_s$  values) is to be solved for. To find the shield current density that minimizes the magnetic energy of the entire system, the derivative of (3.9) is taken with respect to the shielding current density coefficients  $i_s^m$  and equated to zero. The expression that results is:

$$\frac{\mu_0}{8\pi} \sum_{m'=1}^M i_s^{m'} \int dS_s \int dS_s' \frac{\mathbf{f}_s^{m'}(\mathbf{r}) \cdot \mathbf{f}_s^{m'}(\mathbf{r}')}{|\mathbf{r} - \mathbf{r}'|} = -\frac{\mu_0}{4\pi} \sum_{n=1}^N i_p^n \int dS_p \int dS_s' \frac{\mathbf{f}_p^n(\mathbf{r}) \cdot \mathbf{f}_s^m(\mathbf{r}')}{|\mathbf{r} - \mathbf{r}'|}. \quad (3.10)$$

With this representation, (3.10) simplifies to:

$$L_s^{mm'} i_s^{m'} = -M_{ps}^{mn} i_p^n, \quad (3.11)$$

where:

$$L_s^{mm'} = L_s^{m'm} = \frac{\mu_0}{8\pi} \int dS_s \int dS_s' \frac{\mathbf{f}_s^m(\mathbf{r}) \cdot \mathbf{f}_s^{m'}(\mathbf{r}')}{|\mathbf{r} - \mathbf{r}'|}, \quad (3.12)$$

$$M_{ps}^{mn} = \frac{\mu_0}{4\pi} \int dS_p \int dS_s' \frac{\mathbf{f}_p^n(\mathbf{r}) \cdot \mathbf{f}_s^m(\mathbf{r}')}{|\mathbf{r} - \mathbf{r}'|}. \quad (3.13)$$



The matrices  $L_s^{mm'}$  and  $M_{ps}^{mn}$  represent the self-inductance of the shield and the mutual inductance between the shield and primary surfaces respectively. The current density weighting coefficients for the shield surface are then formally obtained by:

$$i_s^{m'} = -[L_s^{mm'}]^{-1} M_{ps}^{mn} i_p^n. \quad (3.14)$$

To review, the algorithm proceeds as follows. A primary-coil current density is assumed known, and is expressed by the set of current density coefficients  $i_p$  and a defined set of finite-element basis functions  $\mathbf{f}_p$ . A desired shield surface is then defined as a finite element mesh, which specifies the set of basis functions  $\mathbf{f}_s$ . From the primary and shield geometries thus defined, the mutual and self-inductance matrices can be calculated. Finally, (3.14) is applied formally to obtain the required set of shield current density amplitudes  $i_s$ , and the shield current density is obtained via (3.7) and (3.8).

The mesh geometries of the primary and shielding surfaces were created in COMSOL Multiphysics<sup>®</sup> version 3.5a and then imported into MATLAB<sup>®</sup> version 7.11.0. The BE method was coded in an object-oriented class-based structure in MATLAB<sup>®</sup> with the current basis functions, resistance, and field matrices calculations written in ANSI C. The calculation of the self-inductances and mutual inductances were also done in ANSI C, while the final matrix inversion (i.e. solution to (3.14)), was performed in MATLAB<sup>®</sup>. All computations were done on a 2.66 GHz iMac with 4 GB of RAM.

As a way of testing the validity of this method, it was compared against the well-known situation of an infinitely long cylindrical primary coil of radius  $R_p$  and an infinitely long cylindrical shielding coil of radius  $R_s$  (5). Two standard, unshielded gradient coils (one  $x$ -gradient and one  $z$ -gradient) were designed using the BE method with a primary geometry containing 2298 node points and having an inner diameter of 40 cm and a maximum length of 80 cm in order to mimic basic insert gradient coil technology. The wire patterns, which are obtained by contouring the stream functions calculated from the current densities, are shown in figures 3.4 (a) and 3.4 (c). The discretization of the wire pattern is determined by the mesh size. The performance values for these coils can be found in table 3.1. Shields were then designed for each primary

coil using both the method of Turner and Bowley (5), which calculates the current density analytically, as well as the minimum energy method presented here. Both methods require only the primary current density and the shield geometry as inputs. The shield geometry was specified as a 60 cm inner diameter cylinder with an allowed length of 1.6 m, and 4092 node points. The shields obtained with the respective methods were compared several different ways: resultant field magnitude as a function of  $z$  outside the coil; coil efficiency and total inductance with and without the shields; and gradient uniformity within the imaging regions of the coils with and without the shields.

In the second part of this study, the minimum energy method was implemented over a planar geometry. Planar gradients are more difficult from a shielding perspective than cylindrical systems, yet the solutions are well documented (10). A planar  $y$ -gradient coil was first simulated using the BE method over a plane extending 20 cm ( $\pm 10$  cm) in the  $x$ -direction and 30 cm ( $\pm 15$  cm) in the  $z$ -direction. A large shielding surface with 1503 node points was then created extending 50 cm ( $\pm 25$  cm) in both the  $x$ - and  $z$ -directions and positioned 3 cm below the planar gradient coil (primary at 0 cm and shield at -3.0 cm). The shield current density was calculated using the methods described, and the effectiveness of the shield over the region beyond the shielding surface was evaluated.

Finally, shields for normal cylindrical  $x$ - and  $z$ -gradient coils were created over closed “rectangular-box” geometries. This geometry is not intended to represent a particularly practical situation, but rather to provide an example case for which an analytic solution would be exceedingly difficult to achieve. The box shields were designed for the same cylindrical primary gradient coils described above. The rectangular boxes were designed with dimensions of: 60 cm ( $x$ - and  $y$ -axes), 90 cm ( $z$ -axis) in order to allow the boxes to fully encapsulate the  $x$  and  $z$ -gradient coils. The rectangular geometry had 5304 node points. The effectiveness of the shields was then evaluated.

## 3.3 Results

### 3.3.1 Cylindrical gradient

Figure 3.1 (a) shows the current density profile for the  $z$ -gradient shield designed with the analytic method (5). The current density for the  $z$ -gradient shield using the minimum energy method is virtually identical; the percent difference between the two current densities is shown as a function of  $z$  in figure 3.1 (b).

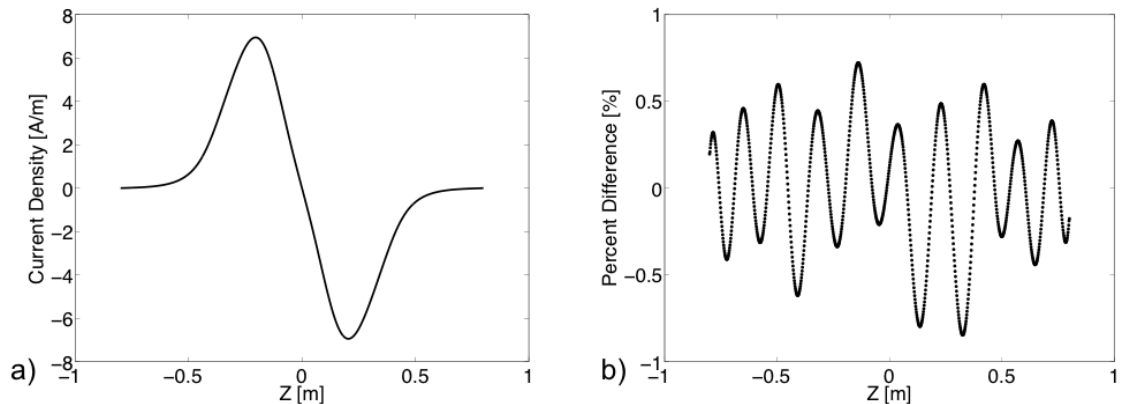


**Figure 3.1:** The current density profile along the  $z$ -axis for the  $z$ -gradient shield designed using the analytic method (a) and the percent difference between the current densities of the analytic shield and BEM shield (b).

The current densities for the  $x$ -gradient shields obtained using the analytic and minimum-energy methods agreed equally well, as shown in figure 3.2. The small discrepancies between the two methods (less than 1% in all cases) are attributed to minor sampling differences between the two algorithms. The inductance and efficiency of the  $x$ - and  $z$ -gradients with and without shields are shown in table 3.1. The efficiency was calculated over a sphere of points with diameter 20.0 cm, representing the imaging region of the coils.

**Table 3.1:** Efficiency and inductance values for the cylindrical gradient set.

	$\eta$ [mT m <sup>-1</sup> A <sup>-1</sup> ]	L [μH]
$x$ -unshielded	0.388	254
$x$ -shielded (Turner method)	0.333	208
$x$ -shielded (Min. energy)	0.333	208
$z$ -unshielded	0.431	494
$z$ -shielded (Turner method)	0.334	368
$z$ -shielded (Min. energy)	0.334	368

The magnitude of the magnetic field calculated as a function of  $z$ , at a radius of 40.0 cm, for the  $z$ - (figure 3.2 (a)) and  $x$ -gradients (figure 3.2 (c)) are shown below. The differences in field (log-scale) between the two shielding methods are shown in figures 3.2 (b) and 3.2 (d). It can be seen that the maximum absolute difference is less than 0.08  $\mu\text{T}$ .

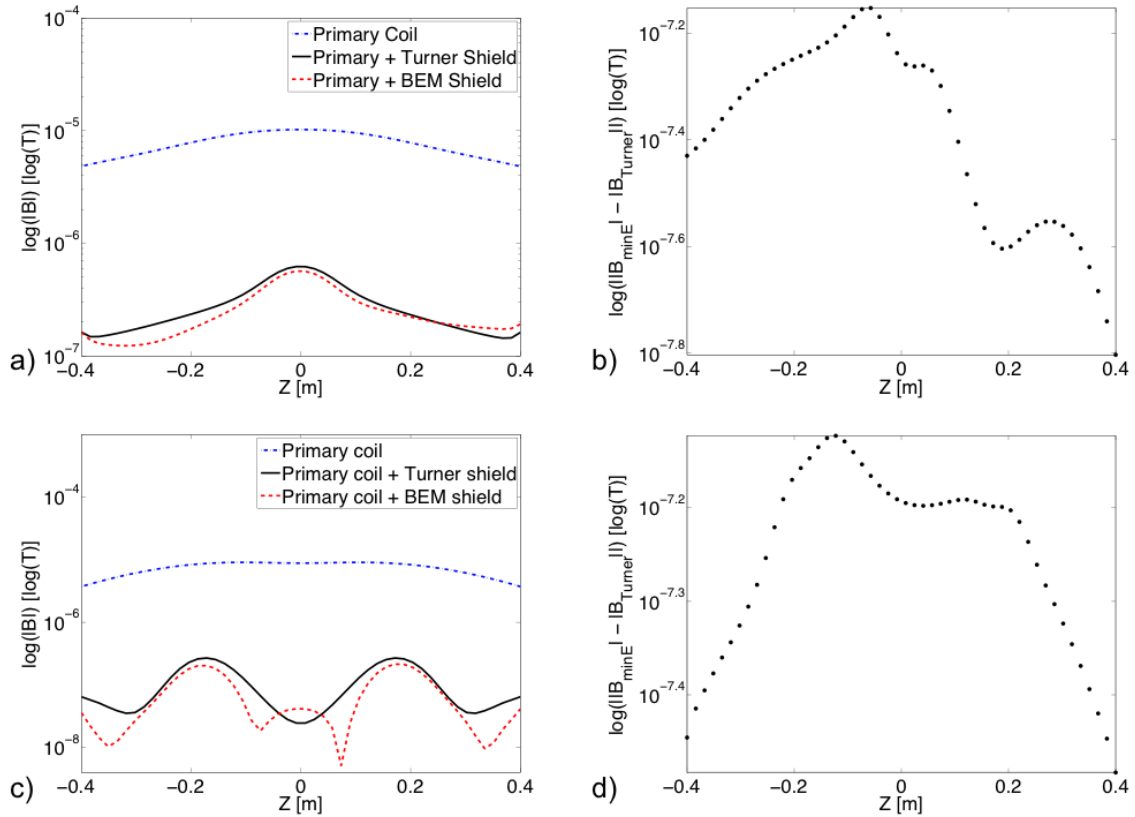


**Figure 3.2:** The magnetic field profiles for the  $z$ -gradient, unshielded and shielded with both the analytic and BEM shields (a), and the difference in magnetic fields for the analytic shield and the BEM shield (b). Figures (c) and (d) show the field differences for the  $x$ -gradient.

### 3.3.2 Planar gradient

The planar gradient was designed with an efficiency of  $1.00 \text{ mTm}^{-1}\text{A}^{-1}$  and an inductance of  $2.07 \mu\text{H}$  without the shield. With the shield the efficiency dropped to  $0.815 \text{ mTm}^{-1}\text{A}^{-1}$  and the inductance was  $1.49 \mu\text{H}$ . The efficiencies were calculated over a  $10.0 \text{ cm}$  cubic volume centered  $6.0 \text{ cm}$  above the primary coil. The wire pattern for the shielded planar gradient is shown in figure 3.3 (a). The magnetic field was calculated along the  $y$ -axis

(i.e. as a function of distance away from the primary coil, along the line perpendicular to the plane of the coil) for the shielded and unshielded cases and is shown in figure 3.3 (b).

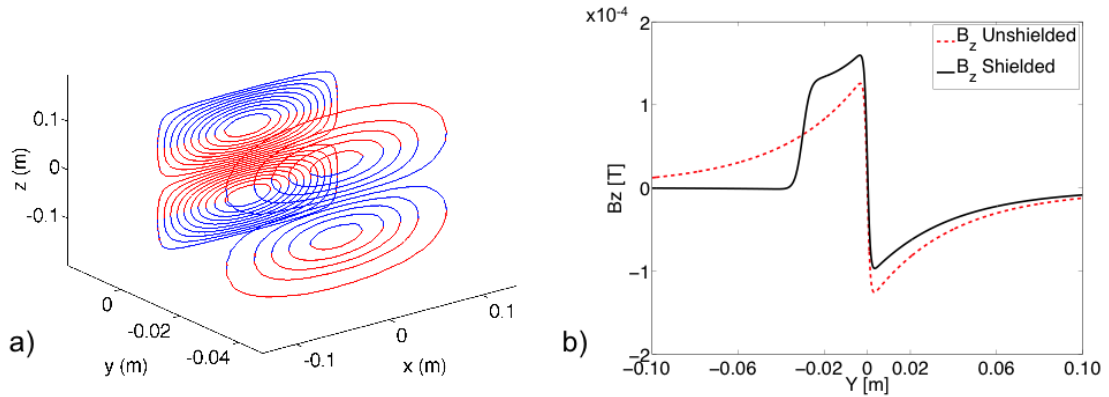


**Figure 3.3:** The wire pattern for the planar  $y$ -gradient coil (a) and the magnetic field profile, along the  $y$ -axis, for the planar gradient with and without the BEM shield (b). The primary is located at the origin and the shield is located at  $y = -3.0$  cm.

### 3.3.3 Cylindrical gradient with rectangular shield

The efficiency and inductances values for the  $x$ - and  $z$ - gradients are given in table 3.2 along with the corresponding values with the box shield.

**Table 3.2:** Efficiency and inductance values for the cylindrical gradient with rectangular shield.

	$\eta$ [mT m <sup>-1</sup> A <sup>-1</sup> ]	$L$ [ $\mu$ H]
x-unshielded	0.388	254
x-shielded	0.352	224
z-unshielded	0.431	494
z-shielded	0.370	407

The wire patterns for the cylindrical  $z$ -gradient (primary) and corresponding rectangular shield are shown in figures 3.4 (a) and 3.4 (b) respectively. Figures 3.4 (c) and 3.4 (d) show the patterns for the  $x$ -axis (primary and shield). Note that connection leads are not included in these figures.

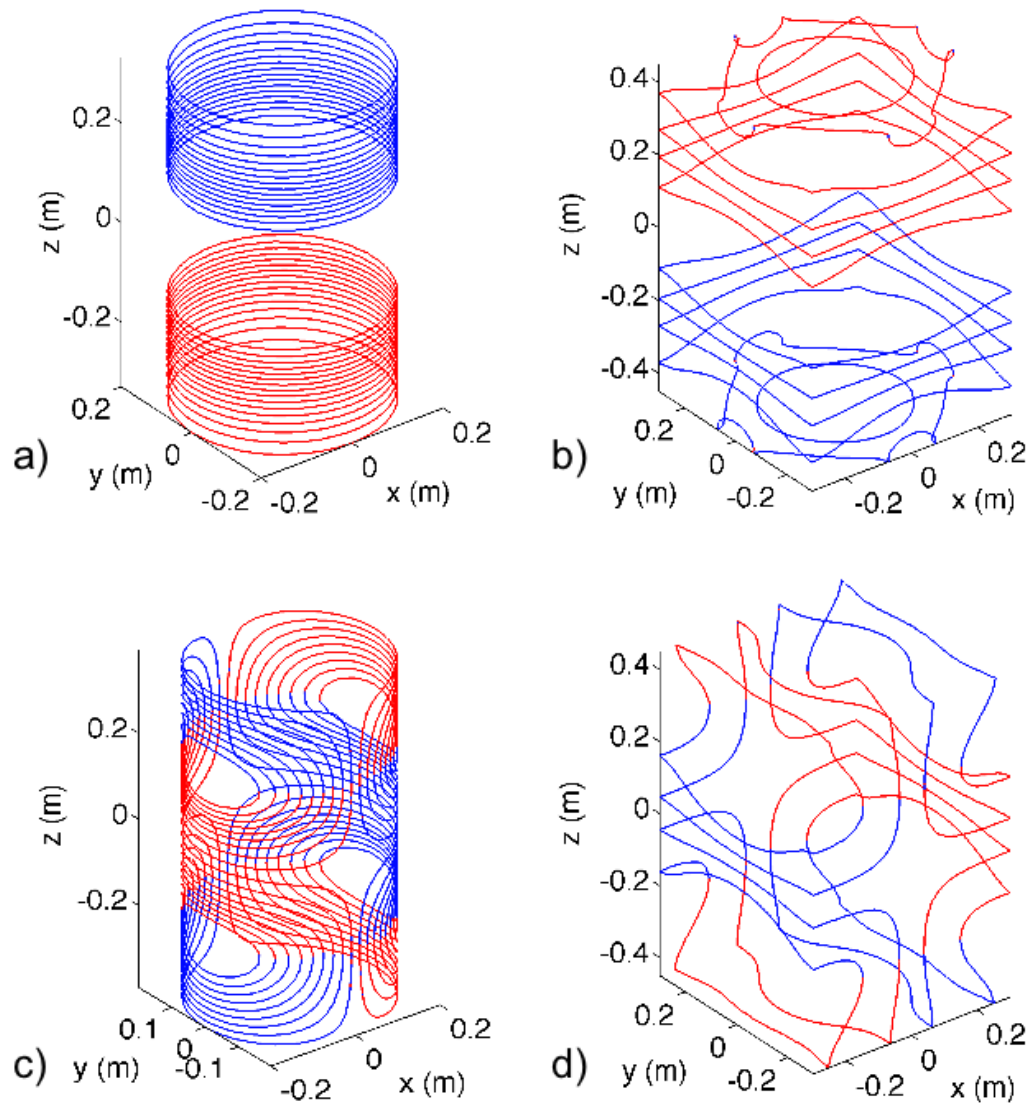


**Figure 3.4:** The wire patterns for the cylindrical  $z$ -gradient (a) and the rectangular ‘box-shaped’ shield (b), as well as the  $x$ -gradient (c) and its rectangular shield (d).

Contour plots of the field magnitude calculated over the  $xy$ -plane (through the longitudinal centre of the coils) are shown for the shielded coils in figure 3.5.

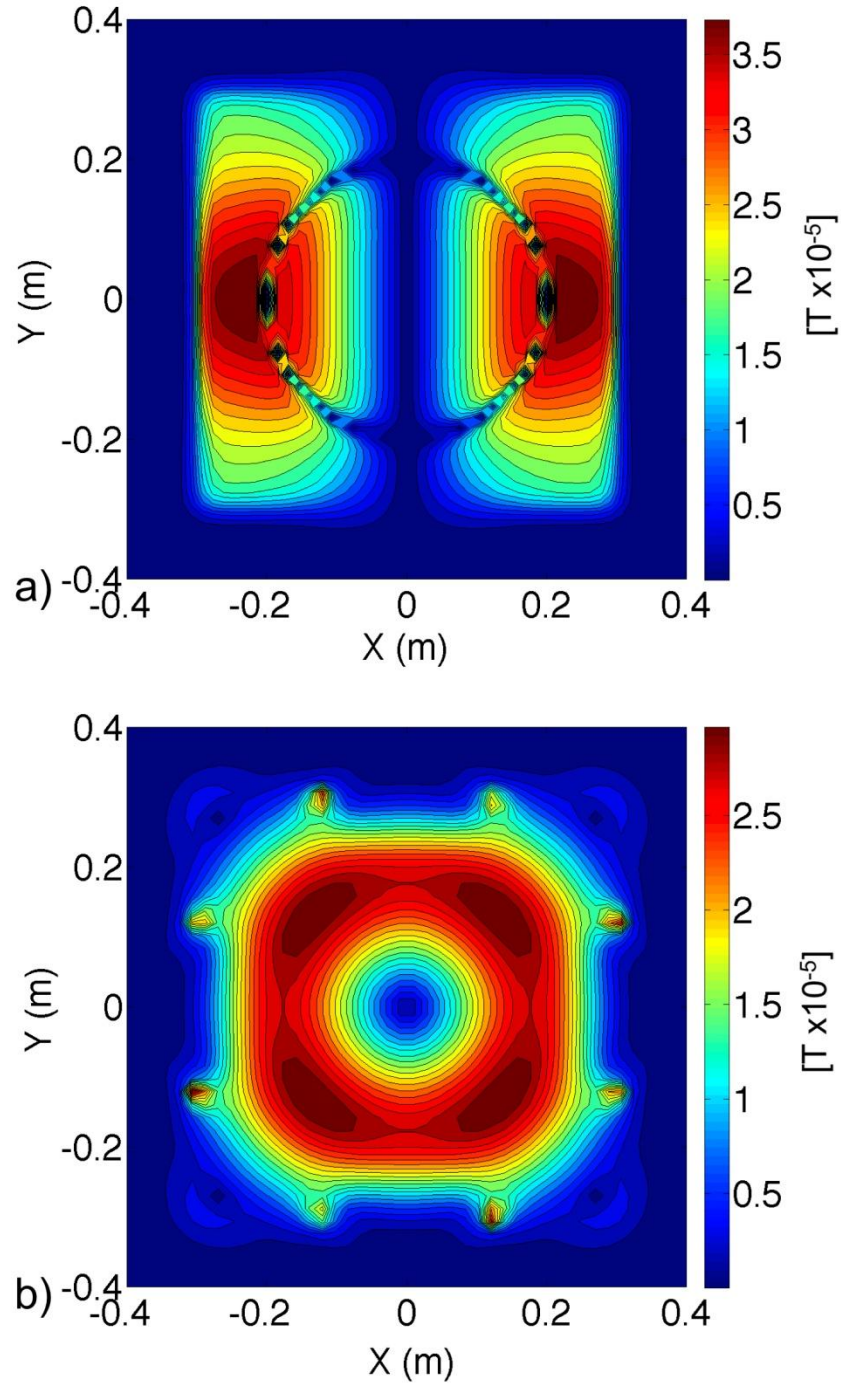


**Figure 3.5:** The magnetic field profiles across the  $xy$ -plane for the  $z$ -gradient (a) and  $x$ -gradient (b), with their corresponding rectangular shields.

### 3.4 Discussion

It has been shown that the shielding current density on a surface of arbitrary geometry can be obtained by minimizing the magnetic energy of the entire system. This method

was validated against well-known analytic shielding solutions for the infinite cylinder case. The small differences observed between the methods are attributed to small differences in stream function contouring, which occurred because the stream functions for the analytic shields were exact whereas the shields for the minimum energy method were calculated for a discretely sampled surface. As the mesh density is increased for the minimum-energy method, the differences decrease.

Most other analytic or numerical techniques for optimized gradient coil design include a minimization of energy (either magnetic energy, thermal energy, or a combination of the two) either implicitly or explicitly. What is unique about the method presented here is the idea of relying on the magnetic energy minimization alone in order to obtain a shielding current density.

The benefits of this method are two-fold. First, the shield geometry can take any specified form. For simple shield geometries such as cylinders and planes, analytic expressions for shield current densities are known and there is no pressing need for a numerical method. However, in situations where there is a need for asymmetric or irregular shaped gradient or shim sets, the minimum-energy shield method introduced here can be very useful. Secondly, this method does not require any target field points. This is significant because a shield's effectiveness is limited by the users ability to correctly specify field targets (i.e. number and location of target points).

Though fundamentally numerical, this method is not an iterative optimization scheme. Given a primary coil density and the desired shield geometry, the shielding current density is calculated directly. The method is relatively fast and simple to use. All the solutions in this paper were obtained in under 60 seconds.

Several limitations of this method exist. The first of which is that the primary and shielding coil are not designed simultaneously. Knowledge of the primary coil must exist prior to calculating the shielding coil. Other analytic methods (20) though limited to simple geometries, have shown a benefit to designing the entire primary-shield system together. One general application in which it would be necessary to design a shield for an already existing gradient coil would be that of shielding a specific region within the



scanner from interference with the rapidly switching gradient coils. A specific example would be shielding an interventional device (possibly a needle biopsy system) from the gradient fields. The device may be relatively distal from the imaging region, but still need to be protected from the gradient fields. Such a shield (which might be constructed to fully or partially surround the device) would be driven in series with the gradient system. Although surely an exotic example, this does represent an example of the desire to design a shield separately from an existing gradient coil.

A second limitation is that the shielding current density, which minimizes the total magnetic energy of the primary-shield system, is global in nature. That is to say, it is the shielding current density that minimizes the energy over all space. Because energy is minimized over all space the shield current densities obtained using this method are best applied in situations similar to that of an insert coil. In these cases, one is interested in reducing the interaction between the insert coil and the rest of the scanner, which encompasses a volume much larger than that of the insert coil. For the second design example presented in this paper (the planar shield), the present method is shown to achieve an effective shield over a reduced area (i.e. one side of the initial coil); however, it was not a highly localized area. The case of the device shielding mentioned above is an example of a highly localized shielding problem. Highly customized local shielding applications may be better dealt with using a numerical field-constraint method (2) and this comparison is one that could be made in future work on this topic.

Other coil design methods have the capacity to design coils of arbitrary geometry. Brown et al. (21) demonstrated that the SUSHI method could be used to design coils of arbitrary geometry. The method described here has not been directly compared against the SUSHI method, though this would be an interesting avenue for future work. Asymmetric cylindrical gradient and shims coils have also been described previously (22,1). The method described here would not be expected to provide improved coil designs as compared to these asymmetric coils; however, if the geometries were in any way not purely cylindrical, the minimum energy method would still be applicable.

A related application for this method is that of eddy current modeling. The minimum energy method yields the current density on an arbitrary conducting surface that would cancel the magnetic field within and beyond that conducting surface. This current density can be considered an active shield (as has been done in this paper); however, it could also be considered to be a transient eddy current induced on the conducting surface. In other words, the spatial distribution of eddy currents on the conducting structures within an MR system could be modeled provided the geometry of these structures is known. However, this method as described in this paper would not directly yield the amplitude of the eddy currents on the conducting surfaces, which is a function of primary coil current waveform, and the composition of the conducting surfaces. Regardless, the ability to estimate the spatial variation of eddy currents inside a realistic scanner geometry is potentially useful in analyzing eddy current induced field effects in MR.

### 3.5 References

1. Chronik BA, Alejski A, Rutt BK. 2000 Design and fabrication of a three-axis edge ROU head and neck gradient coil. *Magnetic Resonance in Medicine*;44(6):955-963.
2. Poole M, Bowtell R. 2007 Novel gradient coils designed using a boundary element method. *Concepts in Magnetic Resonance Part B-Magnetic Resonance Engineering*;31B(3):162-175.
3. Gilbert KM, Gati JS, Klassen LM, Menon RS. A cradle-shaped gradient coil to expand the clear-bore width of an animal MRI scanner. *Phys Med Biol*;55(2):497-514.
4. Mansfield P, Chapman B. 1986 Active Magnetic Screening of Gradient Coils in Nmr Imaging. *Journal of Magnetic Resonance*;66(3):573-576.
5. Turner R, Bowley RM. 1986 Passive Screening of Switched Magnetic-Field Gradients. *Journal of Physics E-Scientific Instruments*;19(10):876-879.
6. Turner R. 1988 Minimum Inductance Coils. *Journal of Physics E-Scientific Instruments*;21(10):948-952.
7. Crozier S, Doddrell DM. 1993 Gradient-Coil Design by Simulated Annealing. *Journal of Magnetic Resonance Series A*;103(3):354-357.
8. Peters AM, Bowtell RW. 1994 Biplanar gradient coil design by simulated annealing. *Magnetic Resonance Materials in Physics, Biology and Medicine*;2(3):387-389.
9. Tomasi D. 2001 Stream function optimization for gradient coil design. *Magnetic Resonance in Medicine*;45(3):505-512.
10. Yoda K. 1990 Analytical Design Method of Self-Shielded Planar Coils. *Journal of Applied Physics*;67(9):4349-4353.
11. Bowtell R, Mansfield P. 1991 Gradient Coil Design Using Active Magnetic Screening. *Magnetic Resonance in Medicine*;17(1):15-21.
12. Martens MA, Petropoulos LS, Brown RW, Andrews JH, Morich MA, Patrick JL. 1991 Insertable Biplanar Gradient Coils for Magnetic-Resonance-Imaging. *Review of Scientific Instruments*;62(11):2639-2645.
13. Petropoulos LS, Martens MA, Brown RW, Thompson MR, Morich MA, Patrick JL. 1993 An Mri Elliptic Coil with Minimum Inductance. *Measurement Science & Technology*;4(3):349-356.

14. Carlson JW, Roos MS. 1995 Shielded Gradient Coils on Hyperbolic Surfaces of Revolution. *Magnetic Resonance in Medicine*;34(5):762-769.
15. Liu HY, Petropoulos LS. 1997 Spherical gradient coil for ultrafast imaging. *Journal of Applied Physics*;81(8):3853-3855.
16. Petropoulos LS, Morich MA. 1997 Novel gradient coil set with an interstitial gap for interventional nuclear magnetic resonance applications. *Ieee Transactions on Magnetics*;33(5):4107-4109.
17. Pissanetzky S. 1992 Minimum Energy Mri Gradient Coils of General Geometry. *Measurement Science & Technology*;3(7):667-673.
18. Lemdiasov RA, Ludwig R. 2005 A stream function method for gradient coil design. *Concepts in Magnetic Resonance Part B-Magnetic Resonance Engineering*;26B(1):67-80.
19. Jackson JD. *Classical Electrodynamics*. New York: John Wiley & Sons Inc.; 1998.
20. Shvartsman SM, Brown RW, Cheng YCN, Eagan TP, Fujita H, Morich MA, Petropoulos LS, Willig JD. 2001 Application of the SUSHI method to the design of gradient coils. *Magnetic Resonance in Medicine*;45(1):147-155.
21. Brown RW, Cheng YCN, Eagan TP, Kidane TK, Mathur H, Petschek RG, Sherwin WG, Shvartsman SM, Willig JD. 2002 Toward shielding improvements in MRI gradients and other systems. *Magnetic Resonance Materials in Physics Biology and Medicine*;13(3):186-192.
22. Forbes LK, Crozier S. 2001 Asymmetric zonal shim coils for magnetic resonance applications. *Medical Physics*;28(8):1644-1651.

## Chapter 4

### 4 Design and construction of a high-power insert gradient and shim system for dynamic shimming in small animal MRI

#### 4.1 Introduction

Almost every application in MR requires a spatially homogeneous main magnetic field for imaging. Main field ( $B_0$ ) imperfections can be devastating to many imaging applications. Gradient echo based imaging applications can suffer signal loss or image distortion depending on the size and spatial variation of the  $B_0$  inhomogeneities (1). Large-scale slowly varying distortions result in misplacement of signal; whereas small-scale sharp field distortions result in signal loss (dephasing). Magnetic resonance spectroscopy (MRS), which can be a powerful tool for extracting metabolic data, experiences greatly reduced spectral resolution when  $B_0$  inhomogeneities are present (2). Common to many imaging applications is the need to go to higher field strengths, which further amplify the problem, as  $B_0$  inhomogeneities scale with field strength (3).

Distortions in the main magnetic field of a typical MR system arise from two separate sources.  $B_0$  inhomogeneities of up to approximately 50 parts-per-million over the imaging volume may be present upon installation of the system. These inhomogeneities result from imperfections in the construction of the magnet.

The other major type of  $B_0$  inhomogeneity results from discontinuities in the magnetic susceptibility of the samples. The magnetic susceptibility difference between biological tissues, mainly air-tissue interfaces, distorts the magnetic field of the MR system – a distortion that is both sample and field strength dependent. These sample specific  $B_0$  inhomogeneities are much more problematic in MR than system specific distortions.

The standard method for dealing with unwanted magnetic field distortions is known as shimming. Generally speaking,  $B_0$  shimming is the process of applying

additional magnetic fields that are optimized to compensate for magnetic field distortions. Shimming procedures can be characterized by the type of field distortions they correct for: system specific field distortions or sample induced field distortions.

Shimming system specific field distortions is typically accomplished via passive shimming techniques. Passive shimming is performed two ways. The first method is to introduce ferromagnetic material into the bore of the scanner and arrange it in such a way that it cancels out the unwanted  $B_0$  perturbations (4). This is usually done when a system is installed to correct for imperfections in the construction and installation of the system. In addition to using ferromagnets, many systems contain a set of superconducting shims (electromagnets) that can also be adjusted at installation to help reduce subject-independent  $B_0$  inhomogeneities. Passive shimming techniques require a fair deal of time and effort to be done correctly, and as result, once passive shims are adjusted correctly their positions are rarely changed.

Correcting for sample specific field distortions is typically accomplished using active shims, which are resistive electromagnets that are actively driven and can be adjusted easily to correct for various field distortions. Sample related field perturbations occur over more focused regions of interest inside the sample, and can be decomposed into weighted sums of spherical harmonic field distributions (5). A set of electromagnetic coils can be designed, where each coil corrects for a different harmonic term. These coils are known as room temperature shim coils, and they exist as a group, usually including up to at least second and sometimes even third order spherical harmonics. Active shim coils are adjusted for each scanning session and they make use of MR data to help guide the field correction process. Active shimming is standard on all commercially available MR systems today, and although it is a dynamic procedure in that the shim settings are different for different samples, it is traditionally a static procedure during a single scan.

The procedure is as follows: a sample is introduced for imaging, then MR data is acquired from which the correct shim settings are determined to allow for effective

imaging (6,7). Although variations of this procedure exist, the basic idea is always the same.

Further reductions in  $B_0$  inhomogeneities can be achieved by performing the active shimming procedure in a dynamic fashion (8). This type of strategy is known as dynamic shim updating and is a more advanced shimming technique that is not commercially available (9,10,11). Dynamic shimming is typically performed on a slice-by-slice basis, where separate shim settings are determined for each slice in an acquisition volume prior to the scan. As each slice is acquired during scanning, the optimal shim settings for that slice are applied. The drawback of this method is that shim systems are not designed for dynamic operation and sufficient time must be allowed for decay of eddy currents related to the switching of the shim settings (10,11).

Many efforts are ongoing to improve the dynamic shimming procedure in MR (12). The main goal for dynamic shimming is to be faster, and the limitation of this goal is inductive coupling with other shim axes and the scanner itself. The motivations for decreasing the switching times in the dynamic shimming procedure are many. First, current applications are limited by the time required for eddy currents to settle between shim updating and acquisition. Second, decreasing the size of the volume that is shimmed over reduces the number of harmonics needed to correct for the field distortions and can greatly improve the shim quality (13). However, reducing the size of the shimmed volume means increasing the number of shim settings that must be switched between, which further emphasizes switching capabilities. Lastly, correcting for  $B_0$  inhomogeneities in real-time as a result of patient motion would be an extremely desirable application of dynamic shimming that requires faster switching times (14). Many methods exist to correct for motion retrospectively, but each has its limitations (15). Real-time dynamic shimming would place stringent demands on the shimming hardware, particularly the shim coils themselves.

It is clear that improving shimming capabilities over existing technology requires either the addition of higher order shim axes or the ability to shim over smaller volumes of interest and update shim settings quickly between volumes. This work examines the

technical challenges associated with constructing a set of shim coils that is highly optimized for use with fast dynamic shimming applications. The shim set contains all first and second order shim axes plus  $z^0$ - and  $z^3$ -shims. The shim set is designed and constructed to operate at much higher power than common existing shim technology, and several techniques are utilized to reduce the eddy currents that would result from such switching speeds.

## 4.2 Methods

### 4.2.1 Design methods

The high powered shim set in this work consists of ten shim axes, up to and including all second order shims plus a third order zonal axes ( $z^0$ ,  $x$ ,  $y$ ,  $z$ ,  $xz$ ,  $yz$ ,  $z^2$ ,  $xy$ ,  $x^2-y^2$  and  $z^3$ ). The shim set is designed for mouse imaging applications with an imaging region of 6.0 cm in diameter. The inner diameter of the shim set is 9.2 cm and the outer diameter is 35.0 cm, small enough to fit inside a 7.0 T head-only Varian system.

All shim axes were designed using the same Fourier series minimum power method presented in chapter 2 (16) with 21 target field points spanning the region of interest. The  $z$ -gradient was designed using a boundary element (BE) method (17,18,19) so it could be split into two separate layers.

### 4.2.2 Minimization of mutual interactions

The major challenge associated with dynamic shimming is overcoming the inductive interactions that occur when the shims are switched rapidly. There are two types of inductive interactions that can occur: coupling between the shim axes and the surrounding system, and coupling between the shim axes themselves. There are several strategies available to deal with the coupling problems faced in this work and each will be discussed in detail.

One method for reducing the inductive coupling between shim axes is to design the wire patterns such that the mutual inductance between those particular axes is minimized. This is accomplished by adding an expression for the mutual inductance between the shim axes into the functional (equation 2.1 presented in chapter 2) and



minimizing. The mutual inductance between two coils parameterized in terms of current density is given by:

$$M = -\mu_0 R_1 R_2 \sum_m \int_{-\infty}^{\infty} j_{\phi}^m(k) J_{\phi}^{-m}(-k) I'_m(k R_1) K'_m(k R_2) dk \quad (4.1)$$

where  $R_1$  and  $R_2$  are the radii of each shim coil,  $j$  and  $J$  are the Fourier transforms of the current densities of each coil, and  $I$  and  $K$  are modified Bessel function of the first and second kind. Ultimately this method produced very inefficient shim coils and was abandoned for techniques described below.

Another method of dealing with coupling (both shim-shim and shim-system coupling) is to shield problem axes from each other or from the surrounding system. The mutual inductance was calculated between each shim coil design; and combined with the knowledge that zonal shim coils couple strongly with typical MR scanners, the axes that required active shielding were determined.

The most important strategy used for the reduction of mutual interactions for this shim set was that of strategic layering. An iterative approach was taken during the design phase whereby many shim sets were designed with the shim axes taking on different orderings, and the mutual interactions terms were calculated across all axes. General knowledge about shim coupling was used to find a reasonable starting point and then the ordering was adjusted to correct for any problems. Many factors were considered during this process. The gradient efficiencies limited where the first order coils could be located. The intrinsic efficiency of each shim axes was also considered. Axes that displayed strong coupling were pushed as far apart as possible. For axes that required shielding, the shields were located inside the primary coils of any axes they coupled strongly with to prevent cascading interactions (*i.e.* even order zonal shields were placed inside the next closest even order zonal shim and similarly for the odd ordered axes). Also, with respect to the shields, they were located as far away from their corresponding primary coils to further increase efficiency. Finally, a separate layer, which will be discussed in more detail below, dedicated for cooling return lines was strategically

located to further separate the zonal shields from their corresponding primary coils. The shim layering that was used is presented in detail in the results section.

### 4.2.3 Cooling strategy

Because of the power requirements of each shim axis, water cooling was necessary to prevent the shim set from overheating. Due to lack of radial space, it was decided that hollow wire would be used so as to combine the cooling layers directly with the current carrying layers. The cooling requirements also played a part in determining the final ordering of the shim axes. Cooling layers were chosen based on their cooling capacity (wire length) and their relative position in the shim set. Because the gradient coils will typically be driven harder than the other axes, cooling layers were concentrated around them. Four cooling layers were chosen, and it was decided that the most efficient way to spread the cooling throughout the shim set was to split the  $z$ -coil into two separate layers. Both  $z$ -layers along with the  $z^0$ -shielding layer and the  $z^2$ -shielding layer were wound with hollow wire and acted as cooling for the whole shim set. To maximize the cooling achieved, each cooling axis was connected in parallel with the aid of a manifold. To save on radial space, a single layer in the center of the shim set was reserved for bringing the water connections back out of the insert coil.

### 4.2.4 Fabrication methods

#### 4.2.4.1 Zonal shims

The zonal shim axes were all wire wound, meaning that the conductor path was cut into a former and then wire was pressed into the groove (20). The zonal shims that were not dedicated cooling layers were wound with 10-gauge copper wire, with the exception of the  $z^3$ -shim, which was wound with 12-gauge copper wire. The wire paths were milled directly into hardened epoxy (50-3100 thermally conductive resin, Epoxies, Etc, Cranston, USA) or in the case of the  $z^0$ -coil the inner G10 (fiberglass) former on a lathe. Joining concentric wire paths required a “trough” to be cut, using an end mill, longitudinally and the wires were simply jogged over (see figure 4.4). Milling and cutting into the epoxy required diamond bit tools because of the extreme abrasiveness of the epoxy.

The zonal shims that were dedicated cooling layers were constructed in the same fashion as the other zonal coils. However, the wire used was 5-gauge copper wire with a square cross-section and 3.0-mm-diameter hole inside. The wire paths for the hollow wire were cut in the same fashion. Special connectors had to be fabricated to join together hollow wire at connection points or when the wire needed to turn a corner and could not be bent without pinching the inside hole. These connectors were machined out of brass, and they were designed and built to complete both the electrical circuits in series, and the water circuits in parallel.

#### 4.2.4.2 Transverse shims

The transverse shim axes ( $x$ ,  $y$ ,  $xz$ ,  $yz$ ,  $xy$  and  $x^2-y^2$ ) were fabricated in a different manner than the zonal shims. The conducting path was cut out of flat copper sheets leaving behind the inverse of the designed wire pattern, which is known to be electromagnetically equivalent (20). The copper sheets were 0.125 inches thick and 99.9% oxygen-free, which was chosen for ease of machining and not the added conductivity. The wire patterns were subsequently backed with a flexible electrically insulating epoxy, rolled to the desired radius, and then fastened to the coil. Each thumbprint was machined separately and were then wired together using a braided ground strapping which helped to save on radial space.

#### 4.2.4.3 Integration

The entire shim set was fabricated one layer at a time. The inner former was made of G10 (fiberglass) and the  $z^0$ -coil was cut directly into it. After the conductor was either pressed, or glued, in place the entire insert coil was potted in epoxy. After each layer was encased in epoxy it was turned down, using a lathe, to the correct radius for the next shim coil and the procedure was repeated. This ensured each layer would be concentric with the others. In some cases it was possible to attach two shim layers to the coil simultaneously – this was done for the  $z_B$ - and  $xz$ -shim layers, as well as the  $xy$ - and  $x^2-y^2$ -layers.

Two different potting procedures were followed depending on the physical complexity of the layer that was to be potted. In most cases a mould was constructed out

of PVC at a radius larger than the next shim layer and the epoxy was simply poured into the mould and left to set. In one instance it was determined that enough cavities existed to necessitate a vacuum potting procedure. The vacuum potting procedure was very much the same except the insert coil and mould were placed in a vacuum chamber, the air was removed from the chamber and the epoxy was drawn into the mould through a tube in the chamber. The advantage of vacuum potting is that the epoxy fills air cavities in the coil more easily, resulting in a stronger pot. Vacuum potting was done for the  $z_B$ -shield and  $xz$ -layers, which were attached to the coil simultaneously, and for the final pot.

The equipment used to machine the wire patterns operated to very precise tolerances, so the uncertainty in wire position is quite small (fractions of a millimeter). However, great care had to be taken in fastening the transverse coils to the structure as this was done by hand. To ensure the coils were correctly positioned with respect to each other several reference points were cut into the original G10 former, and as the coil grew in size and layers it was possible to continually reference off those marks.

In the center of the shim set an empty layer was left for the purpose of returning the wires and the cooling lines back to the back end of the coil (as was previously mentioned). Running each line back over its own layer would have taken up far too much radial space, so a separate layer was dedicated to bringing all the electrical and cooling lines back. Wires that were already in place were brought back through the grooves milled in the empty layer. For the layers that had yet to be constructed Teflon tubes were buried so the wires could be run back at a future date.

#### 4.2.5 Testing

The completed shim insert was tested and compared against the original design expectations. The circuit parameters (L and R) for each shim axis were measured using an INSTEK LCR-800 LCR meter. The resistance and inductance of each coil was measured at 0.012, 0.1, and 1.0 kHz. The error on the resistance and inductance measurements was given by the precision of the LRC meter plus an estimated value that accounts for the changing position of the connection leads, which was determined experimentally.

The magnetic field profiles for each shim axis were measured using a 3-axis magnetic field transducer manufactured by Senis, model number: C-H3A-2m-E3D. The insert coil was fastened to a table and the field transducer was fixed to an end mill with a digital read out for precise positioning. Field measurements were taken along “lines of interest” to capture the desired field profile for calculating the shim efficiency. For the zonal shims the field was measured along the  $z$ -axis in 5.0 mm increments from -30.0 mm to 30.0 mm, which spanned the imaging region. For the  $x$ - and  $y$ -coils the same was done along the  $x$ - and  $y$ -axes. The line  $x=z, y=0$  was used for the  $xz$ -shim with steps  $\sqrt{50}$  mm increments taken along the line. The same was done for the  $yz$ -shim along the line  $y=z, x=0$ , and for the  $xy$ -shim along  $x=-y, z=0$ . The field measurements for the  $x^2-y^2$ -coil were taken along the  $x$ -axis. At every point 10 field measurements were taken and the average was reported. The uncertainties in the field measurements were obtained by repeating measurements along each line and calculating the standard deviation.

The efficiency of each shim coil was determined from the field measurements and compared against the efficiency calculated from the simulated magnetic field profiles. The efficiency was determined by fitting the desired field profile to the measured field points over the imaging region. The corresponding fit parameter is the efficiency given in mT/m<sup>n</sup>/A. To facilitate comparison with the original designs the exact same field points were used for fitting the simulated field profiles for each coil.

The mutual interactions between shim axes were calculated for the original designs and measured for the actual insert coil. Calculating the mutual inductance for the simulated wire patterns was done in MATLAB<sup>®</sup> version 7.11.0 via the Neumann formula. Determining the mutual inductance between axes for the actual insert coil required a multi step process. The coil of interest was driven with a 1.0 kHz sine wave using an Agilent 33220A function generator with a 10.0 V output. Next, both the voltage on the driving coil and the induced voltage on the coupled coil were measured with an oscilloscope. From these measurements the mutual inductance was calculated via:

$$M = L_{drive} \frac{V_{induced}}{V_{drive}}, \quad (4.2)$$

where the subscript *drive* indicates the coil that is being driven and the subscript *induced* indicates the coil that is not. The uncertainties in the mutual inductance measurements were derived using standard error propagation techniques.

The final measurements performed for the insert shim coil were cooling measurements. The cooling capacity of each layer was determined for the original designs using a model based on the Darcy-Weisbach equation (21). The simulated cooling capacities were then compared against the measured values, which were determined as follows. Each cooling layer was connected to a standard sink tap via a flow regulator. The flow was set to 20 PSI and the time required for a 500 mL container to be filled was measured. The measurements were repeated twice for each cooling layer and the flow rate was calculated from the averages for each layer. The cooling capacity of each cooling layer was calculated from the flow rates via:

$$Q = mc\Delta T, \quad (4.3)$$

where  $Q$  is the heat removed by the cooling layer per unit of time,  $m$  is the mass flow rate,  $c$  is the specific heat of water (4186 J/kgK) and  $\Delta T$  is the allowed temperature change, which was 20.0 K.

## 4.3 Results

### 4.3.1 Design results

The original wire patterns, designed using MATLAB<sup>®</sup>, are given in figure 4.1 for each individual coil including shielding coils. These are the exact wire patterns (excluding connection leads) that were eventually used for fabrication. Table 4.1 gives the efficiency and circuit parameters for each shim axis (both simulated and measured). The values given for the zonal shims are for the fully shielded shim axes. Table 4.2 shows the effects of shielding on the zonal shims by examining the shielding ratio, which is the efficiency of the shielded shim divided by the efficiency of the unshielded shim coil.

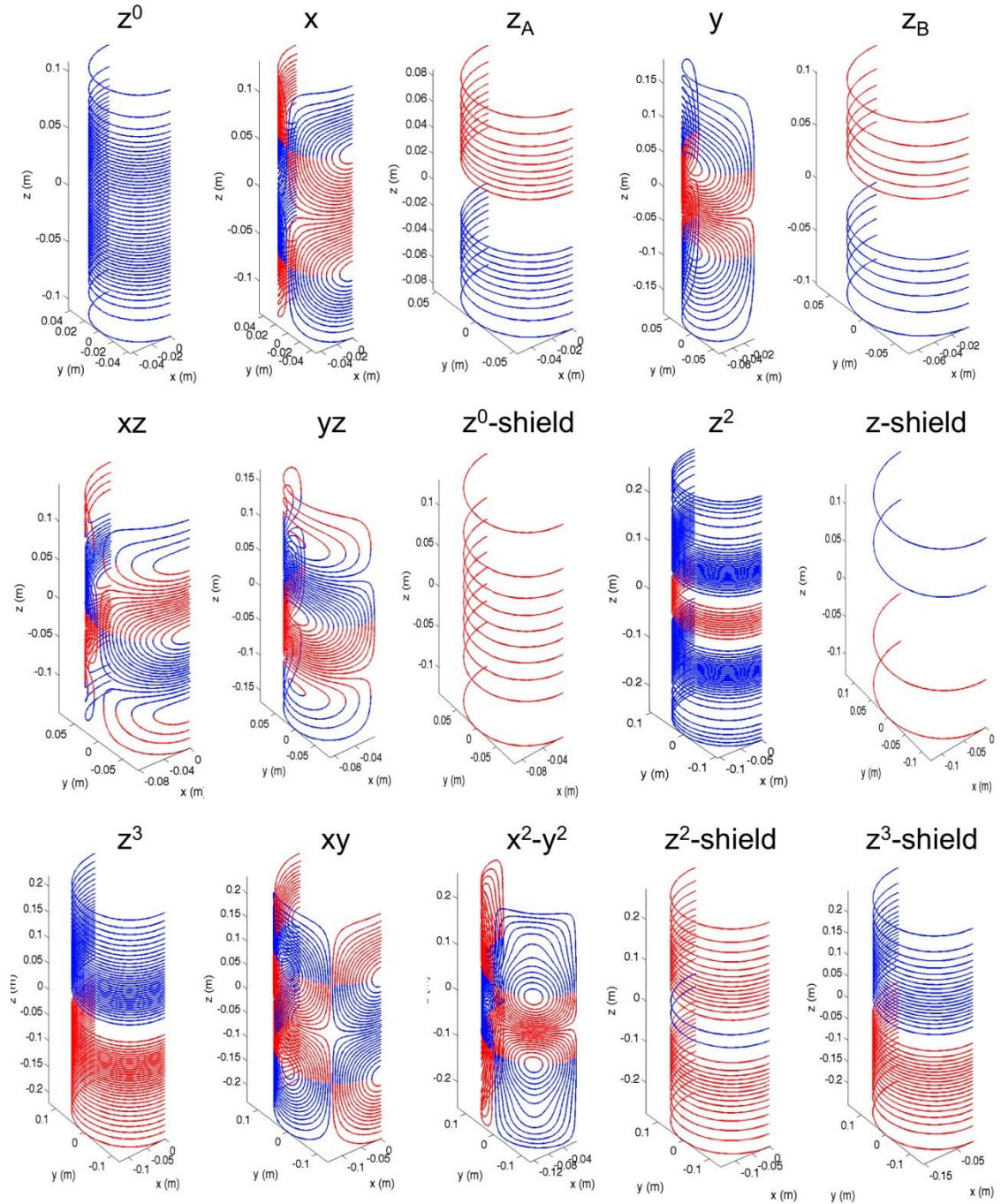


**Figure 4.1:** One half of the simulated wire pattern for each coil in the shim set. The red and blue color coding indicate the current direction. The coils increase in radius from the  $z^0$ -coil out to the  $z^3$ -shield. Note that no connection leads are shown.

**Table 4.1:** The efficiency, inductance and resistance values (both simulated and measured) for each shim coil.

	Simulated			Measured		
	$\eta$ [mT/m <sup>n</sup> /A]	L [ $\mu$ H]	R [m $\Omega$ ]	$\eta$ [mT/m <sup>n</sup> /A]	L [ $\mu$ H]	R [m $\Omega$ ]
$z^0$	0.29	71.0	64.1	$0.3 \pm 0.1$	$79 \pm 1$	$70.4 \pm 0.5$
$x$	4.54	72.9	55.0	$4.02 \pm 0.03$	$63 \pm 1$	$67.0 \pm 0.5$
$y$	3.02	78.2	65.7	$2.72 \pm 0.06$	$64 \pm 1$	$72.5 \pm 0.5$
$z$	3.14	36.4	49.8	$2.97 \pm 0.08$	$41 \pm 1$	$78.1 \pm 0.5$
$xz$	21.52	62.3	60.7	$18.92 \pm 0.02$	$50 \pm 1$	$63.5 \pm 0.5$
$yz$	18.10	77.8	71.9	$16.49 \pm 0.01$	$64 \pm 1$	$77.1 \pm 0.5$
$z^2$	14.79	220.2	264.4	$14.47 \pm 0.01$	$250 \pm 1$	$282.1 \pm 0.5$
$z^3$	52.18	197.4	480.4	$56.385 \pm 0.008$	$241 \pm 1$	$602.5 \pm 0.5$
$xy$	6.49	159.9	147.1	$5.128 \pm 0.008$	$118 \pm 1$	$104.7 \pm 0.5$
$x^2-y^2$	5.55	213.0	165.6	$4.423 \pm 0.009$	$169 \pm 1$	$146.8 \pm 0.5$

**Table 4.2:** The shielding efficiency ratios (both simulated and measured) for the zonal shim coils.

	$\eta_s/\eta_p$ Simulated	$\eta_s/\eta_p$ Measured
$z^0$	0.87	$0.9 \pm 0.6$
$z$	0.97	$0.96 \pm 0.05$
$z^2$	0.89	$0.923 \pm 0.001$
$z^3$	0.83	$0.9545 \pm 0.0003$

The magnetic field measurements, along with the fitting function for each coil evaluated over the imaging region, are shown in figure 4.2 below. The magnetic field profile calculated from the original simulated wire patterns has been plotted as well, and fairly good agreement can be seen.



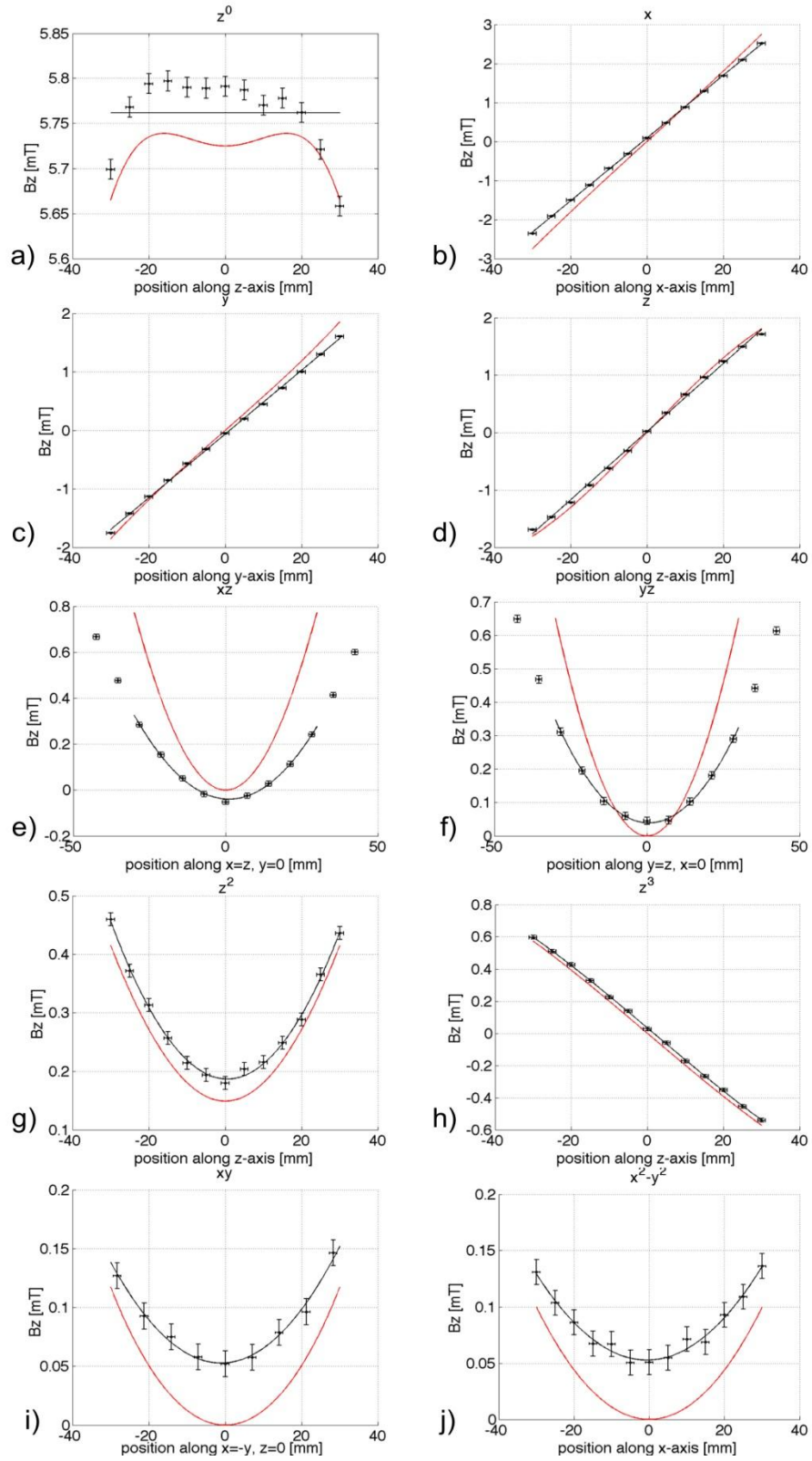


**Figure 4.2:** The fitted (black) and simulated (red) magnetic field profiles over the imaging region for each shim axis.

### 4.3.2 Minimization of coupling

The first strategy for eddy current reduction was to shield shim axes that displayed significant coupling. Only the zonal coils required shielding, and furthermore, each zonal coil only needed to be shielded with respect to other zonal coils that shared the same symmetry. In other words, the even order zonal coils had to be shielded with respect to each other and the same for the odd orders. Shielding the zonal coils served dual purpose as it is well known that these coils couple to the conducting structures of MR systems. Table 4.4 shows the effect on the mutual inductance as a result of shielding the zonal coils from each other.

**Table 4.3:** The simulated and measured mutual inductance for the shielded and unshielded even order and odd order zonal coils.

	M Simulated [ $\mu\text{H}$ ]	M Measured [ $\mu\text{H}$ ]
$z^0$ - $z^2$ unshielded	23.7	$23.7 \pm 8.2$
$z^0$ - $z^2$ shielded	1.4	$2.4 \pm 5.9$
$z$ - $z^3$ unshielded	31.5	$27.6 \pm 7.2$
$z$ - $z^3$ shielded	2.4	$5.0 \pm 5.5$

The second strategy for coupling reduction was to strategically order the coils to reduce these effects. The order of the shim axes and the placement of the shielding coils and cooling line return path are shown below in figure 4.3.

$z^0$ : $r = 4.3$ cm, thickness = 0.4 cm
$x$ : $r = 4.7$ cm, thickness = 0.7 cm
$z_A$ : $r = 5.4$ cm, thickness = 1.0 cm
$y$ : $r = 6.4$ cm, thickness = 0.7 cm
$z_B$ : $r = 7.1$ cm, thickness = 1.0 cm
$xz$ : $r = 8.1$ cm, thickness = 0.7 cm
$yz$ : $r = 8.8$ cm, thickness = 0.7 cm
$z^0$ shield: $r = 9.5$ cm, thickness = 1.0 cm
$z^2$ : $r = 10.5$ cm, thickness = 0.5 cm
cooling line return layer, $r = 11.0$ cm, thickness = 1.0 cm
$z$ shield: $r = 12.0$ cm, thickness = 0.5 cm
$z^3$ : $r = 12.5$ cm, thickness = 0.5 cm
$xy$ : $r = 13.0$ cm, thickness = 0.7 cm
$x^2$ - $y^2$ : $r = 13.7$ cm, thickness = 0.7 cm
$z^2$ shield: $r = 14.4$ cm, thickness = 1.0 cm
$z^3$ shield: $r = 15.4$ cm, thickness = 0.5 cm

**Figure 4.3:** A schematic representation showing the ordering of the shim layers inside the shim set. The cooling layers are shown in blue, green represents the return line layer that does not house a shim coil, and the rest of the coils are shown in gray.

### 4.3.3 Cooling

The power for each shim layer calculated from the simulated and measured (at 1.0 kHz) resistances, is given in table 4.5. These values are calculated for operating currents of 100.0 A for the first order shims and 50.0 A for all other coils.

**Table 4.4:** The power (both simulated and measured) for each shim axes in the insert coil.

	Power [W]	
	Simulated	Measured
$z^0$	160	$176 \pm 1.3$
$x$	553	$670 \pm 5.0$
$y$	658	$725 \pm 5.0$
$z$	501	$781 \pm 5.0$
$xz$	152	$159 \pm 1.3$
$yz$	180	$193 \pm 1.3$
$z^2$	659	$705 \pm 1.3$
$z^3$	1201	$1506 \pm 1.3$
$xy$	368	$262 \pm 1.3$
$x^2-y^2$	415	$367 \pm 1.3$
Total	4847	$5544 \pm 24$

The flow rates for each cooling layer were both simulated and measured and the cooling capacities were subsequently calculated. The values are given in table 4.6.

**Table 4.5:** The cooling capacity for each cooling layer calculated from both simulated and measured flow rates at 20 PSI with a 20.0 K allowable temperature gradient.

	Cooling Capacity [W]	
	Simulated	Measured
$z_A$	1065	$816 \pm 24$
$z_B$	1222	$980 \pm 31$
$z^0$ -shield	1146	$983 \pm 31$
$z^2$ -shield	455	$390 \pm 10$
Total	3888	$3169 \pm 96$

#### 4.3.4 Fabrication

The original wire pattern designs were used as the basis for fabrication. However, the fabrication process was different for both the longitudinal shims and transverse shims.

##### 4.3.4.1 Zonal shims

The longitudinal wire patterns were machined using a lathe directly into their corresponding formers for each layer. Figure 4.4 shows the  $z^0$ -coil, which was machined directly into the inner G10 former and wound with 10-gauge copper wire.

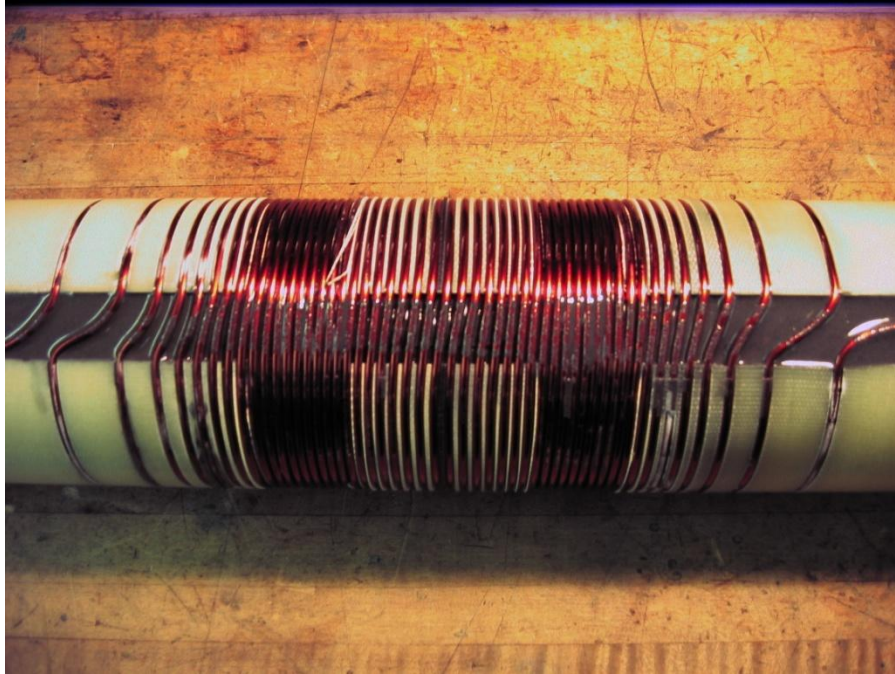


**Figure 4.4:** A photograph of the  $z^0$ -primary coil machined directly into the G10 former. This is the inner-most coil in the shim set and the first one fabricated. All other coils were referenced off this one.

All the zonal shims were fabricated using the same process, the only difference between layers was the type of wire used for each. Figure 4.5 shows the second layer of the  $z$ -shim ( $z_B$ ) which was wound using 5-gauge square copper wire with a 3.0-mm-diameter hole in the middle for water flow. The brass connecting elbows (seen in figure 4.5) were fabricated to turn sharp corners.

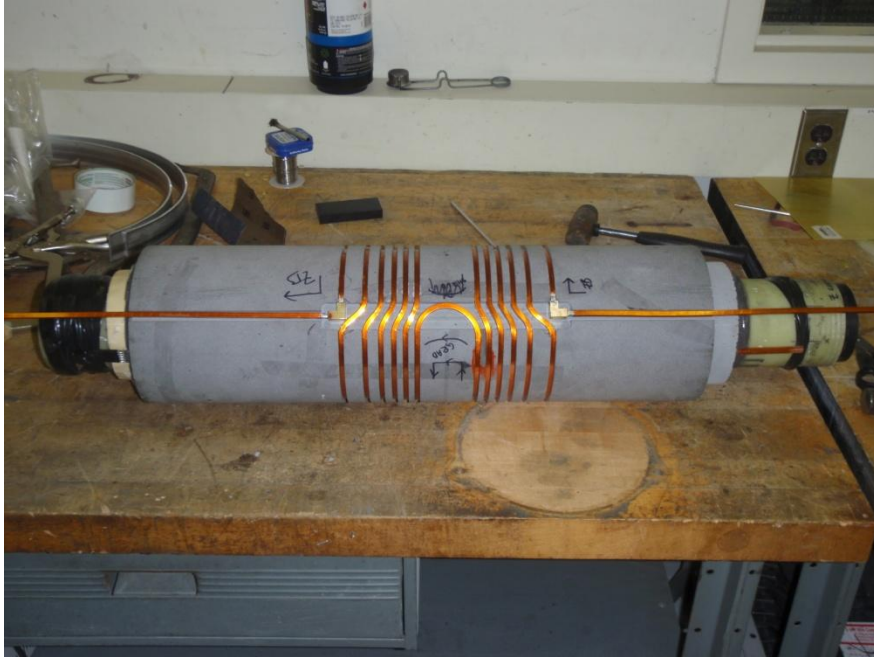


**Figure 4.5:** A photograph of the  $z_B$ -layer machined directly into the epoxy base and wound with hollow wire.

#### 4.3.4.2 Transverse shims

The fabrication process for the transverse shim axes was more complicated than that of the longitudinal. The wire patterns were cut from copper sheets on a CNC end mill as shown below in figure 4.6. Figure 4.7 shows the individual thumbprints of the  $xz$ -shim after they had been fixed with the epoxy backbone and rolled to the proper radius for installation on the insert coil. A 1.0 cm border was left around each individual conductor which allowed it to be fastened to the mill and aided in the rolling process, which was accomplished using a hand roller.



**Figure 4.6:** A photograph of a thumbprint of the  $xz$ -shim being milled by the CNC mill. The simulated wire patterns are fed directly into MasterCam X5<sup>®</sup>, the software that controls the end mill.



**Figure 4.7:** A photograph of the  $xz$ -shim coil after it had been rolled to radius. The 1.0 cm border is cut off before it is attached to the insert coil and wired together.

#### 4.3.4.3 Integration

The power requirements of the shim set combined with the limited radial budget placed stringent tolerances on the overall fabrication process. The techniques for integrating all the shim axes together were unconventional, however, quite robust. Figure 4.8 shows the  $xz$ -shim being fastened to the insert coil using Loctite<sup>®</sup> 411 glue and hose clamps.



**Figure 4.8:** A photograph of the  $xz$ -shim coil being fastened to the insert coil. Hose clamps were used to squeeze the coil and remove flat spots resulting from the rolling procedure. Connection leads are not yet present.

The separate layer allocated for all the return lines (both electrical and cooling) is shown in figure 4.9.



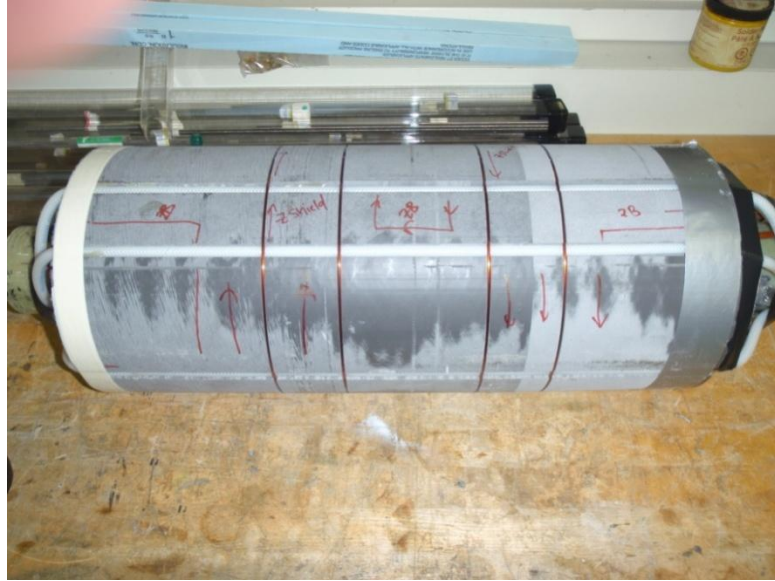


**Figure 4.9:** A photograph of the return path layer. Silicon hoses were embedded to bring cooling fluid (water) back out of the coil from each cooling layer. Several electrical leads had to be run back through this layer.

Figure 4.10 shows the potting procedure that was used for most shim layers, which was simply filling a mould with epoxy. Excess epoxy was used for each layer and then the entire coil was machined down to the correct radius to accept the next shim coil. This technique made it easy to keep the shim coils concentric.



**Figure 4.10:** A photograph of the basic potting procedure for each layer. A mould was constructed from a plastic cylinder and masking tape and the epoxy was simply poured in and left to set.

## 4.4 Discussion

A high power shim insert coil customized for the purpose of dynamic shimming has been designed, constructed and bench tested. Experimental techniques have been employed and validated at both the design and fabrication level for this insert coil.

The final shim designs compared quite well with simulated results. The resistances of the constructed shim coils were greater than the simulated values in most cases, which is a result of connection leads that were not included in the original designs. In a few cases ( $xy$ - and  $x^2$ - $y^2$ -shims) the resistances were actually lower. This is due to the nature of construction of the transverse coils where the conductor path is allowed to vary in width. The original resistance simulations only produce a maximum resistance based upon the minimum separation of the conducting path. The inductance values for each shim agree reasonably well with expected results. The variations are consistent in that for all zonal coils the measured inductances are greater than the simulated inductances and for all transverse shims the opposite is true. The larger inductance values for the zonal shims is likely a result of connection leads, and the lower inductances for the transverse shims are due to the difference in effective wire patterns that result from the “inverse milling procedure” used. The measured efficiency values for the shims are consistently less than the expected efficiencies, with the exception of the  $z^0$ -shim. These discrepancies are likely the result of errors in coil positioning (both during the fabrication process and the field measurement process).

The measured field profiles of the final shim coils are very much as expected. Offsets can be seen in the field profiles of the second order transverse coils, which suggest that the insert coil was slightly displaced azimuthally during the measurement process. The  $xy$ - and  $x^2$ - $y^2$ -coils are less efficient, resulting in a greater relative effect from the misalignment. The inner most shim coils had imaging regions that conformed well to design specifications. However, it can be seen that as the coils grew in radius the imaging regions expanded beyond the desired size. This is a natural consequence of the Biot-Savart law and cannot be avoided in practice.

The measured mutual inductances between the shim axes agreed surprisingly well with the simulated values, as did the cooling measurements. From the results section the total measured power of the shim set was 5.5 kW and the total cooling capacity was 3.2 kW, which suggest that the shim set is under-cooled. However, this is not the case. The cooling measurements were limited to 20.0 PSI (tap pressure in the building), whereas a typical chiller may operate at something closer to 45 PSI, giving the insert coil far greater cooling capacity. The simulated cooling capacity of the system at 45 PSI, holding the other variables constant, is 6.2 kW. It should also be noted that the total measured power assumes all shim coils are being operated at full power with 100% duty cycle. It is unlikely this situation will ever occur.

The overall design of this shim set is a function of its intended application. Every aspect of this coil was optimized for purpose of high power and eddy current reduction, which is very evident in the ordering and shielding of the shim axes. The shim ordering was designed solely for the purpose of reducing interactions between shim axes. If one was interested in a high power shim set that was not intended to be used dynamically many adjustments to the design could be made to improve the shimming capability. Higher order shim axes are intrinsically less efficient and it would be best to place these shims closer to the imaging region if possible.

Many aspects of the fabrication process used for this insert coil were experimental, yet worked very well. The most questionable part of the fabrication process was the technique of building one shim at a time and potting every layer separately. The alternative to this technique would be to build each layer on its own former, fix them together and pot the entire coil in one shot. There are advantages and disadvantages to both methods. The method chosen was very robust; it allowed careful control in the radial direction and did not require extra coils formers, which would consume a portion of the radial budget. The downfall is that the integrity of the coil is reduced because all the layers are not potted together; although the degree to which this could be a problem is hard to predict.

The final product of this work is a shim set that operates at higher power and faster switching speeds than any previously constructed shim insert coil that the author is aware of. Each shim axes operates at gradient strengths and gradient switching speeds. The slowest axis ( $z^2$ ) has a switching time of approximately 125  $\mu$ s assuming a 50 A, 100 V power supply, which means that shim current updating could be performed well within the rise time of a typical gradient pulse.

The applications of such a shim set are numerous from real time subject motion correction to shimming the field distortion from a moving instrument inside the MR system. Other applications, such as imaging around implants could benefit from such an insert coil. Some implants disrupt the field too much for a conventional shim system to correct. A high power shim system like the one described in this work would be capable of correcting for larger field distortions paving the way for imaging applications that were previously off limits.

## 4.5 References

1. Deichmann R, Josephs O, Hutton C, Corfield DR, Turner R. 2002 Compensation of susceptibility-induced BOLD sensitivity losses in echo-planar fMRI Imaging. *Neuroimage*;15(1):120-135.
2. de Graaf RA. *In Vivo NMR Spectroscopy: Principles and Techniques*. New York: Wiley; 1998.
3. Farahani K, Sinha U, Sinha S, Chiu LCL, Lufkin RB. 1990 Effect of Field-Strength on Susceptibility Artifacts in Magnetic-Resonance-Imaging. *Computerized Medical Imaging and Graphics*;14(6):409-413.
4. Chen CN, Hoult DI. *Biomedical Magnetic Resonance Technology*. New York: Adam Hilger; 2005.
5. Romeo F, Hoult DI. 1984 Magnet Field Profiling - Analysis and Correcting Coil Design. *Magnetic Resonance in Medicine*;1(1):44-65.
6. Schneider E, Glover G. 1991 Rapid Invivo Proton Shimming. *Magnetic Resonance in Medicine*;18(2):335-347.
7. Webb P, Macovski A. 1991 Rapid, Fully-Automatic, Arbitrary-Volume Invivo Shimming. *Magnetic Resonance in Medicine*;20(1):113-122.
8. Blamire AM, Rothman DL, Nixon T. 1996 Dynamic shim updating: A new approach towards optimized whole brain shimming. *Magnetic Resonance in Medicine*;36(1):159-165.
9. Morrell G, Spielman D. 1997 Dynamic shimming for multi-slice magnetic resonance imaging. *Magnetic Resonance in Medicine*;38(3):477-483.
10. de Graaf RA, Brown PB, McIntyre S, Rothman DL, Nixon TW. 2003 Dynamic shim updating (DSU) for multislice signal acquisition. *Magnetic Resonance in Medicine*;49(3):409-416.
11. Koch KM, McIntyre S, Nixon TW, Rothman DL, De Graaf RA. 2006 Dynamic shim updating on the human brain. *Journal of Magnetic Resonance*;180(2):286-296.
12. Juchem C, Nixon TW, Diduch P, Rothman DL, Starewicz P, De Graaf RA. 2010 Dynamic Shimming of the Human Brain at 7 T. *Concepts in Magnetic Resonance Part B-Magnetic Resonance Engineering*;37B(3):116-128.
13. Poole M, Bowtell R. 2008 Volume parcellation for improved dynamic shimming. *Magnetic Resonance Materials in Physics Biology and Medicine*;21(1-2):31-40.

14. van Gelderen P, de Zwart JA, Starewicz P, Hinks RS, Duyn JH. 2007 Real-time shimming to compensate for respiration-induced B-0 fluctuations. *Magnetic Resonance in Medicine*;57(2):362-368.
15. Bernstein MA, King KF, Zhou XJ. *Handbook of MRI Pulse Sequences*. Burlington: Elsevier Academic Press; 2004.
16. Carlson JW, Derby KA, Hawryszko KC, Weideman M. 1992 Design and Evaluation of Shielded Gradient Coils. *Magnetic Resonance in Medicine*;26(2):191-206.
17. Pissanetzky S. 1992 Minimum Energy Mri Gradient Coils of General Geometry. *Measurement Science & Technology*;3(7):667-673.
18. Lemdiasov RA, Ludwig R. 2005 A stream function method for gradient coil design. *Concepts in Magnetic Resonance Part B-Magnetic Resonance Engineering*;26B(1):67-80.
19. Poole M, Bowtell R. 2007 Novel gradient coils designed using a boundary element method. *Concepts in Magnetic Resonance Part B-Magnetic Resonance Engineering*;31B(3):162-175.
20. Gilbert KM, Gati JS, Klassen LM, Menon RS. 2010 A cradle-shaped gradient coil to expand the clear-bore width of an animal MRI scanner. *Physics in Medicine and Biology*;55(2):497-514.
21. Brown G. 2002 The history of the Darcy-Weisbach equation for pipe flow resistance. *Environmental and Water Resources History*;38(7): 34-43.

## Chapter 5

### 5 A new approach to the challenges of siting MRI systems: active room shielding

#### 5.1 Introduction

The introduction of magnetic resonance imaging (MRI) as a clinical imaging modality in the early 1980's has led to the design and development of larger and more powerful magnets. This process has greatly increased the level of human exposure to large ambient magnetic fields. Common to almost all clinical MR systems are their enormous physical dimensions and very strong and homogeneous magnetic fields at their centers. Most clinical MR systems are cylindrical in nature and contain superconducting magnets responsible for generating their main magnetic fields, however, other systems exist that utilize permanent or resistive magnet technology (1,2).

Early superconducting conducting MR systems produced magnetic field strengths of approximately 0.05-0.1 T. Today, 1.5 T systems are the most common clinical field strength, 3.0 T systems are routinely installed, and it is not uncommon to have 7.0 T systems or higher installed at research sites. The trend of MR systems continually increasing in size (overall size, not necessarily bore size) and strength has raised many concerns over the fringe fields that modern systems produce. These concerns make siting and installation of MR systems a more challenging and important task. In the context of a clinical imaging facility, or hospital, the large magnetic field footprint poses many potential problems.

There are three separate sources of magnetic field exposure in MR: the static main field, the pulsed gradient field, and the radiofrequency field, each with its own risk profile. Both gradient switching and RF field exposure lead to their own patient safety concerns, however, the limitations on gradient switching speeds (3,4) and RF exposure well known (5,6). Also, gradient exposures are generally limited to a smaller region in the immediate vicinity of the scanner by the use of active shielding. RF exposures are

typically focused over the imaging region of the system, and not a concern at greater distances.

The limiting factors that establish acceptable static magnetic field exposures are not apparent and the current limitations on field strength are a combination of cost, technology, and regulation and not the inherent safety risks associated with static magnetic field exposure (3). Newer studies have shown that movement through the fringe field of an MR system can result in induced currents significant enough to cause effects in biological tissue (8,9). These effects include: headaches, nausea, vertigo, phosphenes, (light flashes) and numbness, just to name a few. Effects such as these should likely be incorporated into future safety guidelines. Other important safety concerns relating to the magnetic footprint of an MR system can include: magnetic object projectiles (3), medical implant compatibility (10-15), and imbedded magnetic objects in patients (16).

Aside from safety concerns, there are many compatibility issues associated with the MR systems static field in a hospital, or imaging facility. Strong magnetic fields are problematic for many electrical devices, as information can be wiped from hard disks. Important medical equipment, such as ventilators and other essential patient care equipment, can also be adversely affected by the main magnetic field (17,18).

In addition to general electrical and medical device compatibility, other imaging modalities are adversely affected by a strong magnetic field. It can be desirable to house all the medical imaging facilities in a hospital or clinical as close as possible, but the interaction of other modalities with the magnetic field of the MR system make this a challenging feat. The operation of positron emission tomography (PET) systems in the vicinity of an MR system is well documented (19). Acceptable tolerances for PET operation within a magnetic field range from 0.3 mT to 5.0 mT depending on the technology utilized (20). Medical devices essential to operation of many imaging modalities are also adversely affected by the direct presence of MR, such as a linear accelerator (21).



Although the interference issues and safety concerns associated with moving to higher field strength are many, the benefits of improved imaging and diagnostic capabilities far out-weigh them, and necessitate the need for solutions to the problem. A strong trend toward intraoperative MRI has placed even more emphasis on the need for more sophisticated solutions to the stray field problem in MRI (22,23).

There are two general methods for dealing with MRI fringe fields in practice. The simplest method is to locate the MR system far enough away from everything else, such that there are no issues. This represents an ideal situation, and in practice this is not always a viable option. The construction of an isolated housing area for an MR system can be very costly and in many situations there is simply not enough room to make it a reality.

The second and most widespread solution to the MR fringe field problem is to shield it. Shielding the static field can be done using two different techniques: passive shielding or active shielding. There are many instances where both methods are used in tandem (24).

Passive shielding is a technique that employs the use of ferromagnetic material (typically iron) placed in the vicinity of the MR system for the purpose of cancelling the magnetic field beyond a certain region. A passive shield can be placed within the MR system itself (primary passive shielding (25,26)) or further away from the MR system, such as in the walls of the MR room (secondary active shielding (24,27)). The benefits of placing the shielding material further from the magnet are two-fold. First, the shield has a limited impact on the overall efficiency of the MR system, and second, any asymmetries in the shape of the passive shield will have less of an impact on the homogeneity of the imaging region. The problem of course is that the further away from the MR system the shield is the larger the extent of the fringe field. Passive shielding is a technique that can be extremely costly and limit the siting options for an MR system. Today it is only common to larger research scanners, such as whole-body 7.0 T systems. The amount of iron necessary to correctly shield an MR system can be quite substantial, up to hundreds of tonnes (28), and aside from the cost of the iron itself, the sheer weight

can result in the need for structural modifications to the building or in extreme cases prevent the MR system from being installed at a particular location.

Active shielding employs current carrying conductors that are actively driven to cancel out or greatly reduce the stray magnetic field. Virtually all commercial MR systems are actively shielded, with the shielding windings being superconducting and housed in the same cryogen as the primary windings of the system (29). The result of this type of primary active shielding is a greatly reduced magnetic footprint. Actively shielded magnets are less efficient than unshielded magnets and are quite a bit larger in size, and mass, for a given field strength. However, for many clinical and even research facilities active shielding is a must in order to house high field systems.

A second type of active shielding is possible, which will be referred to as secondary active shielding, whereby the cancellation current is located not inside the MR system, but further from the system in close proximity to the areas that require shielding. Limited work has been done to explore the extent to which secondary active shielding can be of use in modern MR environments (30,31). This work examines the possibility of using a secondary active shielding technique to reduce stray field for several different cases ranging from inside the MR room, to rooms completely exterior to the MR room. The possibility of operating such active shields in a dynamic fashion to adapt to a changing MR environment is also explored.

Five specific cases (three static and two dynamic) where active shielding can be used to control the fringe field of the MR system are examined in this study. The first case is a shield placed in the walls, floor and ceiling of a room that houses the MR system for the purpose of eliminating the fringe field outside the MR room. The second case is a shield that encloses a room that is adjacent to the MR system for the purpose of reducing the field inside that room. This case was examined for two separate situations: when the room was adjacent in the transverse ( $x$ ) direction and when the room was adjacent in the longitudinal ( $z$ ) direction. The last static shielding case was a small equipment cabinet located inside the MR room that was shielded to reduce the field inside the cabinet. The first dynamic shielding application examined was a double-layered equipment cabinet

(two separate shields) that responded to the MR system moving in a straight line along  $z$ . The second dynamic case was a cart with four independent shielding layers that can be moved around in the vicinity of the main magnet. The details of each case are outlined below.

## 5.2 Methods

The active shields in this work were designed using the minimum energy method (32) presented in chapter 3. The minimum energy algorithm is an extension of previous boundary element (BE) methods (33,34,35) and is based on the assumptions that the current density to be shielded is known ahead of time, and that the geometry of the shield is known - assumptions that are valid for the shielding cases explored here.

The minimum energy algorithm is applied as follows. A known primary-coil current density is expressed by a set of current density amplitudes and a defined set of finite-element basis functions. For this study the primary current density was a 1.0 T shielded MR system based upon the design by Xu *et al.* (36), a schematic of which is shown in figure 5.1.

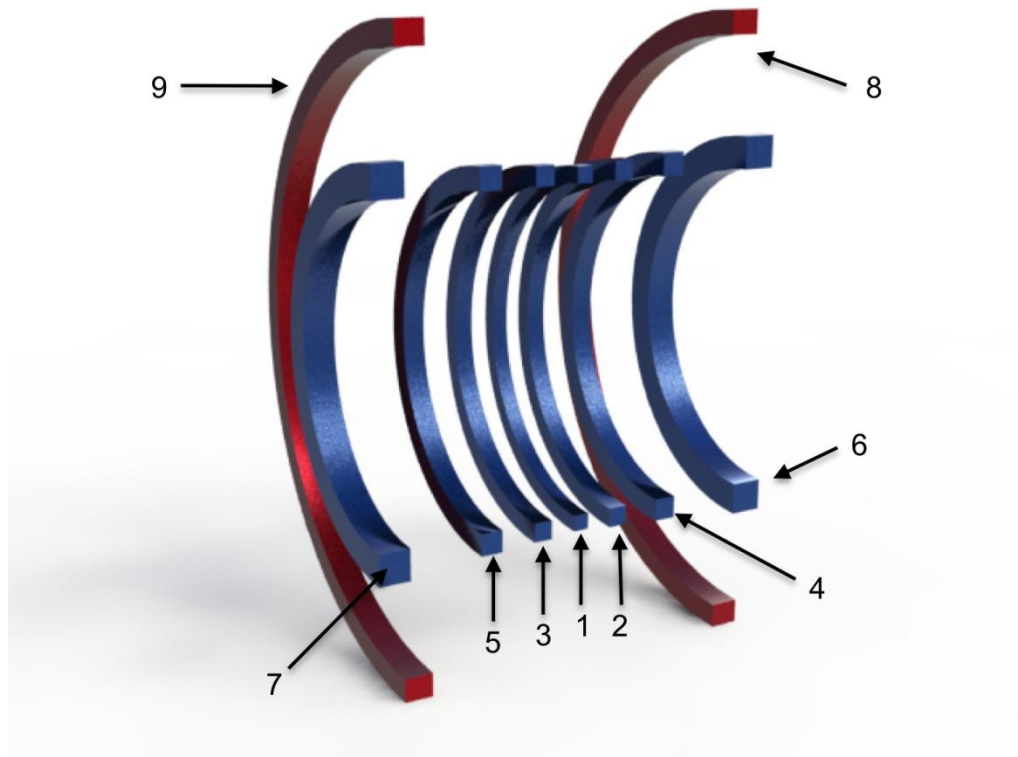


**Figure 5.1:** A cut-through schematic representation of the 1.0 T MR system used. Each winding carries 300 A, with the shielding windings (shown in red) carrying 300 A in the opposite direction to the primary windings (shown in blue). The imaging region for this system is 40.0 cm in diameter.

The magnet is comprised of nine separate coils, seven primary coils and two shielding coils. The system has an inner bore diameter of 100.0 cm, an inner shield diameter of 180.0 cm, and its total length was 140.0 cm. This represents the configuration of a typical MR system today. Table 5.1 gives the positions and number of windings in each of the coils that make up the MR systems main magnet.

**Table 5.1:** The specifications for each coil in the 1.0 T main magnet, including their positions, the number of windings and the current.

Coil Number	Z position [m]	Number of windings	Current [A]
1	0	437	300
2	0.132	513	300
3	-0.132	513	300
4	0.306	806	300
5	-0.306	806	300
6	0.621	2080	300
7	-0.621	2080	300
8	0.550	1073	-300
9	-0.550	1073	-300

Next, a desired shield surface is then defined as a finite element mesh, which specifies the set of basis functions for the shield surface. A set of shield current density coefficients is then solved for over the shield mesh by minimizing the magnetic energy of the primary-shield system, just as was done in chapter 3. Figure 5.2 (a) shows one of the meshed shielding surfaces used in this study.

The mesh geometries were created in COMSOL Multiphysics<sup>®</sup> version 3.5a and then imported into MATLAB<sup>®</sup> version 7.11.0. The BE method was coded in an object-oriented class-based structure in MATLAB<sup>®</sup>. The current basis functions, resistance, inductance and field calculations were written in ANSI C. All computations were done on a 2.66 GHz iMac with 4 GB of RAM.

### 5.2.1 Static MR room

The first static shielding application was to place an active shield in the walls of the MR room for the purpose of reducing the stray field outside the MR room itself. In this case an MR room was modeled based on the minimum manufacture recommended room size for a commercial 3.0 T system (37). The MR room dimensions were 8.0 m long ( $z$ ) by 3.5 m wide ( $x$ ) by 3.0 m high ( $y$ ). To make the room more realistic a door was added along with a viewing window, filtration panel and finally a hole for the magnets quench pipe. The meshed shield surface and the room-system schematic can be seen in figures 5.2 (a) and 5.2 (b).

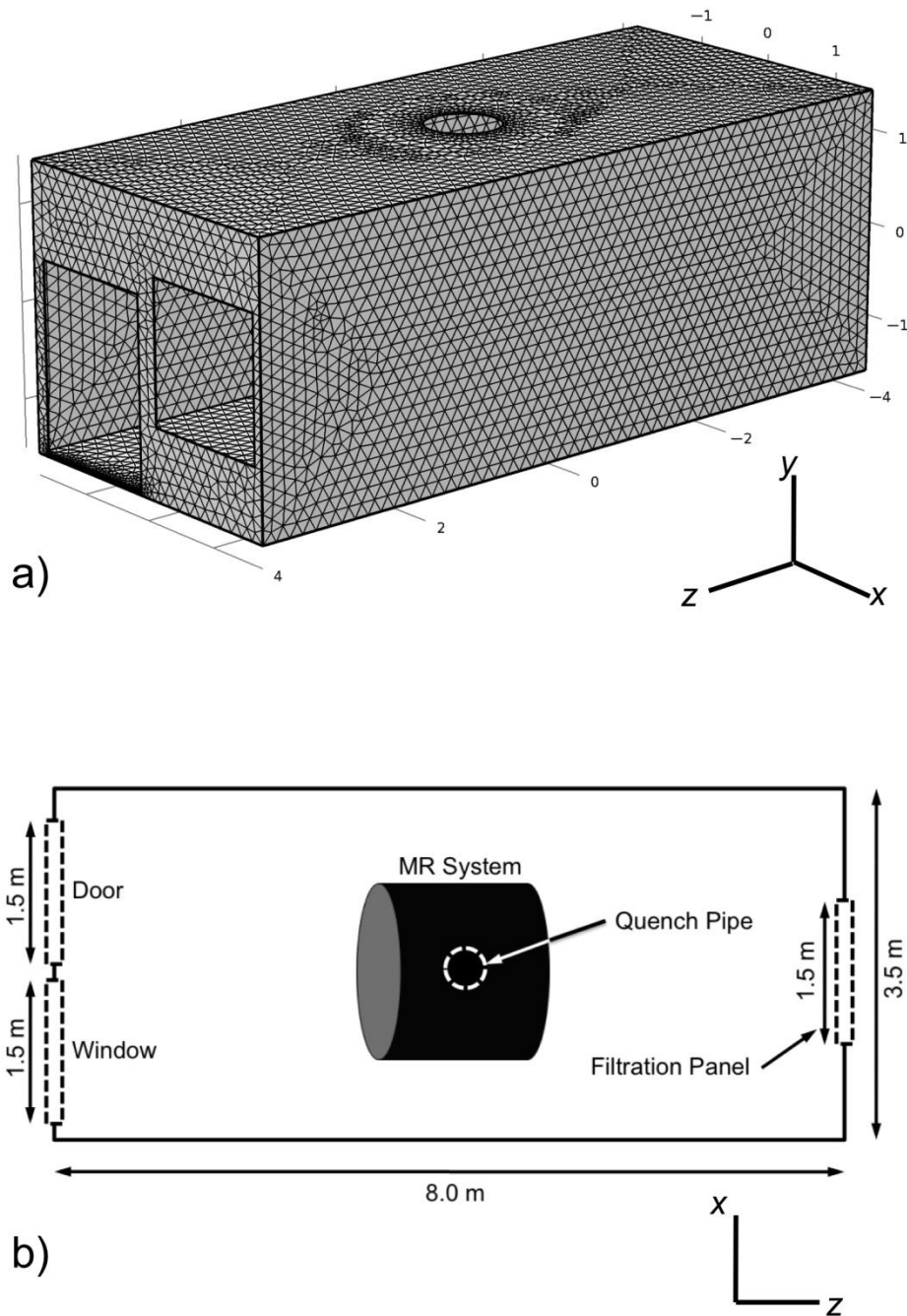


**Figure 5.2:** (a) shows the meshed shielding surface for the MR room shield. A viewing window (1.5 m by 1.5 m) and doorway (1.5 m by 2.0 m) are visible at the front, and not seen is a filtration panel (1.5 m by 1.5 m) on the back face. A 0.75 m diameter hole was cut in the roof to accommodate for a quench pipe. Figure 5.2 (b) is a schematic of the MR room and shows the positioning of the scanner. The isocenter of the magnet sits at the isocenter of the room, which means the magnet sits above the floor.

### 5.2.2 Static adjacent room

The second case addressed a shield in the walls of a room adjacent to the MR room for the purpose of reducing the field inside the adjacent room. The shield over the room's surface was calculated (such that it would be inserted into the walls of the room) for two separate cases: the case where the adjacent room is along the  $z$ -axis of the scanner, and the case where the adjacent room is located in the transverse ( $x$ ) direction. The room had dimensions 4.0 m long by 4.0 m wide by 3.0 m high and contained a 2.5 m tall by 2.0 m wide doorway. The meshed room surface is shown in figure 5.3 (a). The same room was used in both cases with the door position relative to the MR system shown in figures 5.3 (b) and 5.3 (c).

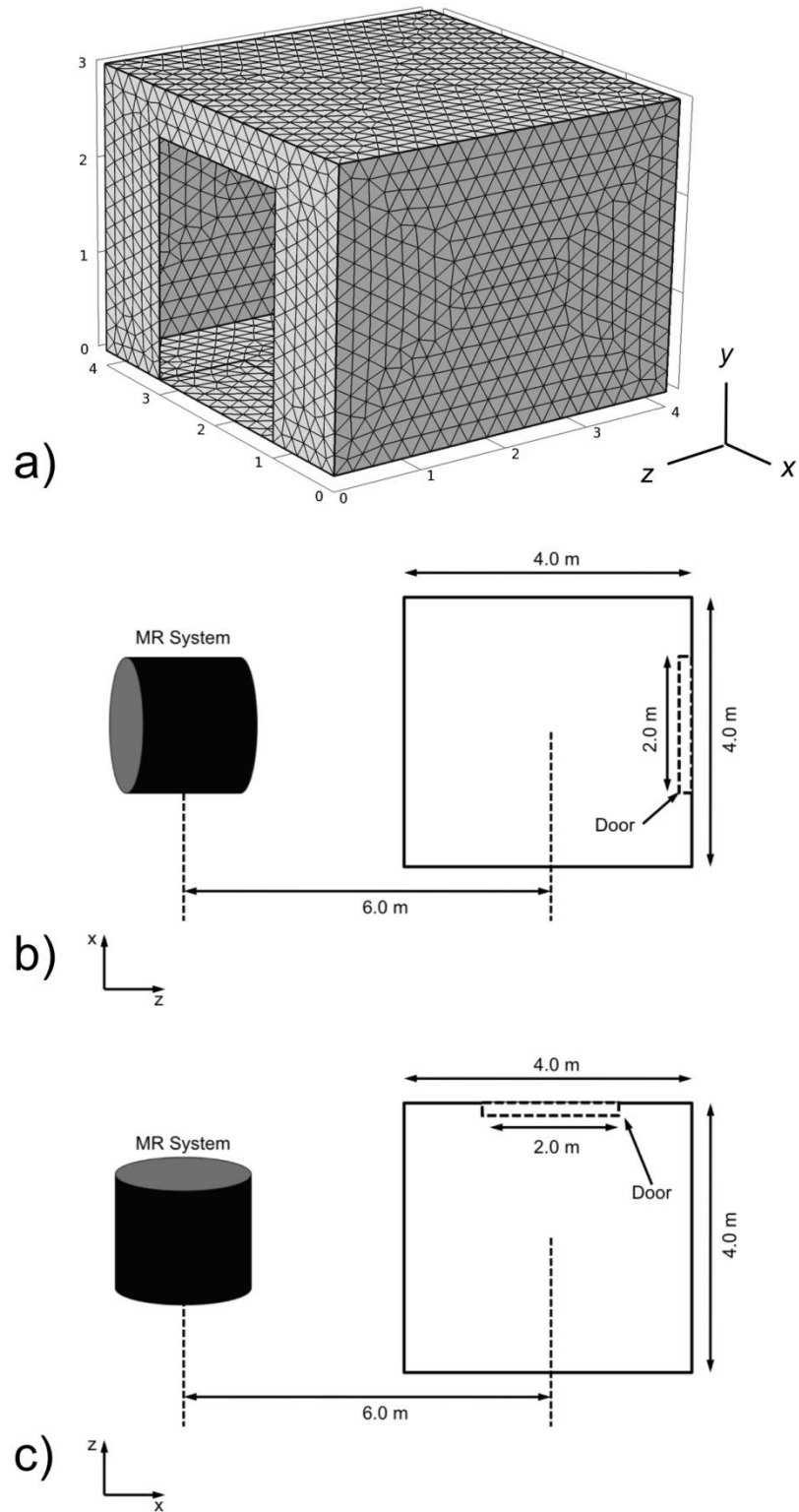


**Figure 5.3:** (a) displays the meshed surface used for the adjacent room case. The axes shown are for the situation where the room is located along the  $z$ -direction (axis of the scanner). Switching the  $x$ - and  $z$ -axes gives the transverse case. Figures 5.3 (b) and (c)



show schematics of the relative positions of the adjacent room and scanner for both cases examined. Both the magnets and rooms isocenters sit on the same horizontal plane.

### 5.2.3 Static equipment cabinet

The third static shield was that of a smaller shielded equipment cabinet inside the MR room. This case addressed the problem of housing non-MR compatible equipment in close proximity to the scanner. An example of the need for this can be found in (22). The cabinet had dimensions of 1.0 m by 1.0 m by 2.0 m tall. An opening 1.0 m tall by 0.5 m wide was cut into one side 0.75 m from the bottom of the cabinet. Figure 5.4 (a) shows the cabinet surface and figure 5.4 (b) shows the positioning relative to the MR system.

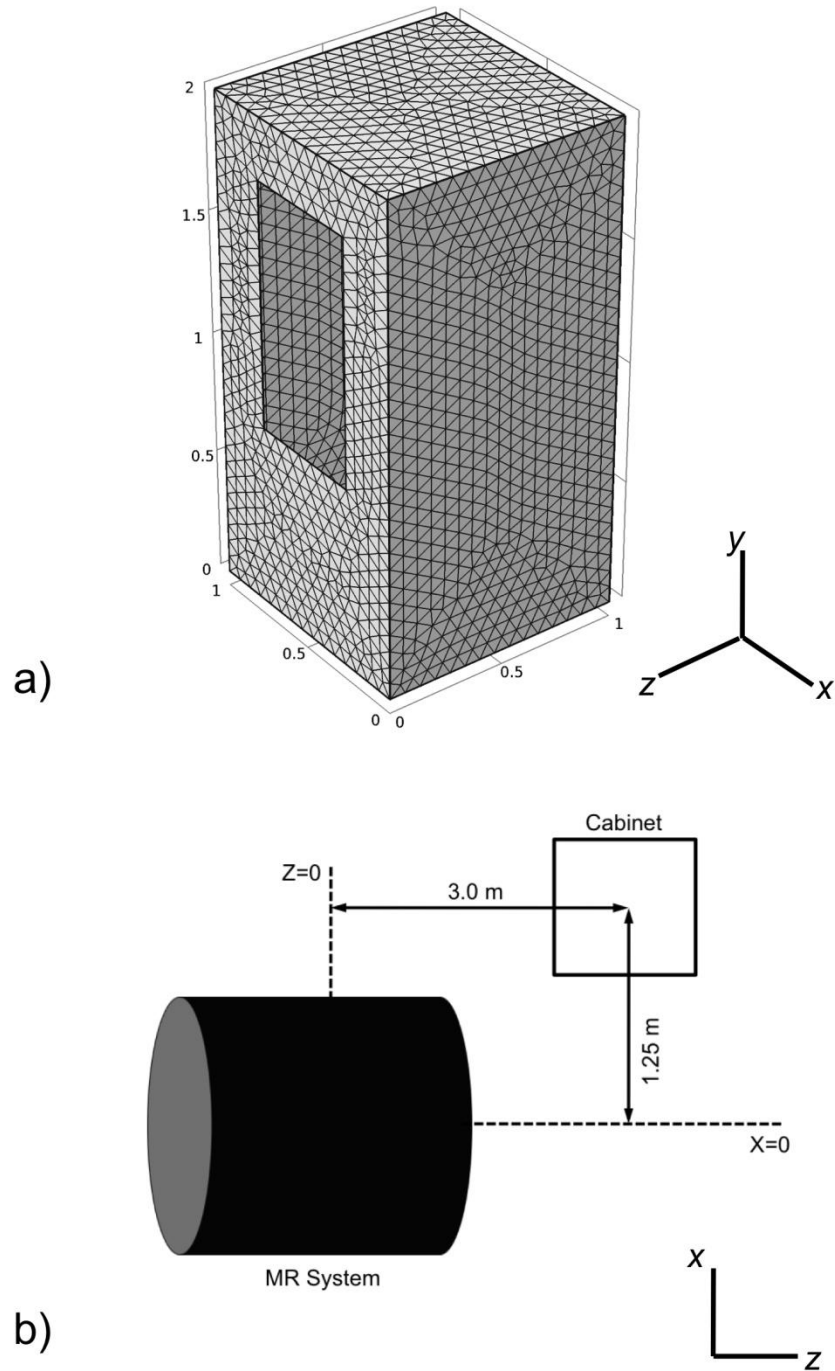


**Figure 5.4:** (a) is the meshed cabinet surface. Figure 5.4 (b) shows the positions of the MR scanner and the shielded cabinet in relation to one another. The cabinet was centered vertically with the MR system and the opening was located opposite the scanner on the face perpendicular to the  $z$ -axis.

### 5.2.4 Dynamic equipment cabinet

The second part of this study examined shielding applications in which either the MR system, or the shield, are in motion and the shielding current had to respond dynamically. The first case was that of a shielded cabinet inside the MR room that responded to an MR system moving in and out of the MR room along the  $z$ -axis. A moving superconducting MR system has many practical applications related to intraoperative MRI (38). The isocenter of the MR system in this simulation started 9.0 m away from the cabinet (along  $z$ ) and ended 3.0 m from the cabinet (along  $z$ ). The cabinet was offset 1.25 m in the  $x$ -direction with respect to the scanner and was centered vertically with the magnet. The minimum energy algorithm was used to find the shielding current density at two separate points along the MR systems path of motion. The first point was at 5.0 m where it was deemed that the magnetic field was beginning to be significant over the shielded region and the second point was the final position of the MR system (3.0 m away along  $z$ ). The cabinet itself consisted of two layers. The first layer had dimensions 1.0 m by 1.0 m in  $x$  and  $z$ , and 2.0 m along the  $y$ -direction and contained the shield calculated when the scanner was at  $z=3.0$  m (figure 5.4 (a), same as previous case) and the second layer had dimensions 1.01 m by 2.01 m by 1.01 m in  $x$ ,  $y$ , and  $z$  respectively, and housed the shield that was solved for when the MR system was at  $z=5.0$  m. The same opening as in the previous cabinet was cut through both layers.

### 5.2.5 Dynamic equipment cart

The second dynamic shield was a cart that could be moved around within the vicinity of the MR system, while adjusting for the changing magnetic field that it experiences. This cart had four separate shielding layers. The inner most layer had dimension 40.0 cm in  $x$  and  $z$  and 80.0 cm in  $y$ , and the outer most layer had dimensions 44.0 cm in  $x$  and  $z$  and 84.0 cm in  $y$ , with the two middle layers having 1.0 cm separation between them and the next layer on either side. Each shielding current density was solved for with the cart at  $x=0.64$  m and  $z=2.5$  m relative to the scanner isocenter with one of the four sides facing the scanner. The total shielding current density for an arbitrary cart position is just a weighted sum of the four separate current layers, where the current weights are solved for

by minimizing a functional containing target field points inside the shielded region of interest.

### 5.2.6 Performance calculations

The performance of each shield was calculated on a case specific basis. Because of the nature of these shields and the specific applications they are designed for, it does not make sense to use the 5.0 G line as a measure of shield effectiveness. Instead a more customized approach was used for each case. For the MR room shield the magnetic field was calculated over a rectangular surface of points (10.0 cm spacing between each point) 50.0 cm outside the walls of the room. The magnetic field values were plotted in a histogram and the root-mean-squared (rms) field values were calculated with and without the shield for comparison. For the adjacent room cases a similar procedure was followed. The field was calculated over a rectangular volume of points inside the rooms with 10.0 cm spacing between points in all directions. The grid points spanned the whole volume of the room to within 10.0 cm of the shield on each wall to avoid wire proximity effects. The field values were plotted in a histogram and rms values were calculated both before and after shielding cases. The effectiveness of the shielded cabinet was calculated the exact same way as the adjacent room shield, with the volume of grid points spanning the volume of the cabinet within 10.0 cm of each wall.

For the dynamic shields histograms of field magnitude and rms values were calculated at several different locations spanning the range of motion of the shield (or scanner) and the results are shown in the next section.

For all the shielding cases the change in the 1.0 % diameter spherical volume (DSV) was calculated as a measure of the effect the shield had on the imaging region of the scanner with and without each shield. To compliment this measure the magnetic field difference between unshielded and shielded was also calculated for each case at the isocenter of the main magnet.

For all shields the torques and forces were calculated directly from the simulated wire patterns using the Biot-Savart law. The resistances were calculated by assuming a

specific conductor material (copper) and conductor cross-sections based on the minimum wire separation for each case. The inductance was calculated via the Neumann formula, and power and stored energy were calculated from the resistance and inductance values generated for each shield.

## 5.3 Results

### 5.3.1 Static MR room

The full wire pattern for the MR room shield is shown in figure 5.5 and the wire patterns for each individual wall are shown in figure 5.6. Connection leads are not shown in any of the wire patterns and are not critical for magnetic field calculations. This shield was designed to operate at 300 A, which was chosen to give a buildable wire pattern based on minimum separation of wire spacing of 5.2 mm.

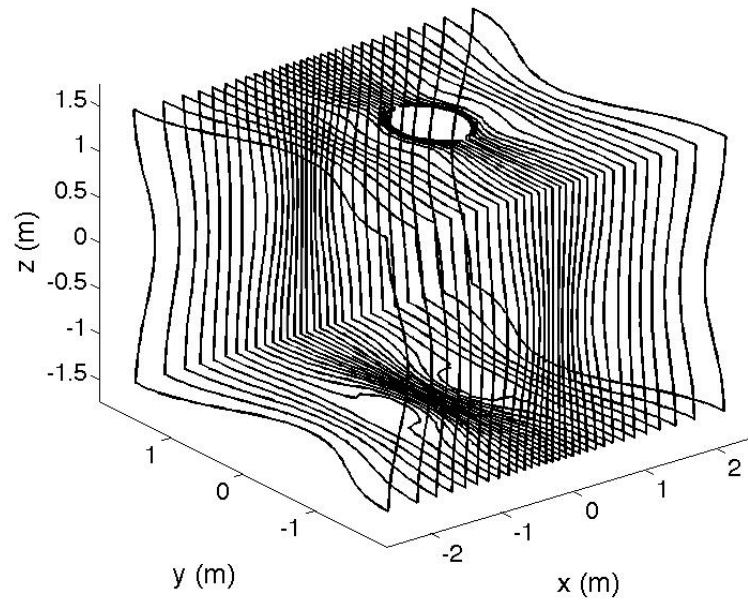


**Figure 5.5:** The wire pattern for the MR room shield with 80 % less wires for ease of visualization. Connection leads are not shown.

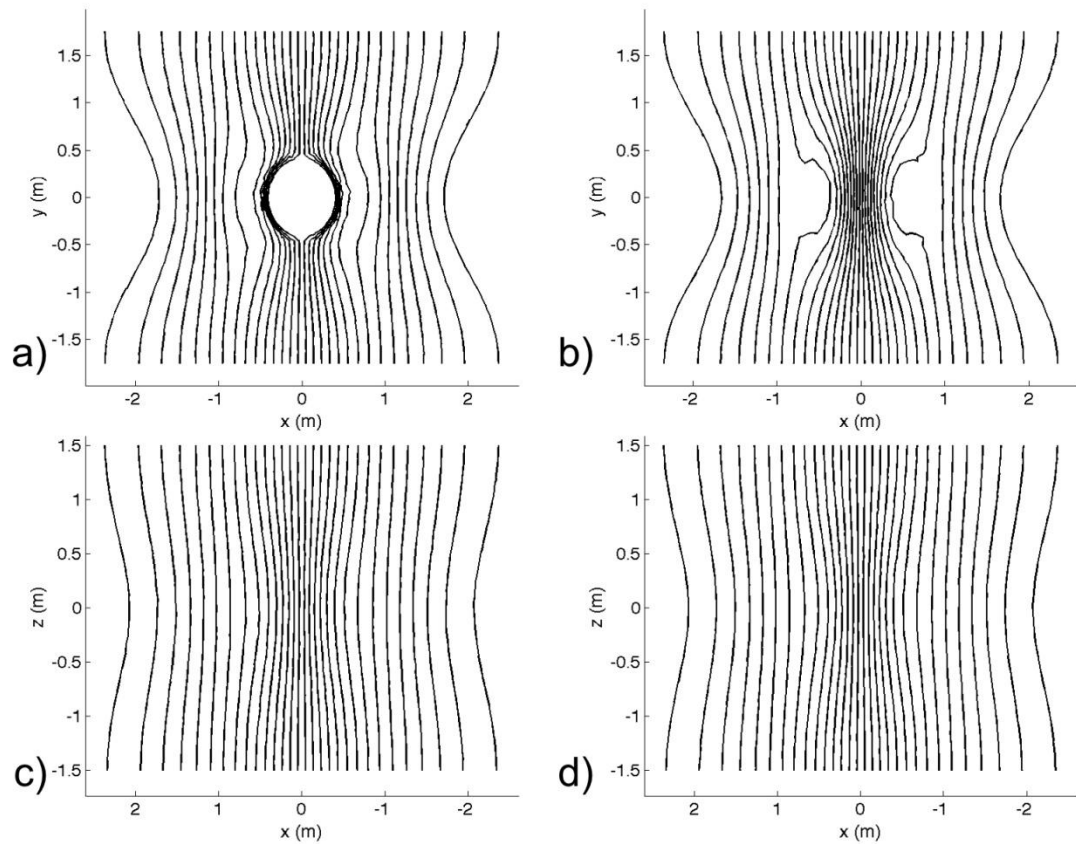


**Figure 5.6:** The conductor paths on each wall of the room, again with 80 % less windings. Note that two walls are not shown because they contain no current density. Connection leads are not shown.

The 0.5, 1, 5, 10 and 50 mT magnetic field lines with and without the shield in place are shown in figure 5.7 for the  $xy$ - and  $xz$ -planes. It can be seen from these plots that the presence of the room shield drastically reduces the stray field produced by the MR system.

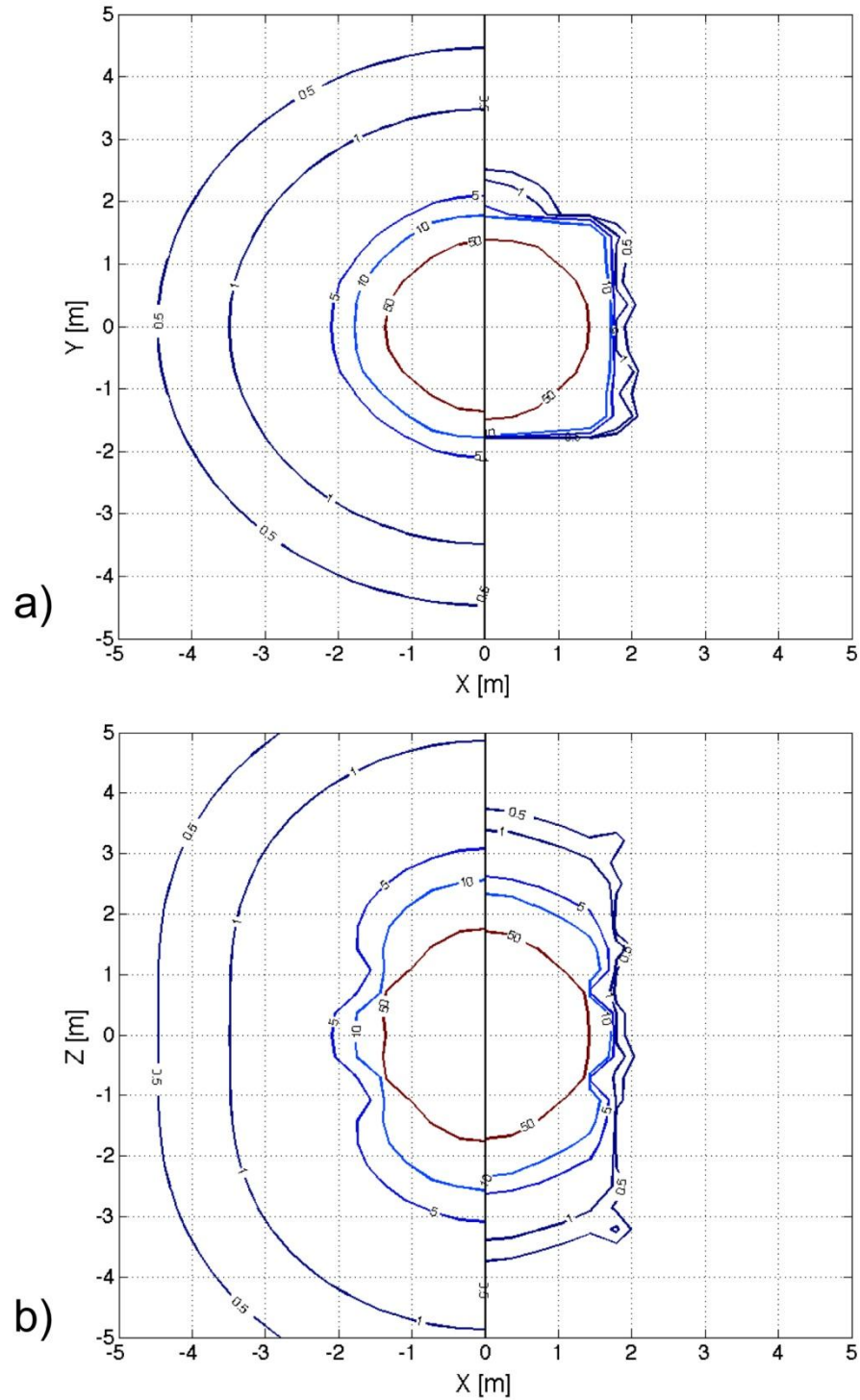


**Figure 5.7:** (a) is a plot of the 0.5, 1, 5, 10, and 50 mT magnetic field lines for the unshielded system (left side) versus the system plus the room shield (right side) on the  $xy$ -plane. Figure 5.7 (b) is the same plot over the  $xz$ -plane.

Table 5.2 shows the performance values of the room shield. The circuit parameters are given and the 1.0 % DSV is shown with and without the shielding, along with the rms field values calculated from the histograms shown in figures 5.8 (a) and 5.8 (b).

**Table 5.2:** The performance parameters for the MR room shield, including the circuit parameters, shielding performance metrics and effects on the imaging region.

Torque [Nm]	0.38
Force [N]	406
L [mH]	59.8
M [mH]	-60.0
R [ $\Omega$ ]	1.67
Current [A]	300
Power [kW]	150
Stored Energy [kJ]	2.69
1% DSV Before [cm]	35.73
1% DSV After [cm]	35.55
RMS Field Before [mT]	1.71
RMS Field After [mT]	0.10
$\Delta B$ at isocenter [mT]	2.1

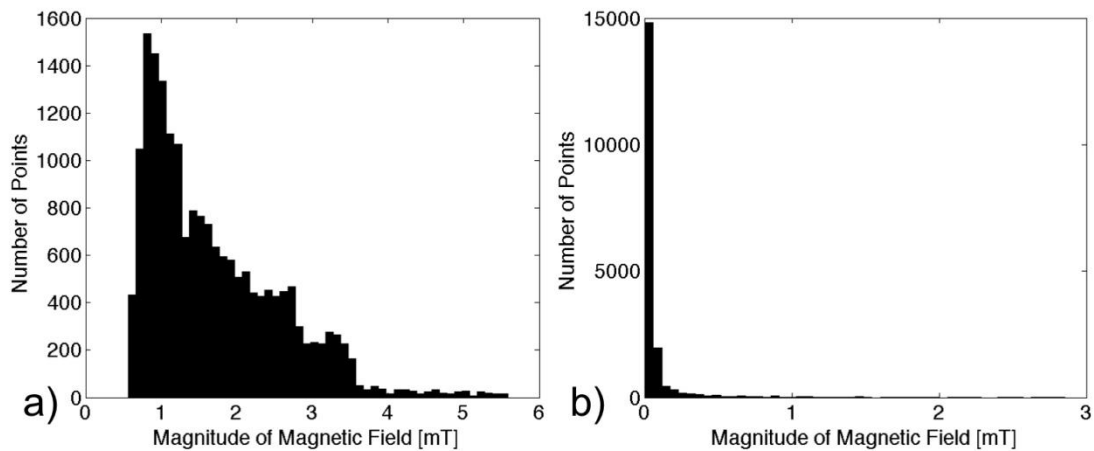
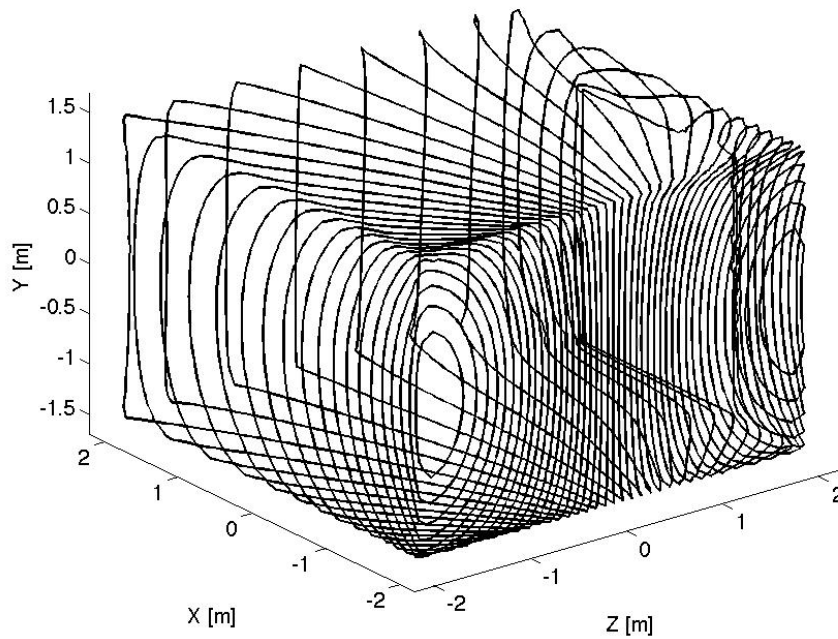


**Figure 5.8:** The field histograms over the rectangular surface 50.0 cm outside the MR room without (a) and with (b) the active room shield. Note the change in axis scale here.

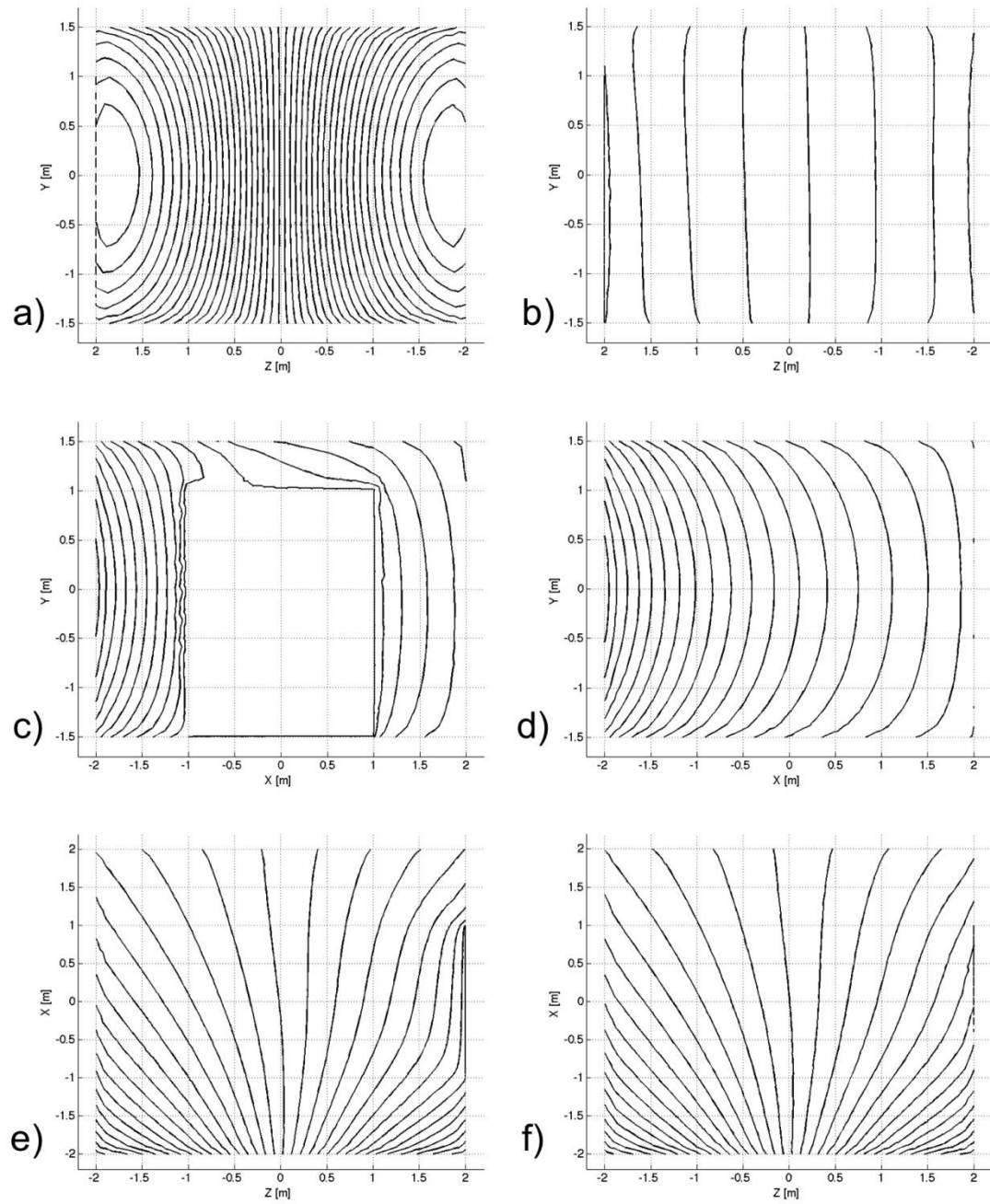


### 5.3.2 Static adjacent room

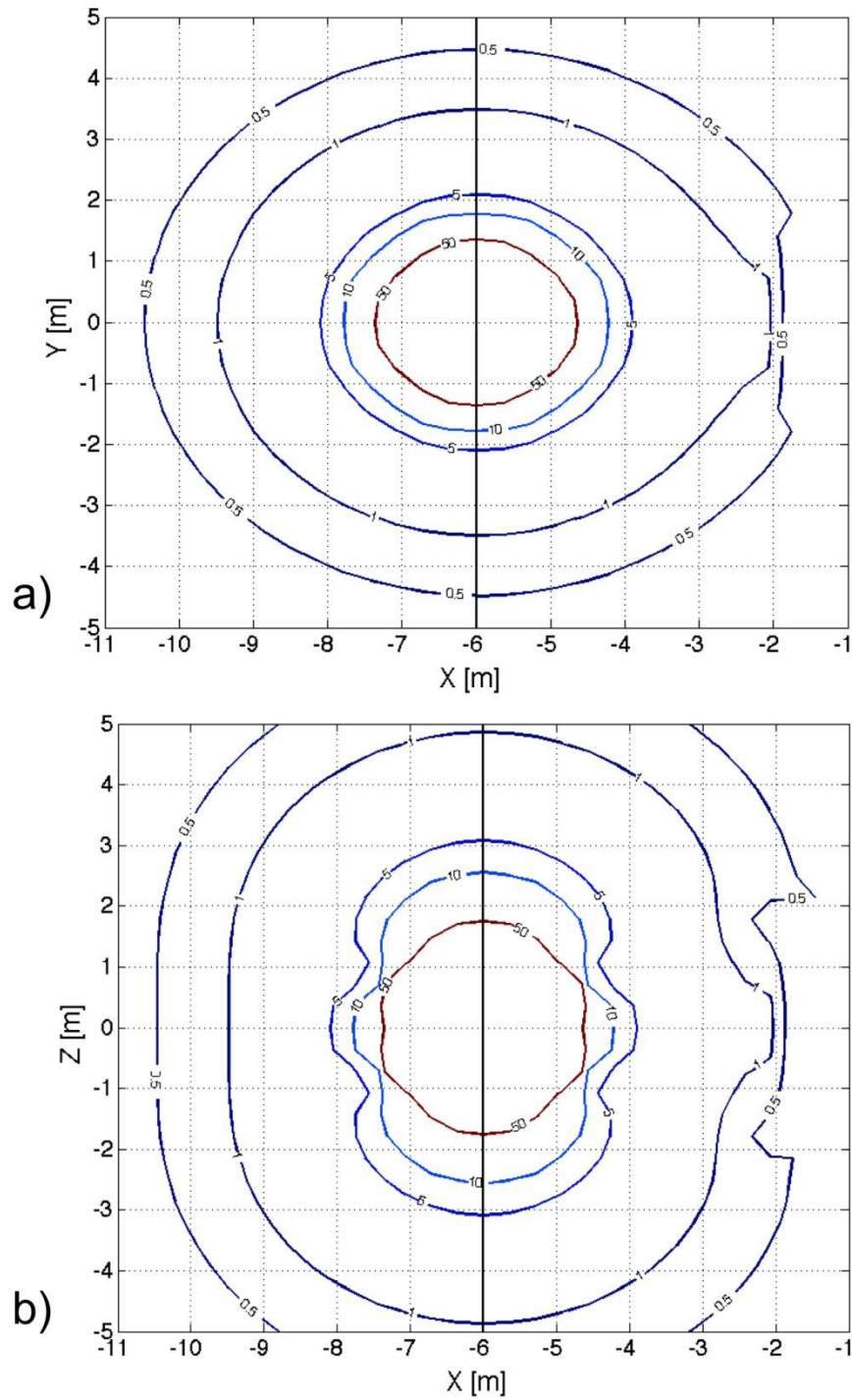
The full wire pattern for the shielded adjacent room located along the  $x$ -direction relative to the scanner is shown in figure 5.9. Figure 5.10 shows each individual wall of the room. The resulting magnetic field lines (0.5, 1, 5, 10, and 50 mT) are presented in figure 5.11 for the  $xy$ - and  $xz$ -planes.



**Figure 5.9:** The wire pattern of the room adjacent along the  $x$ -direction contoured such that it operates at 50.0 A. The connections leads are not shown.



**Figure 5.10:** The wire patterns on each of the individual walls of the room shown in figure 5.9 above. Connection leads are not shown.



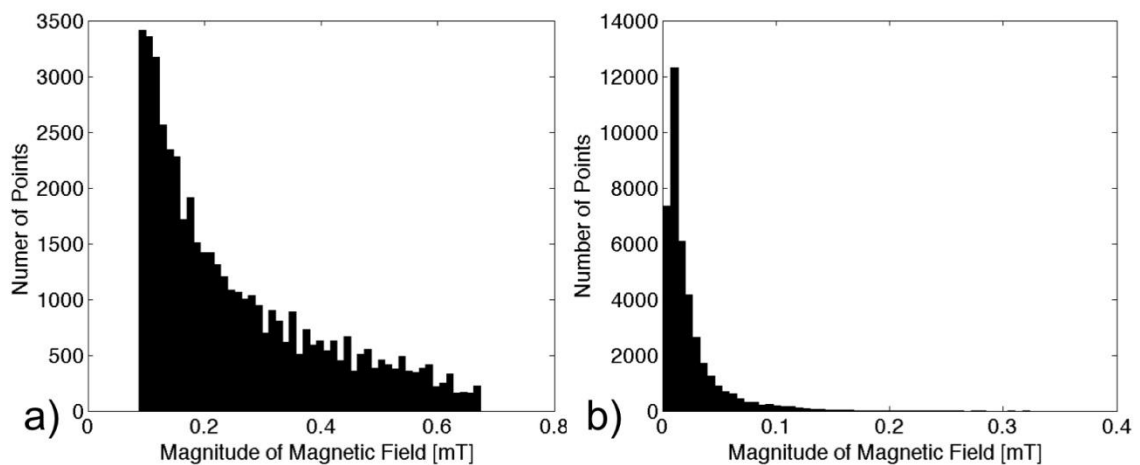
**Figure 5.11** The field lines for the MR system by itself (left side) and in the presence of the shielded room (right side) in the  $xy$ -plane (a) and  $xz$ -plane (b) for the transverse case.

Table 5.3 shows the performance values for each shield. The shields were designed to operate at 50.0 A, and this gave solutions that were very acceptable from a fabrication perspective, having a minimum wire separations of 9.7 mm for the transverse case and 9.0 mm for the longitudinal case.

**Table 5.3:** The performance parameters of both the adjacent room shields, including circuit parameters, shielding performance metrics, and the effects on the imaging region.

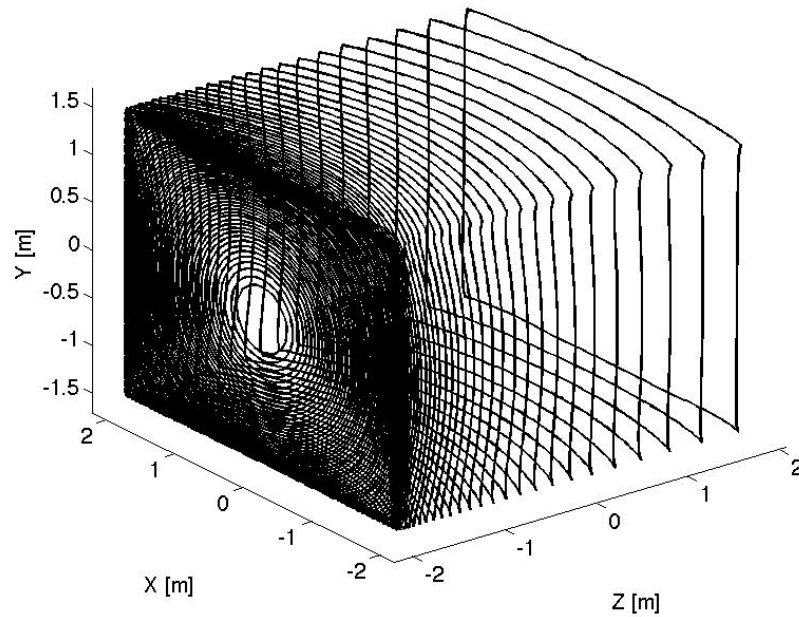
	Transverse	Longitudinal
Torque [Nm]	0.107	0.009
Force [N]	2.7	22.3
L [mH]	1.8	13.6
M [mH]	-0.3	-2.3
R [ $\Omega$ ]	0.33	0.68
Current [A]	50	50
Power [kW]	0.8	1.7
Stored Energy [J]	2.3	17.0
1 % DSV Before [%]	35.73	35.73
1 % DS* After [%]	35.72	35.71
RMS Field Before [mT]	0.26	0.56
RMS Field After [mT]	0.024	0.013
$\Delta B$ at isocenter [mT]	0.09	0.10

Figure 5.12 shows the histograms of the field magnitude over a volume enclosed by the room but not closer than 10.0 cm from any wall of the room. The histograms are shown for the cases: without and with active shielding.



**Figure 5.12:** The histograms of field magnitude over the volume enclosed by the rooms without (a) and with (b) shielding for the transverse case.

For the case where the room is adjacent along the  $z$ -axis the full wire pattern is shown in figure 5.13, and the individual wire patterns for each wall are shown in figure 5.14. It can be seen that the opposite wall containing the doorway does not contain any current.



**Figure 5.13:** The wire pattern for the room adjacent to the MR system along the  $z$ -direction. The doorway into the room is located on the back face. Connection leads are not shown.

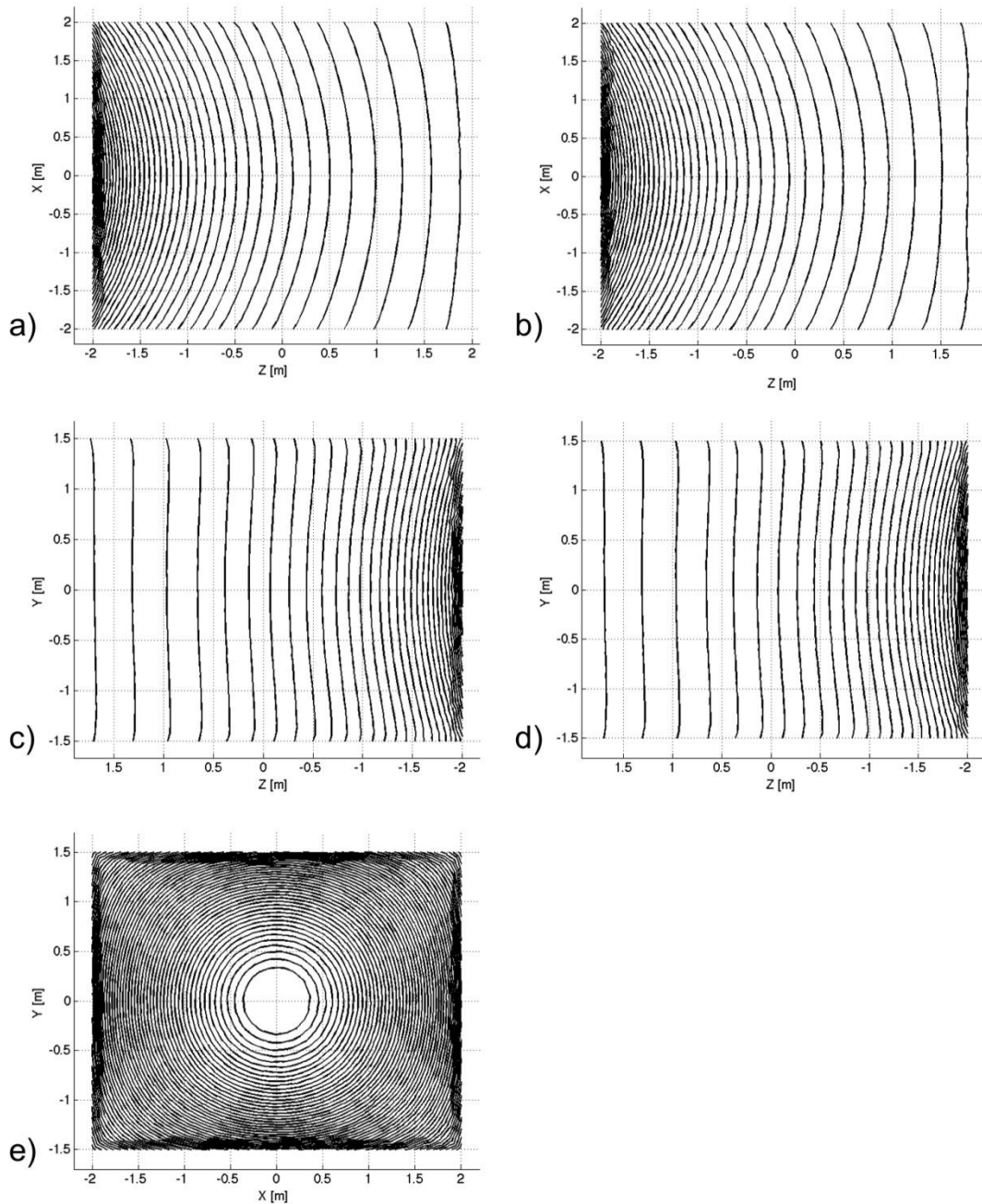


**Figure 5.14:** The wire patterns of each individual wall for the longitudinally adjacent shielded room. The wall furthest from the MR system, which contained the doorway, was omitted because it contained no wires. Connection leads are not shown.

The magnetic field profiles without and with the shield are shown in figure 5.15 for the  $xz$ - and  $yz$ -planes. The magnitude of the magnetic field was calculated over a volume enclosed by the room (10.0 cm away from each wall) and the resulting histograms are given in figure 5.16.

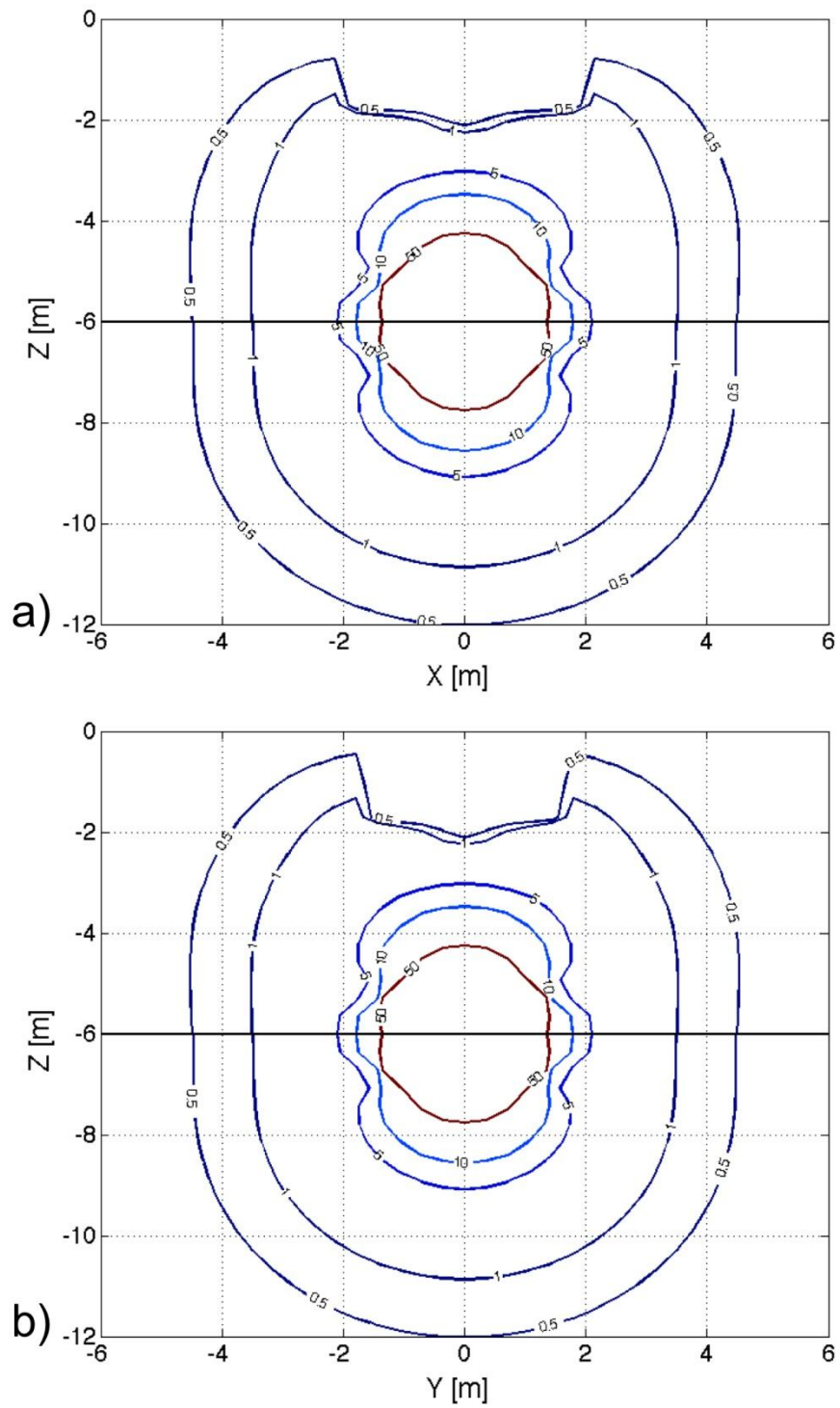


**Figure 5.15:** The 0.5, 1, 5, 10, and 50 mT field lines for the  $xz$ -plane (a) and the  $yz$ -plane (b) with (upper half) and without (lower half) shielding.

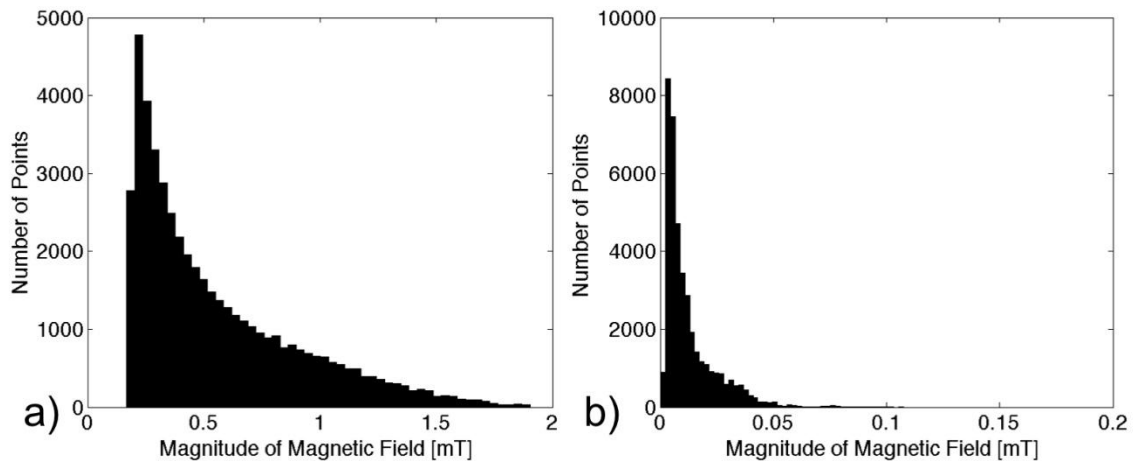


**Figure 5.16:** The histograms of field magnitude over the volume enclosed by the adjacent room without (a) the shield and with (b) the shield respectively. Note the scale change.

### 5.3.3 Static equipment cabinet

The full wire pattern for the shielded equipment cabinet is shown in figure 5.17 and the wire pattern on each face are shown in figure 5.17. This shield was designed to operate optimally at 50 A, and again, it was found that the wire spacing associated with 50 A was very suitable for fabrication purposes giving a 3.1 mm minimum wire spacing.

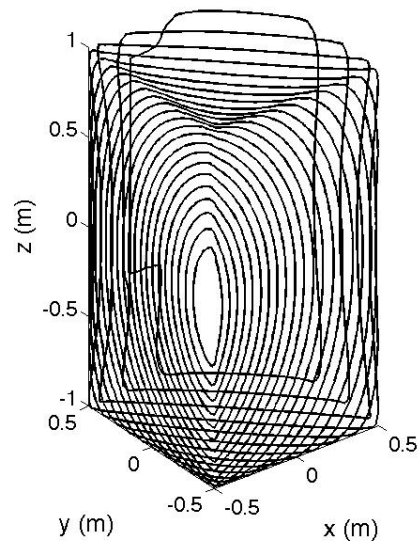


**Figure 5.17:** The wire pattern for the shielded cabinet with 80 % windings for ease of visualization. Connection leads not shown.



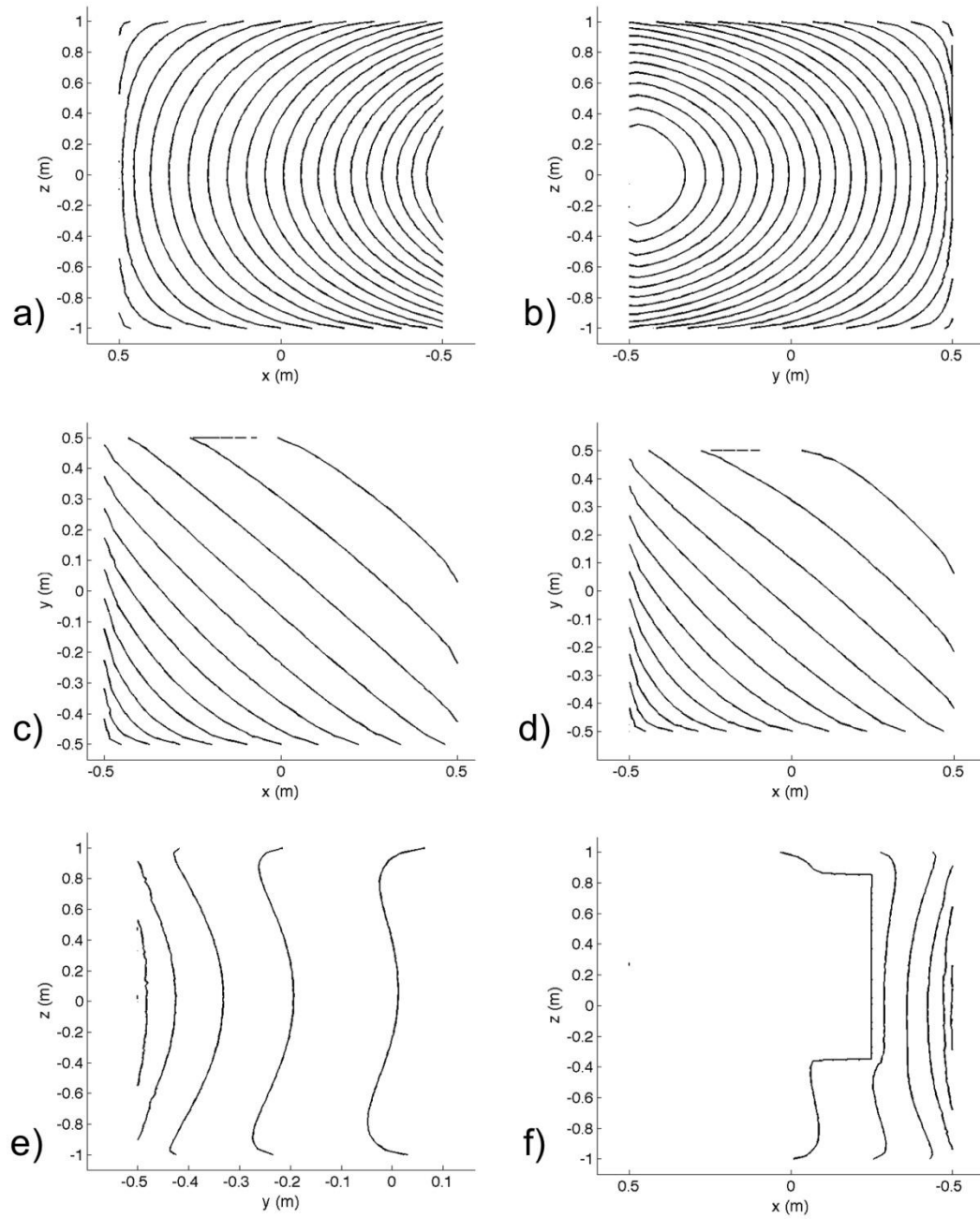


**Figure 5.18:** The individual wire patterns on each face of the cabinet with 80 % less wires for ease of visualization. The opening cut into the shield is noticeable in figure 5.18 (f).

The magnetic field lines (0.5, 1, 5, 10, and 50 mT) are shown in figure 5.19 and the circuit parameters and performance metrics for the shielded cabinet are given in table 5.4. The rms field values were calculated from the histograms shown in figure 5.20.

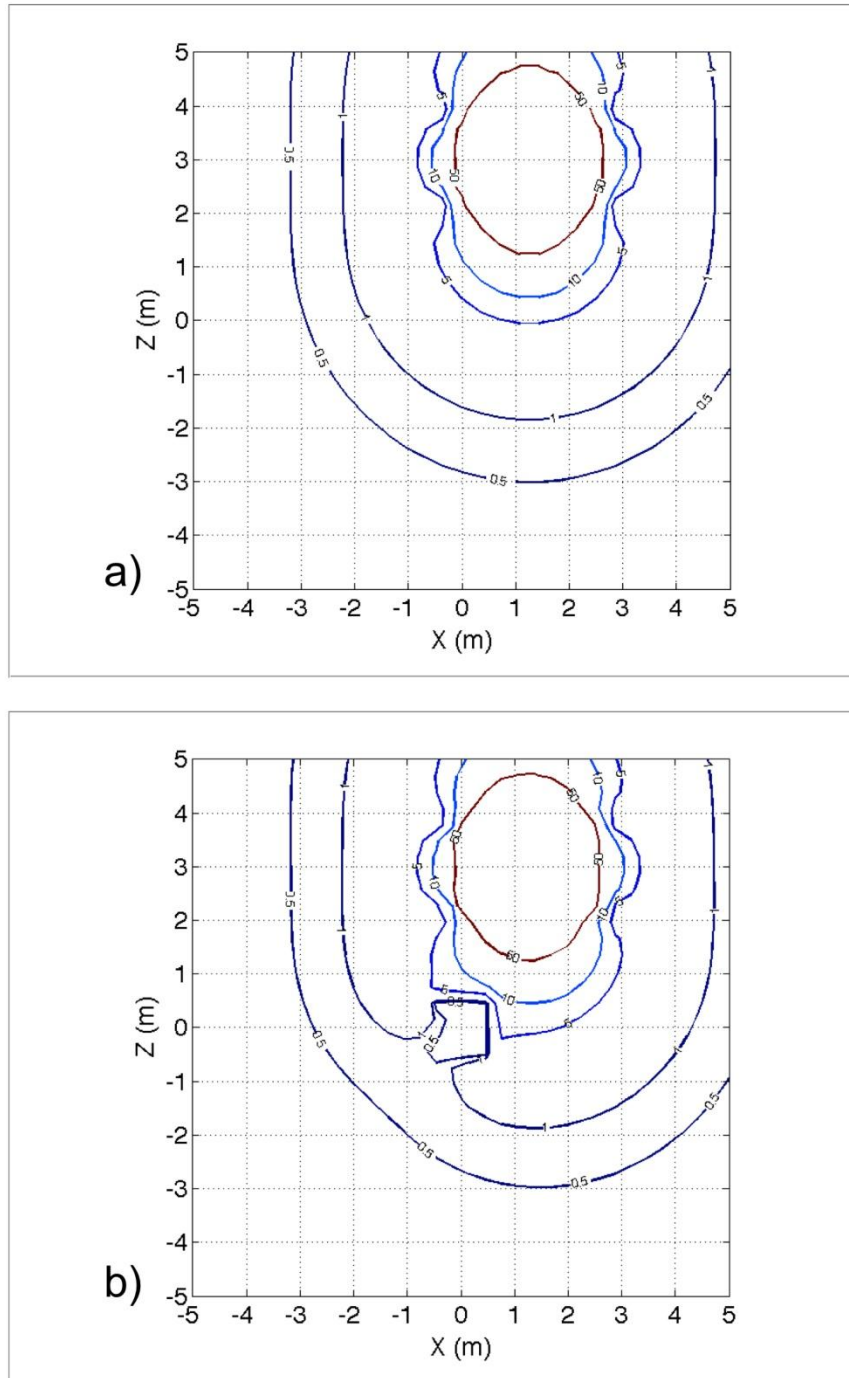


**Figure 5.19:** Plots of the magnetic field lines for the MR system and the MR system with the shielded cabinet present.

**Table 5.4:** The performance values for the shielded cabinet, including circuit parameters, shielding performance metric, and the effects on the imaging region.

Torque [Nm]	2.04
Force [N]	37.3
L [mH]	13.4
M [mH]	-2.3
R [ $\Omega$ ]	0.48
Current [A]	50
Power [kW]	1.21
Stored Energy [J]	16.8
1% DSV Before [cm]	35.73
1% DSV After [cm]	35.70
RMS Field Before [mT]	3.26
RMS Field After [mT]	0.10
$\Delta B$ at isocenter [mT]	0.11

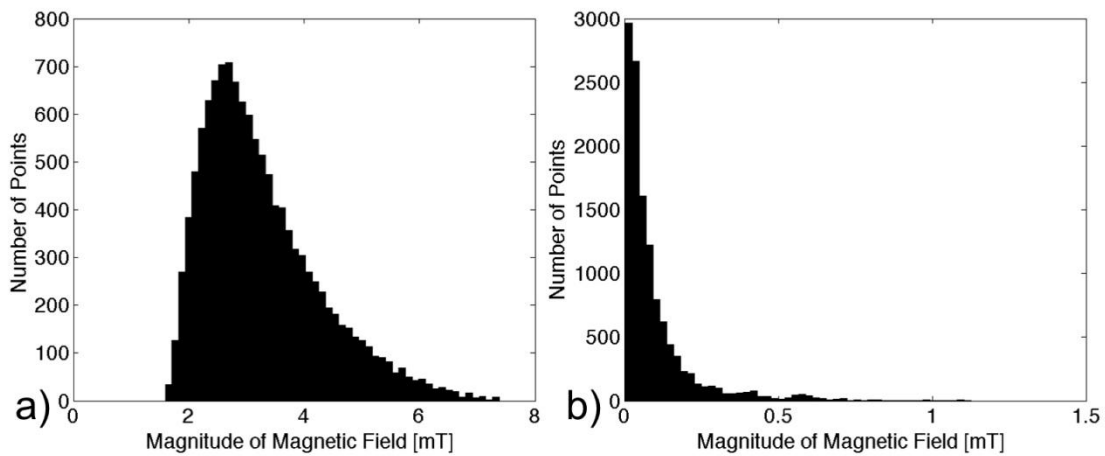


**Figure 5.20:** The magnetic field histograms without (a) and with (b) the shielded equipment cabinet.

### 5.3.4 Dynamic equipment cabinet

The wire patterns for this shielded cabinet are very similar to the static case previously shown, with the exception that the current density on the shield calculated at 5.0 m (along  $z$ ) away from the scanner is significantly lower amplitude. The optimal shielding current values were calculated for various positions relative to the MR system and are shown in table 5.5.

**Table 5.5:** The current values for each shield and the rms field values inside the cabinet for several different positions.

$z$ [m]	$i_1$ [A]	$i_2$ [A]	$B_{\text{rms}}$ Before [mT]	$B_{\text{rms}}$ After [mT]
5.0	-0.2	52.3	0.78	0.056
4.0	8.1	65.2	1.48	0.091
3.0	49.3	4.2	3.26	0.11

Magnetic field histograms are shown in figure 5.21 without and with the shield at 3.0, 4.0, and 5.0 m from the scanner along  $z$ .

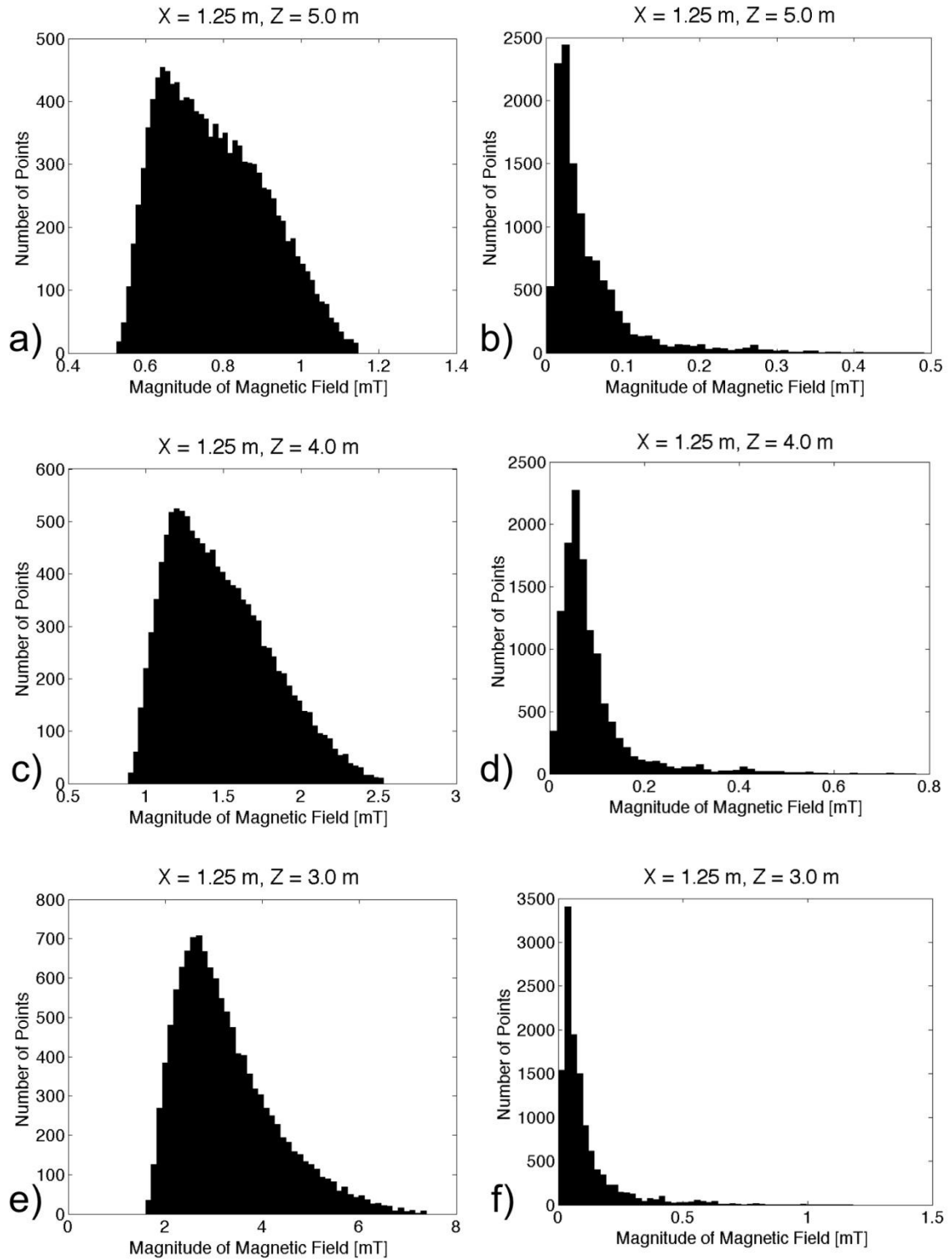


**Figure 5.21:** The magnetic field histograms calculated over a volume enclosed by the cabinet, but no closer than 5.0 cm to any inside wall.

### 5.3.5 Dynamic equipment cart

The currents in each shield of the shielded cart were calculated at various positions in the vicinity of the MR system. Both translational and rotational motion was used and the values are reported in table 5.6.

**Table 5.6:** The current values for all shields in the cart and the before and after rms field values inside the cart for various positions and orientations relative to the scanner.

$z$ [m]	$\phi$ [degrees]	$i_1$ [A]	$i_2$ [A]	$i_3$ [A]	$i_4$ [A]	$B_{rms}$ Before [mT]	$B_{rms}$ After [mT]
2.25	45	44.7	0	-7.6	39.1	12.47	8.43
2.25	30	52.8	0	-5.0	27.9	12.46	6.26
2.25	15	57.6	0	-5.1	16.1	12.47	4.06
2.25	0	57.9	7.5	-5.8	0	12.46	1.56
2.0	0	91.2	19.8	-3.0	0	18.75	2.56
1.75	0	143.8	48.7	0	0	29.79	5.24

For the various positions and orientations the magnetic field was calculated inside the shielded cart and the histograms, which are shown in figures 5.22 and 5.23, were plotted to highlight the shields effectiveness. It can be seen that despite the carts position or orientation it does in fact shield the enclosed volume. However, it can also be seen that the shielding ability of the cart is more dependent on its orientation than its proximity (to a point).

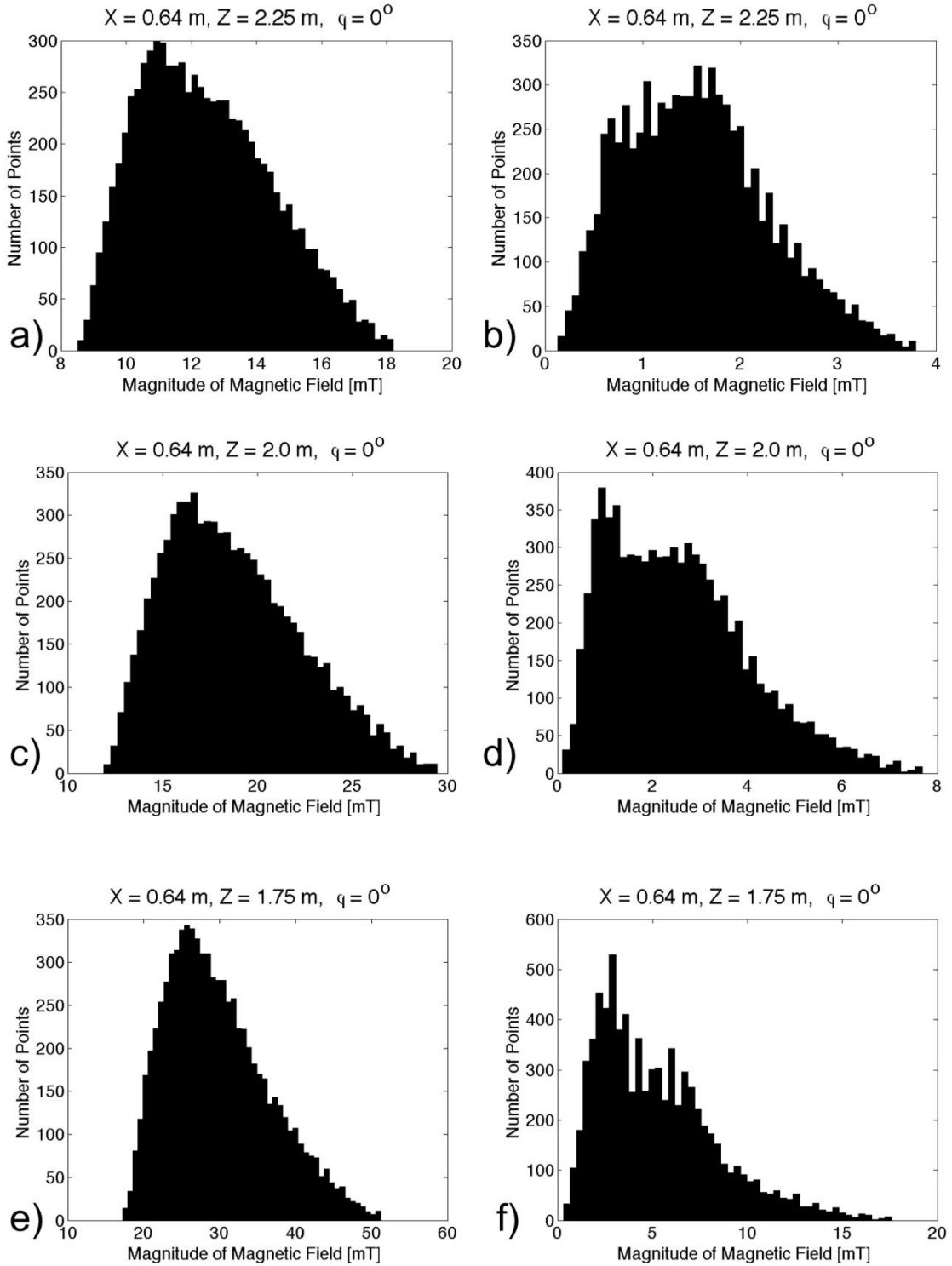


**Figure 5.22:** The histograms calculated at various translational positions (2.25 m, 2.00 m, and 1.75 m along  $z$ ) relative to the scanner.

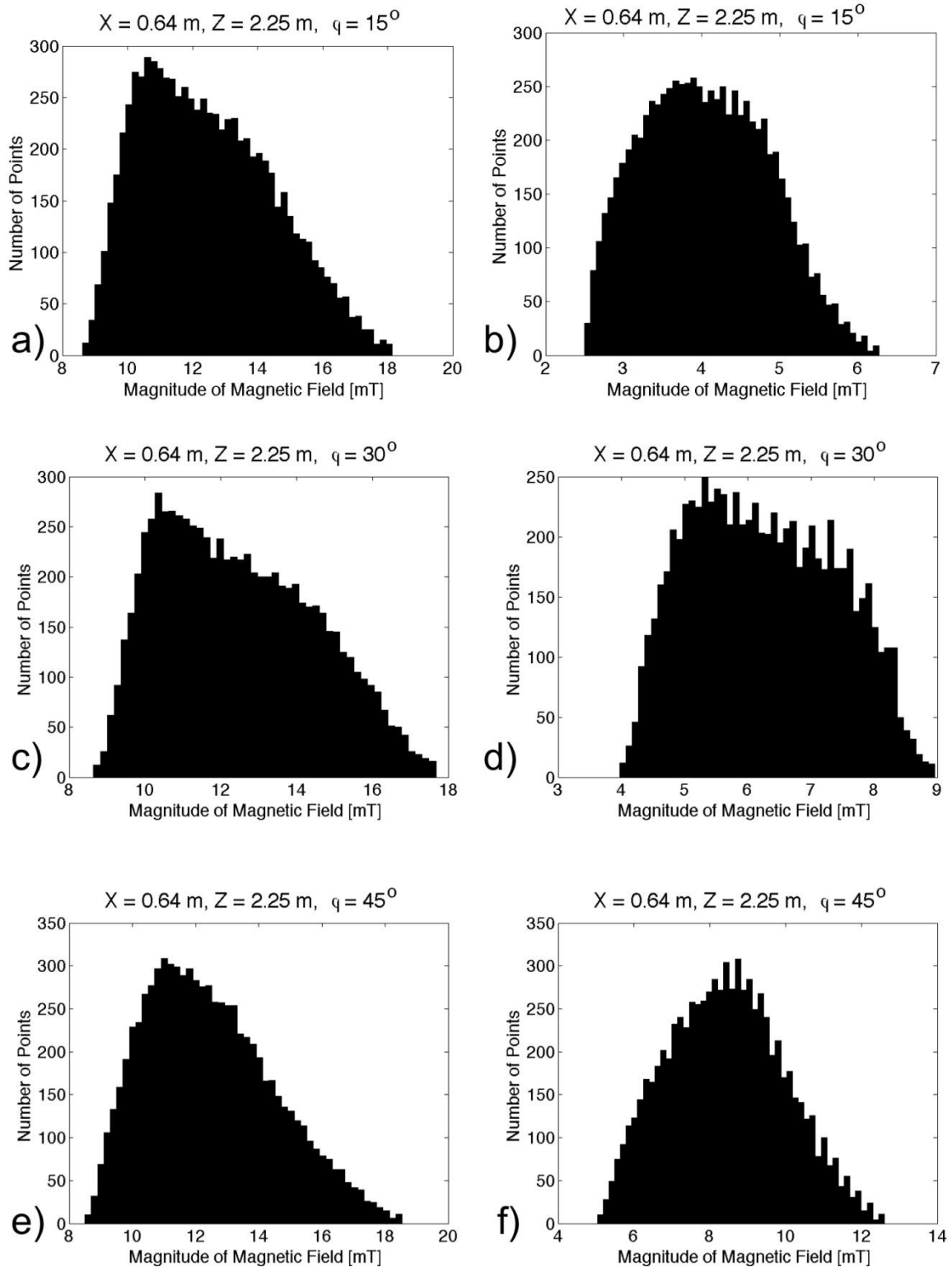


**Figure 5.23:** The magnetic field histograms for various orientations ( $15^\circ$ ,  $30^\circ$ , and  $45^\circ$ ) at the same position relative to the MR system.



## 5.4 Discussion

A minimum energy shielding algorithm has been used to examine several practical applications of active shielding with respect to the main field of an MR system.

For the case where an active shield was placed in the walls of the room that contained the MR system it was found that the fringe field could be greatly reduced outside the confines of the room. The rms field values calculated over a rectangular surface 50.0 cm from the room's surface before and after were 1.71 and 0.10 mT, suggesting an effective shield. However, in order to achieve a buildable solution a contour spacing equal to 300 A was necessary, making this shielding application rather impractical. At 300 A the power deposited would be ~150 kW, which necessitates a lot of liquid cooling. The cost to run such a device using recent and local (39) electricity costs would be on the order of \$9,600 per month. The material cost for such a shield considering only the cost of raw copper (40) would be approximately \$2,800. Note that this is not a build cost figure, just a raw conductor estimate. Overall the designed shield for this case works well from a theoretical standpoint, but is likely not feasible in practice given the power requirements and cost to run such a shield.

The adjacent room shields showed more promise. For both cases the magnetic field over the volumes of the rooms was drastically reduced. The average field values were reduced from 0.26 and 0.56 mT to 0.024 and 0.013 mT for the longitudinal and transverse cases respectively. To achieve buildable wire patterns a contour spacing equal to 50 A was sufficient, making these shield far more practical than the previous case. The total power required to run these shields was drastically less than the MR room shield at 1.69 and 0.83 kW for the longitudinal and transverses cases respectively. The copper costs of both shields were \$2,800 (longitudinal) and \$1,740 (transverse), estimated for 0 and 00 gauge copper wire, which corresponds to the largest diameters the minimum separations will allow. With the resistances given in Table 5.3 the electricity costs for both shields would be \$53 and \$108 per month, which means the costs associated with operation of these shields are likely not prohibitive.

The stationary shielded equipment cabinet reduced the average field from 3.26 to 0.099 mT over the volume inside the cabinet, while minimally affecting the imaging region of the system. The current in the cabinet shield was 50 A, which resulted in 1.21 kW of total power. The cost to build this shield using only copper as an input is approximately \$197 and the cost to drive it at current hydro rates would be approximately \$77 per month. The feasibility of this type of shield depends highly on the positioning relative to the MR system, which will be discussed with the case of the dynamic equipment cabinet.

The dynamic equipment cabinet was just an extension of the stationary case to address the situation where an MR system is actually moved in and out of operating room that houses non-compatible MR equipment. Significant rms field reductions were achieved for the range of motion reported. However, it was found that bringing the scanner and cabinet within approximately 2.0 m of each other (center to center) resulted in current requirements of over 200 A to maintain a respectable level of shielding, which is not practical given the wire spacing of these shields. The copper cost for both layers together was \$244, and the power required to drive the shields was dependent on the cabinet's proximity to the scanner. In practice this case is certainly possible, but proximity limits do exist.

The last case examined was the of a smaller shielded equipment cart that could move around in the vicinity of the MR system and respond to the changing field it experienced. Four separate shielding layers were required in order to allow for field cancellation in any upright orientation. The shields were effective at reducing the field inside the cart, as evidenced by figures 5.21 and 5.22. Again it can be noted that the effectiveness and feasibility of this types of shield is dependent of the required proximity from the scanner. At distances approaching 1.75 m from the center of the MR system currents of approximately 150 A or greater were required. An interesting point to address for this and the previous case is that of eddy current generation due to the changing flux through these shields. As they are brought closer to the MR system eddy currents will build to oppose the changing flux. This could possibly aid in ramping the current in the

shield, but it will also result in forces that oppose the motion of the shield (to the point where a person cannot physically push the shield any closer to the system).

For completeness it is constructive to examine a situation where one of these shields could be used in practice. Consider the desirable situation where a PET system is located in a room adjacent (longitudinally) to a 1.5 T shielded clinical MR system at a distance of 6.0 m isocenter to isocenter, which corresponds to the MR room and adjacent room dimensions used above. Given the tolerances on PET electronics reported by Bindseil *et al.* (41) the normalized efficiency of the PET system would be reduced from 1.0 to 0.927 as a result of a 0.84 mT average stray field from the 1.5 T MR system. This amount is significant, as it means the PET system needs to undergo significant recalibration. However, if the shield calculated above is present the average field over the volume of the room is 0.29 mT, which results in an efficiency of 0.989, meaning no recalibrations are required for imaging with the PET system at all.

Aside from build and power costs, other practical issues deserve mention. Temporal stability is a major issue in MR and could pose a serious problem as the temporal stability of resistive magnets is significantly worse than that of superconducting magnets. Also of issue is the stability of commercial amplifiers. A typical commercial gradient amplifier has current noise of approximately 250  $\mu\text{A}$ . A current stability such as this, would result in a 0.0005 ppm drift at the center of the magnet for the case of longitudinally adjacent room shield. Clinical MR systems require stabilities on the order of 0.1 ppm/hour – meaning the stability of these shields would be quite acceptable. The fact that these shields produce much smaller fields than the MR system more than compensates for their reduced stability.

Failure risks are also an interesting point of discussion. The shields in this work have been discussed in the context of both siting safety and siting compatibility. Perhaps only the later would be possible given that these shields could fail due to either malfunction or loss of power. Consider the PET system example outlined above; a failure of the shield would only result in poor PET data provided a scan was in progress during the shield failure. However, if a shield is constructed for safety purposes, such as shielding patient

care equipment during intraoperative MR procedures, and a failure occurs, the result could be a malfunction in critical patient care equipment. This could be devastating. Ultimately the specific application would dictate the seriousness of a shield malfunction.

## 5.5 References

1. Gilbert KM, Handler WB, Scholl TJ, Odegaard JW, Chronik BA. 2006 Design of field-cycled magnetic resonance systems for small animal imaging. *Physics in Medicine and Biology*;51(11):2825-2841.
2. Matter NI, Scott GC, Grafendorfer T, Macovski A, Conolly SM. 2006 Rapid polarizing field cycling in magnetic resonance imaging. *Ieee Transactions on Medical Imaging*;25(1):84-93.
3. Chronik BA, Rutt BK. 2001 Simple linear formulation for magnetostimulation specific to MRI gradient coils. *Magnetic Resonance in Medicine*;45(5):916-919.
4. Chronik BA, Rutt BK. 2001 A comparison between human magnetostimulation thresholds in whole-body and head/neck gradient coils. *Magnetic Resonance in Medicine*;46(2):386-394.
5. Collins CM, Li SZ, Smith MB. 1998 SAR and B-1 field distributions in a heterogeneous human head model within a birdcage coil. *Magnetic Resonance in Medicine*;40(6):847-856.
6. Lattanzi R, Sodickson DK, Grant AK, Zhu YD. 2009 Electrodynamic Constraints on Homogeneity and Radiofrequency Power Deposition in Multiple Coil Excitations. *Magnetic Resonance in Medicine*;61(2):315-334.
7. Schenck JF. 2000 Safety of strong, static magnetic fields. *Journal of Magnetic Resonance Imaging*;12(1):2-19.
8. Crozier S, Trakic A, Wang H, Liu F. 2007 Numerical study of currents in workers induced by body-motion around high-ultrahigh field MRI magnets. *Journal of Magnetic Resonance Imaging*;26(5):1261-1277.
9. Trakic A, Wang H, Liu F, Lopez HS, Weber E, Crozier S. 2008 Minimizing the induced fields in MRI occupational workers by lowering the imager. *Concepts in Magnetic Resonance Part B-Magnetic Resonance Engineering*;33B(1):39-54.
10. Ho HS. 2001 Safety of metallic implants in magnetic resonance imaging. *Journal of Magnetic Resonance Imaging*;14(4):472-477.
11. Nyenhuis JA, Park SM, Kamondetdacha R, Amjad A, Shellock FG, Rezai AR. 2005 MRI and implanted medical devices: Basic interactions with an emphasis on heating. *Ieee Transactions on Device and Materials Reliability*;5(3):467-480.
12. Achenbach S, Moshage W, Diem B, Bieberle T, Schibgilla V, Bachmann K. 1997 Effects of magnetic resonance Imaging on cardiac pacemakers and electrodes. *American Heart Journal*;134(3):467-473.

13. Martin ET, Coman JA, Shellock FG, Pulling CC, Fair R, Jenkins K. 2004 Magnetic resonance imaging and cardiac pacemaker safety at 1.5-Tesla. *Journal of the American College of Cardiology*;43(7):1315-1324.
14. Graf H, Lauer UA, Schick F. 2006 Eddy-current induction in extended metallic parts as a source of considerable torsional moment. *Journal of Magnetic Resonance Imaging*;23(4):585-590.
15. Schueler BA, Parrish TB, Lin JC, Hammer BE, Pangrle BJ, Ritenour ER, Kucharczyk J, Truwit CL. 1999 MRI compatibility and visibility assessment of implantable medical devices. *Journal of Magnetic Resonance Imaging*;9(4):596-603.
16. Kangarlu A, Robitaille PML. 2000 Biological effects and health implications in magnetic resonance imaging. *Concepts in Magnetic Resonance*;12(5):321-359.
17. Barnett GH, Ropper AH, Johnson KA. 1988 Physiological Support and Monitoring of Critically Ill Patients during Magnetic-Resonance Imaging. *Journal of Neurosurgery*;68(2):246-250.
18. Jekic M, Ding Y, Dzwonczyk R, Burns P, Raman SV, Simonetti OP. 2010 Magnetic Field Threshold for Accurate Electrocardiography in the MRI Environment. *Magnetic Resonance in Medicine*;64(6):1586-1591.
19. Pichler BJ, Judenhofer MS, Wehrl HF. 2008 PET/MRI hybrid imaging: devices and initial results. *European Radiology*;18(6):1077-1086.
20. Bindseil G. 2010 Active magnetic shielding of PET detectors for a small-animal multimodality PET/MRI system. *J Nucl Med Meeting Abstracts*;51:412.
21. Lagendijk JJW, Raaymakers BW, Raaijmakers AJE, Overweg J, Brown KJ, Kerkhof EM, van der Put RW, Hardemark B, van Vutpen M, van der Heide UA. 2008 MRI/linac integration. *Radiotherapy and Oncology*;86(1):25-29.
22. Kettenbach J, Kacher DF, Kanan AR, Rostenberg B, Fairhurst J, Stadler A, Kienreich K, Jolesz FA. 2006 Intraoperative and interventional MRI: Recommendations for a safe environment. *Minimally Invasive Therapy & Allied Technologies*;15(2):53-64.
23. Silverman SG, Jolesz FA, Newman RW, Morrison PR, Kanan AR, Kikinis R, Schwartz RB, Hsu LG, Koran SJ, Topulos GP. 1997 Design and implementation of an interventional MR imaging suite. *American Journal of Roentgenology*;168(6):1465-1471.
24. Morad R, Palkovich A. 1988 The Design and Use of Secondary Shielding in Mri Systems - Experience from 4 Years of Operation. *Ieee Transactions on Magnetics*;24(2):1288-1291.

25. Kalafala AK. 1993 Optimized Configurations for Passively Shielded Magnetic-Resonance-Imaging Magnets. *Ieee Transactions on Magnetics*;29(2):1240-1244.
26. Noguchi S, Ishiyama A. 1997 Optimal design method for MRI superconducting magnets with ferromagnetic shield. *Ieee Transactions on Magnetics*;33(2):1904-1907.
27. Price T. 2010 A case study on the influence of a magnetic shielding retrofit on the static magnetic field present in a Magnetic Resonance Imaging (MRI) suite. *Safety Science*;48(10):1498-1515.
28. Cho ZH, Son YD, Kim HK, Kim KN, Oh SH, Han JY, Hong IK, Kim YB. 2007 A hybrid PET-MRI: An integrated molecular-genetic imaging system with HRRT-PET and 7.0-T MRI. *International Journal of Imaging Systems and Technology*;17(4):252-265.
29. Davies FJ, Elliott RT, Hawksworth DG. 1991 A 2-Tesla Active Shield Magnet for Whole-Body Imaging and Spectroscopy. *Ieee Transactions on Magnetics*;27(2):1677-1680.
30. Hirosato S, Yamazaki K, Muramatsu K, Hirayama M, Haga A, Katada K. 2006 Open type of magnetically shielded room combined with cancelling coil for magnetic resonance imaging. *Ieee Transactions on Magnetics*;42(10):3542-3544.
31. Yamazaki K, Hirosato S, Muramatu K, Hirayama M, Kamata K, Onoki T, Kobayashi K, Haga A, Katada K, Kinomura Y and others. 2007 Open-type magnetically shielded room using only canceling coil without a ferromagnetic wall for magnetic resonance imaging. *Ieee Transactions on Magnetics*;43(6):2480-2482.
32. Haw DW, Harris CT, Handler WB, Chronik BA. 2011 A minimum energy method for the design of shielding coils over arbitrary geometries. *Phys Med Biol*. (*Submitted*)
33. Pissanetzky S. 1992 Minimum Energy Mri Gradient Coils of General Geometry. *Measurement Science & Technology*;3(7):667-673.
34. Lemdiasov RA, Ludwig R. 2005 A stream function method for gradient coil design. *Concepts in Magnetic Resonance Part B-Magnetic Resonance Engineering*;26B(1):67-80.
35. Poole M, Bowtell R. 2007 Novel gradient coils designed using a boundary element method. *Concepts in Magnetic Resonance Part B-Magnetic Resonance Engineering*;31B(3):162-175.
36. Xu H, Conolly SM, Scott GC, Macovski A. 2000 Homogeneous magnet design using linear programming. *Ieee Transactions on Magnetics*;36(2):476-483.

37. Siemens Medical Solutions. MAGNETOM Trio 3 T specification sheet. Siemens Incorporated; 2011.
38. IMRIS. IMRIS neurosurgical solutions. IMRIS Incorporated; 2011.
39. OEB. Delivery Rates and Electricity Prices. Hydro One Inc.; 2011.
40. CME. Copper Futures. Chicago: CME Group; 2011.
41. Bindseil G, Handler WB, Scholl TJ, Chronik BA. Magnetic field exposure tests on a Siemens small animal PET system: a feasibility study for multimodality PET and field-cycled MRI. 2010; Stockholm, Sweden.



## Chapter 6

### 6 Discussions and future work

#### 6.1 Thesis summary

In Chapter 2 of this work the effects of construction tolerances on shielded gradient coils was examined. A customized gradient insert coil with transverse and longitudinal shielded gradients was constructed such that the shields could be deliberately misaligned with respect to the primary coils. The inductance was measured for both axes as a function of shield position on the bench, and a significant increase was seen with shield displacement. The eddy current response was examined inside a Varian 7.0 T head only system, with a artificial copper bore inserted. It was found that the tolerance of the shield position for both coils and any direction of misalignment was quite high.

In chapter 3 the minimum energy method was introduced as a way of designing shielding coils on arbitrary surfaces for known primary current densities. This method is extremely robust, and represents an improvement over previous methods because it is capable of calculating solutions over any geometry, not just simple ones, and it is a direct calculation, not an optimization algorithm. Shields were designed using the minimum energy method and compared to a previous widely used shielding method (1) for validation. Mathematical verification was also provided. The unconventional case of a cylindrical gradient shielded with a rectangular shield was designed to demonstrate the versatility of the method. This method extends far beyond the likes of MR gradient and shim design. In fact, it should be viewed as an engineering tool, as it is capable of calculating shields for any known current density provided the quasi-static assumptions are not violated.

In chapter 4 the design and construction of a high power shim set for the purpose of dynamic shimming is outlined. The shim set contained ten shim axes:  $z^0$ ,  $x$ ,  $y$ ,  $z$ ,  $xz$ ,  $yz$ ,  $z^2$ ,  $xy$ ,  $x^2-y^2$ , and  $z^3$ , with all the zonal shims being actively shielded. The shim set was designed to operate with conventional gradient amplifiers driving each shim axis. A multitude of new design and construction techniques were exploited to overcome the

challenges associated with limited bore space, and inductive coupling. The zonal shims doubled as cooling layers using hollow wire, and the z-shim was split into two layers to distribute the cooling more evenly throughout the shim insert. Each axis was built directly onto the previous one with the only supporting structures being the epoxy they were encased in. The measured field profiles agreed well with simulation and the cooling capability was as predicted.

Finally, chapter 5 presented a direct application of the minimum energy method outside the context of imaging coils. The minimum energy method was used to shield entire MR systems or conversely shield the outside world from the MR systems. The case study of placing conducting wires inside the walls of an MR room for the purpose of stray field reduction was examined and ultimately it was deemed that the power requirements for such a shield would be too high, making it unfeasible. However, several other MR environment shielding situations proved more successful. The case of shielding an adjacent room by constructing an active shield that contoured the walls floor and ceiling of the room was examined, and was deemed feasible. The case of a shielded equipment cabinet in close proximity to the MR system also showed great promise. Finally two dynamic shielding cases were examined; the first being a shielded equipment cabinet that responded to the field of a moving MR system and the second being a shielded equipment cart that could move freely in the vicinity of the MR system and have its shield current adapt to the changing flux. Practical limits place restrictions on how close such a cart could get to the MR system and still remain reasonably shielded inside. The shields presented in this work represent the first time distributed winding electromagnets have been examined in the context of secondary active shielding.

## 6.2 Future work

### 6.2.1 Eddy current measurements

The eddy current measurements performed addressed the necessary questions regarding the tolerance of shielded insert coils. However, the problem of a varying impedance mismatch, among other uncertain factors, limited the predictive power of the model. Ultimately, a more careful experiment may have overcome these problems. It would be

of interest to repeat this experiment, while limiting the impedance mismatch, to possibly further isolate the eddy behavior. Another avenue of interest is the dependence on system geometry, which is crucial in accurately determining the eddy current response. Performing this experiment in more than one MR system with different bore sizes would give insight into the dependence on the relative size of the coil and system.

### 6.2.2 Minimum energy method

If the discovery of this method occurred earlier this thesis would look very different. The minimum energy method has proven extremely useful in countless different applications since its creation. The capabilities of this technique are only apparent to the few who work closely with it at the moment, but the list of applications that can likely benefit from this is long and still growing.

The most obvious extension to this method is that of eddy current modeling. The shielding current density is nothing more than the eddy current density that would be produced on that surface. Without knowledge of the primary current densities current input, this method can only model the spatial distribution of the eddy current, and gives no amplitude information. However, extending this method to account from an input waveform makes this a powerful eddy current modeling tool, not just in the realm of MR, but for any systems that operate in the quasi-static regime.

If the minimum energy method can be extended to model the eddy currents on an arbitrary conducting surface given a known primary current density and a known current input. Then one could go a step further and use it to calculate the heat induced in the conductor as a result of driving the primary coil. This is an extremely useful application of this method in terms of medical device testing in MR, and one could imagine that other areas could benefit from such a model.

Another important direction for the minimum energy method is that of simultaneous primary and shield design. The minimum energy constraint can be implemented with the original BE method to design both the primary and the shield in

tandem. In hind sight it is surprising that this idea was not immediately conceived, nevertheless it will surely become a reality in the very near future.

Among one of the most intriguing avenues for exploration is the idea of proximity of the shield relative to the primary versus the benefits of symmetry. There are many instances in which a shield could be brought closer to the region that is to be shielded (and thus further away from the primary coil) by changing the shape to more closely conform to that region. The result would be a more efficient shielded coil; although the effect on uniformity remains to be seen for various geometries. This could result in a new way to improve efficiency for customized shield gradient designs.

Countless other shielding applications exist to which this method could be applied; MR stray field reduction via room shielding presented in chapter 5 was only one of many. The minimum energy method shows promise in small device shielding, as well as shielding more exotic insert coils such as DREAMR (2).

### 6.2.3 Dynamic shim set

The next phase for the work related to the high power dynamic shim set introduced in chapter 4 is implementation and imaging. The shim insert is set to be integrated with a Varian 7.0 T head only system and preliminary imaging studies will be conducted to test its dynamic shimming capabilities in a retrospective fashion at first. The ultimate goal this system is true real time dynamic shimming for small animal applications.

The implementation of an insert coil such as this is not trivial. Standard clinical MR consoles are capable of gradient waveform control throughout the imaging sequence. However, extra channels for shim current updating during the imaging sequence are usually not available. Overcoming this problem is the major obstacle in the implementation of this insert coil. The proposed method is to use excess RF channels to trigger pre-programmed current waveforms. This requires customized hardware to interface between the console and the gradient amplifiers that are responsible for driving each shim coil. Another area that remains uncertain is the ability to map the  $B_0$  inhomogeneities fast enough. Initial imaging experiments will make use of

predetermined shim settings via RASTAMAP (3), but eventually the goal will be real time shimming, which will require very fast current calculations.

#### 6.2.4 Room shielding

The future direction of this work is fairly straight forward. It has already been shown that most of these shields are feasible from a power perspective. The next step is to develop the fabrication methods necessary to construct and test them. A first step would likely see scale models of full room designs as a proof of principle. The major challenge with these type of coils is that they are many times larger than anything our group has built previously and a piecewise construction process would be necessary to make them a reality.

## 6.3 References

1. Chronik BA, Alford JK, Rutt BK, Scholl TJ, Handler WB. 2009 Delta Relaxation Enhanced MR: Improving Activation-Specificity of Molecular Probes through R(1) Dispersion Imaging. *Magnetic Resonance in Medicine*;61(4):796-802.
2. Turner R, Bowley RM. 1986 Passive Screening of Switched Magnetic-Field Gradients. *Journal of Physics E-Scientific Instruments*;19(10):876-879.
3. Menon RS, Klassen LM. 2004 Robust automated shimming technique using arbitrary mapping acquisition parameters (RASTAMAP). *Magnetic Resonance in Medicine*;51(5):881-887.

## Appendix A

### A Minimum energy method and analytical method equivalency

This appendix shows the equivalency of the minimum energy method and the analytic solutions to the shielding of infinite cylinders provided in Turner and Bowley (1). The analytic solutions for the shielding current density components are given by the following expressions (1):

$$j_z^m(k) = -J_z^m(k) \frac{R_p^2 I_m'(kR_p)}{R_s^2 I_m'(kR_s)} \quad (\text{A.1})$$

$$j_\phi^m(k) = -J_\phi^m(k) \frac{R_p I_m'(kR_p)}{R_s I_m'(kR_s)}. \quad (\text{A.2})$$

$j_z^m$  and  $j_\phi^m$  are the Fourier transforms of the  $z$ - and  $\phi$ -components of the shielding current densities respectively.  $J_z^m$  and  $J_\phi^m$  are the Fourier transforms of the primary current densities.  $R_p$  is the primary radius, and  $R_s$  is the shield radius. Lastly  $I_m$  is a modified Bessel function of the first kind. The energy stored in the entire system is given by:

$$W = \frac{1}{2} L_{total} I^2, \quad (\text{A.3})$$

where:  $L_{total} = L_{primary} + L_{shield} + 2M$ . Taking the derivative of the energy with respect to the Fourier transform of the  $\phi$ -component of shield current density and equating it to zero gives the following result:

$$\frac{\partial L_{shield}}{\partial j_\phi^m(k)} = -2 \frac{\partial M}{\partial j_\phi^m(k)}. \quad (\text{A.4})$$

Now substituting expressions for the self (2) and mutual inductance (3) into the above formula to give the following for the left hand side:

$$\frac{\partial \mathcal{L}_s}{\partial j_\phi^m(k)} = -\mu_0 R_s^2 \sum_m \int_{-\infty}^{+\infty} \frac{\partial}{\partial j_\phi^m(k)} |j_\phi^m(k)|^2 I_m'(kR_s) K_m'(kR_s) dk, \quad (\text{A.5})$$

where:  $|j_\phi^m(k)|^2 = j_\phi^{-m}(-k)j_\phi^m(k)$ . So taking the derivative with respect to  $j_\phi^m(k)$  results in:

$$\frac{\partial \mathcal{L}_s}{\partial j_\phi^m(k)} = -2\mu_0 R_s^2 \sum_m \int_{-\infty}^{+\infty} j_\phi^{-m}(-k) I_m'(kR_s) K_m'(kR_s) dk. \quad (\text{A.6})$$

Now substituting (A.2) for the shielding current density and exploiting the following Bessel function identities (4):

$$I'_{-m}(k) = I'_m(k) \quad (\text{A.7})$$

$$I'_{-m}(-k) = (-1)^m I'_m(k) \quad (\text{A.8})$$

gives:

$$\frac{\partial \mathcal{L}_s}{\partial j_\phi^m(k)} = -2\mu_0 R_s^2 \sum_m \int_{-\infty}^{+\infty} \left( -J_\phi^{-m}(-k) \frac{R_p I'_m(kR_p)}{R_s I'_m(kR_s)} \right) I'_m(kR_s) K'_m(kR_s) dk \quad (\text{A.9})$$

$$\frac{\partial \mathcal{L}_s}{\partial j_\phi^m(k)} = 2\mu_0 R_p R_s \sum_m \int_{-\infty}^{+\infty} J_\phi^{-m}(-k) I'_m(kR_p) K'_m(kR_s) dk. \quad (\text{A.10})$$

Now addressing the right hand side of (A.4), which contains the mutual inductance between the shield and the primary coil gives:

$$-2 \frac{\partial \mathcal{M}}{\partial j_\phi^m(k)} = 2\mu_0 R_p R_s \sum_m \int_{-\infty}^{+\infty} \frac{\partial}{\partial j_\phi^m(k)} j_\phi^m(k) J_\phi^{-m}(-k) I'_m(kR_p) K'_m(kR_s) dk \quad (\text{A.11})$$

$$-2 \frac{\partial \mathcal{M}}{\partial j_\phi^m(k)} = 2\mu_0 R_p R_s \sum_m \int_{-\infty}^{+\infty} J_\phi^{-m}(-k) I'_m(kR_p) K'_m(kR_s) dk. \quad (\text{A.12})$$

Equations (A.12) and (A.10) are equivalent, so the expression for the  $\phi$ -component of shield current density components given by Turner and Bowley (1) is in fact the solution that minimizes the magnetic energy of the two-coil system. The same can be done for the  $z$ -component of the shielding current density to show that it too minimizes the magnetic



energy. Taking the derivative of the energy with respect to the Fourier transform of the  $z$ -component of shield current density and equating it to zero gives the following result:

$$\frac{\partial L_{shield}}{\partial j_z^m(k)} = -2 \frac{\partial M}{\partial j_z^m(k)}. \quad (\text{A.13})$$

Now substituting expressions for the self (2) and mutual inductance (3) into the above formula to give the following for the left hand side:

$$\frac{\partial L_s}{\partial j_z^m(k)} = -\mu_0 R_s^2 \sum_m \int_{-\infty}^{+\infty} \frac{\partial}{\partial j_z^m(k)} |j_\phi^m(k)|^2 I_m'(kR_s) K_m'(kR_s) dk \quad (\text{A.14})$$

$$\frac{\partial L_s}{\partial j_z^m(k)} = -\mu_0 R_s^2 \sum_m \int_{-\infty}^{+\infty} \frac{\partial}{\partial j_z^m(k)} \left| \frac{kR_s}{m} j_z^m(k) \right|^2 I_m'(kR_s) K_m'(kR_s) dk, \quad (\text{A.15})$$

where:  $|j_z^m(k)|^2 = j_z^{-m}(-k) j_z^m(k)$ . So taking the derivative with respect to  $j_z^m(k)$  results in:

$$\frac{\partial L_s}{\partial j_z^m(k)} = -2\mu_0 R_s^4 \sum_m \int_{-\infty}^{+\infty} \frac{k^2}{m^2} j_z^{-m}(-k) I_m'(kR_s) K_m'(kR_s) dk. \quad (\text{A.16})$$

Now substituting (A.2) for the shielding current density and exploiting the following Bessel function identities (4):

$$I_{-m}'(k) = I_m'(k) \quad (\text{A.17})$$

$$I_{-m}'(-k) = (-1)^m I_m'(k). \quad (\text{A.18})$$

results in:

$$\frac{\partial L_s}{\partial j_z^m(k)} = -2\mu_0 R_s^4 \sum_m \int_{-\infty}^{+\infty} \frac{k^2}{m^2} \left( -J_z^{-m}(-k) \frac{R_p^2 I_m'(kR_p)}{R_s^2 I_m'(kR_s)} \right) I_m'(kR_s) K_m'(kR_s) dk \quad (\text{A.19})$$

$$\frac{\partial L_s}{\partial j_z^m(k)} = 2\mu_0 R_p^2 R_s^2 \sum_m \int_{-\infty}^{+\infty} \frac{k^2}{m^2} J_z^{-m}(-k) I_m'(kR_p) K_m'(kR_s) dk. \quad (\text{A.20})$$

Addressing the right hand side of (A.13) which contains the mutual inductance between the shield and the primary coil gives:

$$-2 \frac{\partial M}{\partial j_z^m(k)} = 2\mu_0 R_p R_s \sum_m \int_{-\infty}^{+\infty} \frac{\partial}{\partial j_z^m(k)} J_\phi^m(k) J_\phi^{-m}(-k) I_m'(kR_p) K_m'(kR_s) dk \quad (\text{A.21})$$

$$-2 \frac{\partial M}{\partial j_z^m(k)} = 2\mu_0 R_p R_s \sum_m \int_{-\infty}^{+\infty} \frac{\partial}{\partial j_z^m(k)} \left( -\frac{kR_s}{m} j_z^m(k) \right) \left( -\frac{kR_p}{m} J_z^{-m}(-k) \right) I_m'(kR_p) K_m'(kR_s) dk \quad (\text{A.22})$$

$$-2 \frac{\partial M}{\partial j_\phi^m(k)} = 2\mu_0 R_p^2 R_s^2 \sum_m \int_{-\infty}^{+\infty} \frac{k^2}{m^2} J_z^{-m}(-k) I_m'(kR_p) K_m'(kR_s) dk \quad (\text{A.23})$$

Thus, the full analytic solution for the optimal shielding current density obtained through minimizing the stored magnetic energy is the same as the solution that was originally derived by Turner and Bowley (1) via a target field approach.

## A.1 References

1. Turner R, Bowley RM. 1986 Passive Screening of Switched Magnetic-Field Gradients. *Journal of Physics E-Scientific Instruments*;19(10):876-879.
2. Turner R. 1988 Minimum Inductance Coils. *Journal of Physics E-Scientific Instruments*;21(10):948-952.
3. Carlson JW, Derby KA, Hawryszko KC, Weideman M. 1992 Design and Evaluation of Shielded Gradient Coils. *Magnetic Resonance in Medicine*;26(2):191-206.
4. Abramowitz M, Stegun I.A. *Handbook of Mathematical Functions with Formulas, Graphs, and Mathematical Tables*. Washington D.C.: Dover Publications; 1972.

## Curriculum Vitae

### **Dustin W. Haw**

Department of Physics and Astronomy  
The University of Western Ontario  
London Ontario, Canada  
N6A 3K7

---

### **Education**

Ph. D. Candidate 2006-2011	University of Western Ontario Department of Physics and Astronomy London, Ontario, Canada
Bachelor of Science (Honours Physics) 2002-2006	University of Western Ontario Department of Physics and Astronomy London, Ontario, Canada

### **Awards**

Award of Excellence in Teaching	2009
Ontario Graduate Scholarship for Science and Technology	2008-2010
Western Graduate Research Scholarship	2006-2011
Gold Medal in Medical Physics	2006/04
University of Western Ontario Entrance Scholarship	2002/09
Raymond Industrial Equipment Scholarship	2002/09
Governor General's Academic Medal	2002/06

### **Related work experience**

Sept. 2006 – 2011	Graduate Research Assistant, Physics and Astronomy University of Western Ontario Supervisor: Blaine Chronik
Sept. 2006 – 2011	Teaching Assistant, Physics and Astronomy University of Western Ontario Supervisors: Khanti. Kaluarachchi, Jeff Hutter, Margaret Campbell-Brown, Eugene Wong, Shantanu Basu, Wayne Hocking, Aaron Sigut
May 2006 – Aug. 2006	Summer Research Student, Physics and Astronomy

University of Western Ontario  
Supervisor: Blaine Chronik

- Sept. 2005 – Apr. 2006      Research Assistant, Physics and Astronomy  
University of Western Ontario  
Supervisor: Blaine Chronik
- May 2005 – Aug. 2005      Summer Research Student, Physics and Astronomy  
University of Western Ontario  
Supervisor: Blaine Chronik

## **Publications**

### **Journal articles**

Haw DW, Harris CT, Handler WB, Chronik BA. 2011 A minimum energy method for the design of shielding coils over arbitrary geometries. *Phys Med Biol.* (*Submitted*)

### **Conference proceedings**

Haw DW, Chronik BA. Towards simultaneous PET and field-cycled MRI: active shielding for PMT detectors. *Proc. Intl. Soc. Reson. Med. 16* (Toronto, Canada) 2008

Haw DW, Chronik BA. Effect of active shielding on zonal shim coils for a 31cm bore 9.4T MR system. *Proc. Intl. Soc. Reson. Med. 16* (Toronto, Canada) 2008

Haw DW, Chronik BA. Towards dynamic shimming in a 31-cm-bore 9.4-T system: analysis of shim-shim inductive interactions. *Proc. Intl. Soc. Reson. Med. 17* (Honolulu, USA) 2009

Haw DW, Chronik BA. Shielding requirements for a complete 3<sup>rd</sup>-order shim set for a 31-cm-bore 9.4T system. *Proc. Intl. Soc. Reson. Med. 17* (Honolulu, USA) 2009

Haw DW, Dalrymple B, Van Sas F, Scholl TJ, Chronik BA. Mechanically adjustable shielded insert gradient for experimental evaluation of construction tolerances. *Proc. Intl. Soc. Reson. Med. 18* (Stockholm, Sweden) 2010

Haw DW, Harris CT, Handler WB, Chronik BA. Simple minimum energy method for calculating shielding coils on arbitrary geometries. *Proc. Intl. Soc. Reson. Med. 19* (Montreal, Canada) 2011